

UNIVERSITÉ DU QUÉBEC À MONTRÉAL

VALIDATION RADIOMÉTRIQUE DU «FAR INFRARED RADIOMETER»
ET ÉVALUATION DE SA SENSIBILITÉ À L'ÉTAT DE L'ATMOSPHÈRE
ARCTIQUE

MÉMOIRE
PRÉSENTÉ
COMME EXIGENCE PARTIELLE
DE LA MAÎTRISE EN SCIENCE DE L'ATMOSPHÈRE

PAR
LUDOVICK S.PELLETIER

NOVEMBRE 2019

UNIVERSITÉ DU QUÉBEC À MONTRÉAL
Service des bibliothèques

Avertissement

La diffusion de ce mémoire se fait dans le respect des droits de son auteur, qui a signé le formulaire *Autorisation de reproduire et de diffuser un travail de recherche de cycles supérieurs* (SDU-522 – Rév.01-2006). Cette autorisation stipule que «conformément à l'article 11 du Règlement no 8 des études de cycles supérieurs, [l'auteur] concède à l'Université du Québec à Montréal une licence non exclusive d'utilisation et de publication de la totalité ou d'une partie importante de [son] travail de recherche pour des fins pédagogiques et non commerciales. Plus précisément, [l'auteur] autorise l'Université du Québec à Montréal à reproduire, diffuser, prêter, distribuer ou vendre des copies de [son] travail de recherche à des fins non commerciales sur quelque support que ce soit, y compris l'Internet. Cette licence et cette autorisation n'entraînent pas une renonciation de [la] part [de l'auteur] à [ses] droits moraux ni à [ses] droits de propriété intellectuelle. Sauf entente contraire, [l'auteur] conserve la liberté de diffuser et de commercialiser ou non ce travail dont [il] possède un exemplaire.»

REMERCIEMENT

Je tiens à remercier avant tout mon superviseur Jean-Pierre Blanchet. Merci de m'avoir offert l'opportunité d'effectuer mon premier travail de recherche dans un milieu aussi singulier que la nuit polaire. Merci de m'avoir confié cette mission comme première expérience. Merci de m'avoir laissé une liberté don peu peuvent jouir au courant de leur parcours académique. Merci à Eva Monteiro et Pierre Gauthier pour les nombreuses réponses à mes questionnements parfois flous. Merci à mes collègues de CANDAC pour les discussions prolifiques concernant l'arctique et la télédétection. Merci à mes collègues et amis de l'UQÀM, qui m'ont accompagné pendant cette période. Merci à ma compagne de m'avoir soutenu et enduré au courant de cette aventure. Merci à Emily McCullough de m'avoir accueillie au laboratoire d'ØPAL, un conteneur entouré de loups et rempli de laser. Et surtout, merci à Quentin Libois, pour m'avoir initié à la recherche et pour avoir, par l'exemple, fixé un standard que je viserai toujours avec admiration.

TABLE DES MATIÈRES

LISTE DES TABLEAUX	v
TABLE DES FIGURES	vii
ACRONYMES	ix
RÉSUMÉ	xiii
INTRODUCTION	1
CHAPITRE I WINTER FAR INFRARED MEASUREMENTS IN THE HIGH ARCTIC	9
1.1 Introduction	13
1.2 The Far InfraRed Radiometer	19
1.2.1 Technical Characteristics	20
1.2.2 Filters	22
1.2.3 Instrumental Setup	25
1.2.4 Signal Processing	26
1.2.5 Calibration	29
1.3 The Eureka Campaign	32
1.3.1 Climatology	32
1.3.2 ØPAL	34
1.3.3 Weather	41
1.4 Radiometric Validation	44
1.4.1 Radiative Transfert Simulation	44
1.4.2 Radiative Closure Experiment	46
1.4.3 Radiometric Resolution	50
1.5 Water Vapour	55
1.5.1 PWV Observation	55

1.5.2 PWV Retrieval	58
1.6 Ice Cloud and Arctic Haze	62
1.6.1 TIC Observations	64
1.6.2 TIC Classification Algorithm	75
1.7 Conclusion	79
CONCLUSION	83
BIBLIOGRAPHIE	87

LISTE DES TABLEAUX

Tableau	Page
1.1 Radiative Closure Results	49
1.2 Comparison between the FIRR and E-AERI/MODTRAN	53
1.3 coefficient use in Eq : (1.21)	59
1.4 Results of inter-comparison of PWV measurements between the FIRR and the radiosonde	61
1.5 FIRR measured downwelling radiances for a case of TIC-1	66
1.6 FIRR measured downwelling radiances for the case of TIC-2B	68
1.7 FIRR measured downwelling radiances for the case of TIC-2A	70
1.8 FIRR measures downwelling radiances for the case of arctic haze	74



TABLE DES FIGURES

Figure	Page
1.1 Schematic of the FIRR Optomechanical Device	20
1.2 FIRR filters and atmospheric gas absorption	22
1.3 FIRR Filters and Examples of Downwelling Radiances	24
1.4 FIRR installation at OPAL	25
1.5 Comparison with the CRL and a radiosonde corrected atmospheric profile	38
1.6 Time series of the weather vertical profiles and surface conditions obtain from radiosonde datasets at Eureka, Nu between February 22 and March 3, 2016	43
1.7 Clear sky simulated and observed downwelling radiance	48
1.8 Residual between the FIRR and the E-AERI and between the FIRR and MODTRAN	51
1.9 Comparison between CRL and radiosonde corrected atmospheric profile	56
1.10 Variation of both ΔBT in respect to the water vapour total column PWV[mm] for clear sky events	58
1.11 PWV from integrated radiosonde RH profile vs. the PWV retrieve using the FIRR	60
1.12 24h Time series of cloud observations above ØPAL on February 24, 2016	63
1.13 Observed case of TIC-1 above ØPAL on February 24, 2016	65
1.14 Cloud Radiative Forcing From a Case of TIC-1.	66
1.15 Observed case of TIC-2b above ØPAL on March 27, 2016	68

1.16 Cloud Radiative Forcing From a Case of TIC-2B	69
1.17 Observed case of TIC-2A above ØPAL on March 6, 2016	70
1.18 Cloud radiative forcing from a case of TIC-2A	71
1.19 Observed case of arctic haze above ØPAL on March 22, 2016	73
1.20 Cloud Radiative Forcing From a Case of Arctic Haze	74
1.21 FIRR TIC classification	78

LISTE DES ACRONYMES

FRANÇAIS

ASC	Agence Spatiale Canadienne
D_{eff}	Diamètre Effectif
HR	Humidité Relative
HR_i	Humidité Relative par rapport à la glace
IR	InfraRouge
IRL	InfraRouge Lointain
IRT	InfraRouge Thermique
NG	Noyaux Glacigène
Ni	Nombre de cristaux de glace
TIC	Nuage de glace optiquement mince

ANGLAIS

ABB	Ambient Black Body
AW	Atmospheric Window
BB	BlackBodies
CANDAC	Canadian Network for the Detection of Atmospheric Changes
CRF	Cloud Radiative Forcing
CRL	Candac Raman Lidar
CSA	Canadian Space Agency
CS	Clear Sky
D_{eff}	Effective diameter
DGF	Dehydration Greenhouse Feedback
DW	Dirty Window
ECCC	Environment and Climate Change Canada
EWS	Eureka Weather Station
FIR	Far InfraRed
FIRR	Far InfraRed Radiometer
FIRST	Far-Infrared Spectroscopy of the Troposphere
FORUM	Far Infrared Outgoing Radiation Understanding and Monitoring
GRUAN	GCOS (Global Climate Observing System) Reference Upper-Air Network
HBB	Hot Black Body
IC	Ice Crystal
IR	Infrared
IWC	Ice Water Content

MMCR	MilliMeter Cloud Radar
MODTRAN	MODerate resolution atmospheric TRANsmission
MODIS	Moderate Resolution Imaging Spectroradiometer
MS	Measurment Sequence
Ni	Ice crystal numbers
NWP	Numerical weather prediction
OEM	Optimal Effective Method
OMD	Optomechanical device
REFIR	Radiation Explorer in Far-Infrared
RMSD	Root Mean Square Difference
RTM	radiative transfer model
SEM	Stadard Error to the Mean
SSM	Scene selecting Mirror
STD	Standard Deviation
SV	Skyview
TIR	Thermal-infrared
TACTS	Tropospheric Airborne Fourier Transfer Spectrometer
TIC	Thin Ice Clouds
TICFIRE	Thin Ice Clouds in Far InfraRed Experiment
TOA	Top of the Atmosphere

RÉSUMÉ

Durant la nuit polaire, la majorité de la radiation terrestre est émise dans l'infrarouge lointain(IRL) ($\lambda > 15\mu m$). Lorsque le contenu en eau précipitable est inférieur à 10 mm, l'atmosphère commence à devenir partiellement transparente dans cette région du spectre, ouvrant la fenêtre atmosphérique vers de plus grandes longueurs d'onde. De petites variations de vapeur d'eau peuvent donc fortement influencer la transmittance de l'atmosphère en réduisant l'effet de serre associé à celle-ci, ce qui engendre une augmentation de son refroidissement radiatif vers l'espace. Ceci est particulièrement vrai dans les régions polaires où 50% du refroidissement radiatif est effectué dans le IRL. De plus, les instruments de télédétection active à bord des satellites CALIPSO et CLOUDSAT ont permis de démontrer l'omniprésence de nuages de glace optiquement minces (TIC) dans ces régions. Ces nuages ont un effet important sur le bilan radiatif, car ils agissent comme un radiateur sur l'ensemble de l'atmosphère et le processus de formation de ces nuages est toujours mal compris. De récents travaux ont démontré l'utilité du IRL, dans un cadre de télédétection passive, afin de mesurer les propriétés optiques des nuages de glace ainsi que la vapeur d'eau dans les régions froides de l'atmosphère. Malgré tout, il n'existe présentement aucun instrument satellitaire utilisant cette portion du spectre pour observer la Terre. Le projet de satellite TICFIRE (Thin Ice Cloud in the Far Infrared Experiment) de l'agence spatiale canadienne vise à combler cette lacune. Dans cette étude, nous présentons les résultats de la première campagne de terrain d'un prototype de l'instrument destiné au projet TICFIRE, le «Far InfraRed Radiometer» (FIRR), qui a mesuré la radianc émise par l'atmosphère vers le sol à Eureka, NU N79°59'20"W85°56'27" du 25/02/2016 au 31/05/2016. Le FIRR utilise comme détecteur un microbolomètre qui mesure la radianc dans 9 bandes spectrales à des longueurs d'onde incluse entre 8 - 50 μm . Dans cette région spectrale, l'émissivité de l'atmosphère est très sensible au contenu en vapeur d'eau et au diamètre des cristaux de glace. En comparant les mesures du FIRR à celles d'un interféromètre ainsi qu'à des valeurs de radianc obtenues à l'aide d'un modèle de transfert radiatif, la résolution et la précision de cette nouvelle technologie ont été évaluées. Sa sensibilité aux propriétés microphysiques a aussi été testée à l'aide d'un Radar et d'un Lidar. Nos résultats démontrent que la précision et la résolution du FIRR ont une valeur similaire à celles obtenues en laboratoire avec un bruit inférieur à $0.02 [Wm^{-2}sr^{-1}]$. L'instrument permet de mesurer de faibles quantités de vapeur d'eau avec une précision

similaire et parfois supérieure à celle d'autres instruments utilisés en région polaire. Le FIRR démontre une bonne sensibilité aux propriétés microphysique des TICs et permet de classifier les nuages en fonction de leur diamètre effectif.

Mot-clés : Cirrus- Infrarouge lointain- Radiomètre- Nuit polaire- Vapeur d'eau-

INTRODUCTION

La Terre avec une température effective de 255 K, émet 40% de son rayonnement vers l'espace dans des longueurs d'onde appartenant à la région spectrale de l'infrarouge lointain (IRL) ($\lambda > 15\mu m$) (Harries *et al.*, 2008). Dans les régions froides et sèches de l'atmosphère, telle que la haute troposphère ou les régions polaires durant l'hiver, plus de 60% du refroidissement radiatif vers l'espace est émis dans cette portion du spectre (Clough *et al.*, 1992), où l'émissivité de l'atmosphère est largement dominée par les modes rotationnels de la vapeur d'eau (Turner et Mlawer, 2010) ainsi que les propriétés optiques des nuages.

Durant la nuit polaire, une large portion du refroidissement radiatif de la surface a lieu dans des longueurs d'onde proche de $20\mu m$, dans ce qu'on appelle la fenêtre atmosphérique «sale» (Tobin *et al.*, 1999). La transmittance de l'atmosphère dans ces longueurs d'onde dépend fortement de la quantité d'eau précipitable présente dans la colonne d'air, ceci engendre une forte corrélation entre les températures de surface et la quantité de vapeur d'eau (Lesins *et al.*, 2010). Ceci n'est pas seulement valable aux pôles, mais aussi dans la haute troposphère des basses latitudes, où la quantité d'eau précipitable, des niveaux élevés de l'atmosphère, est encore plus basse.

Comme dans l'infrarouge thermique (IRT) ($\lambda < 15\mu m$), la radiation terrestre dans le IRL est aussi affectée par la couverture nuageuse. L'émissivité des nuages optiquement épais dépend presque uniquement de leur température effective, celle des cirrus, par contre, dépend aussi de leurs propriétés microphysiques, telles que le nombre de cristaux (Ni), le diamètre effectif (D_{eff}) et la forme de ceux-ci (Yang,

2003).

Actuellement les nuages représentent la plus grande incertitude des modèles climatiques (IPCC, 2013). Les propriétés radiatives et microphysiques des cirrus sont toujours mal comprises et les modèles globaux ont tendance à surestimer la valeur de Ni (Krämer *et al.*, 2016). Des campagnes de mesures aéroportées destinées aux cirrus de la tropopause tropicale ont démontré une large variabilité concernant leur D_{eff} et Ni (Jensen *et al.*, 2008). Pour des valeurs d'humidité relative (HR), de température et de vitesse verticale similaire, deux types de cirrus semblent se définir. L'un avec des valeurs de Ni plus élevées et un D_{eff} petit, et l'autre avec un D_{eff} plus élevé, mais un Ni beaucoup plus faible. Le dernier cas est généralement associé à une sursaturation par rapport à la glace plus élevé à l'intérieur du nuage plus élevé, avec des valeurs d'humidité relative par rapport à la glace (HR_i) pouvant atteindre 160%. (Krämer *et al.*, 2009) expliquent cette corrélation par le fait qu'une faible quantité de cristaux de glace ne permet pas d'absorber par déposition la totalité de la vapeur d'eau en excès dans leur environnement. La valeur de HR_i reste donc élevée même à l'intérieur du nuage. Un faible Ni favorise aussi une valeur supérieure pour le D_{eff} , car plus de vapeur d'eau est disponible pour chaque cristal.

Des propriétés microphysiques similaires ont aussi été observées en Arctique durant une campagne aéroportée en Alaska (Jouan *et al.*, 2012). Grâce à la détection active satellitaire, l'omniprésence, pendant la nuit polaire, de ces deux types de nuages de glace optiquement mince (TIC) avait préalablement été démontré par (Grenier *et al.*, 2009). Ces nuages présents sur l'ensemble du profil de la troposphère agissent comme un radiateur qui contribue à refroidir l'atmosphère (Blanchet *et al.*, 2011).

En plus d'affecter directement le bilan radiatif atmosphérique, les TIC peuvent

affecter celui-ci de manière indirecte. Pour les nuages ayant un D_{eff} assez large, les cristaux qui s'y forment peuvent atteindre une taille suffisante pour précipiter, déshydratant du même coup de manière permanente la couche atmosphérique où c'était formé le nuage. Il en résulte une augmentation du refroidissement radiatif vers l'espace. Ce processus a déjà été étudié à l'aide d'une modélisation régionale centrée sur l'Arctique (Blanchet et Girard, 1995). Il a été démontré qu'un tel refroidissement peut engendrer une boucle de rétroaction, en favorisant la formation ultérieure de TIC, qui à leur tour déshydratent l'atmosphère. Cet effet est appelé «Dehydration greenhouse feedback»(DGF) et a le potentiel d'accroître le refroidissement de l'atmosphère durant la nuit polaire.

De plus, les TICs présents à la tropopause tropicale servent de porte d'entrée vers la stratosphère pour la vapeur d'eau provenant des plus bas niveaux. Les propriétés micropysiques des cirrus fins influencent leur habilité à déhydrater l'air avant son entrée dans la stratosphère et influencent donc le flux de vapeur d'eau traversant la tropopause(Jensen *et al.*, 2013). La vapeur d'eau stratosphérique est un puissant gaz à effet de serre. De faibles fluctuations dans sa concentration peut ralentir ou accélérer de 25% le réchauffement climatique (Solomon *et al.*, 2010).

Les TICs sont des cirrus qui se forment directement en phase solide et sont aussi connus sous le nom de «*in situ* cirrus» (Krämer *et al.*, 2016). Deux procédés sont responsables de leur formation. Le gel homogène est lorsque des aérosols liquides gèlent subitement lorsqu'une valeur critique de HR_i est atteinte. Cette valeur de HR_i dépend presque uniquement de la température et non de la composition chimique des aérosols (Koop *et al.*, 2000). Le gel hétérogène se produit lorsqu'un aérosol liquide va geler suite au contact avec un noyau glacigène (NG), ou lorsque la WV se dépose directement sur un NG. Dans un même nuage, les deux régimes sont souvent en compétition(Sullivan *et al.*, 2016) . Lorsque le nombre de NG est élevé, le régime hétérogène sera favorisé et la valeur de Ni sera élevée, car

directement proportionnelle au nombre de NG. Lorsque très peu de NG sont présents dans l'air, le régime homogène sera dominant et un Ni élevé sera aussi favorisé. C'est lorsque le nombre de NG favorise la plus forte compétition entre les deux régimes que le Ni atteint les valeurs observées les plus faibles et permet l'accroissement du D_{eff} .

La nature, l'origine et les propriétés de nucléation de ces NG sont encore mal comprises. La poussière de kaolinite considérée comme un excellent NG, peut être affectée par la présence d'un revêtement d'acide sulfurique qui décroît sa capacité de nucléation à des températures inférieures à -40°C (Ansmann et Müller, 2005). (Sullivan *et al.*, 2010) a démontré que ce processus était irréversible même après neutralisation de l'acide par l'ammonium. Contre intuitivement, des particules solides de sulfate d'ammonium peuvent agir comme des NG, ceci favorisant la compétition entre les deux régimes et engendre des TICs ayant un Ni plus faible et un D_{eff} plus élevé que ceux formés uniquement par le régime homogène (Abbatt *et al.*, 2006) .

Afin de bien représenter le bilan radiatif terrestre dans les modèles climatiques, le spectre des émissions atmosphériques dans le IRL doit être adéquatement résolu par les modèles de transfert radiatif (Mlynczak *et al.*, 2005). Pour ce faire, le cycle de l'eau dans les régions froides et sèches de l'atmosphère doit être mieux compris (Harries *et al.*, 2008). Il est donc d'une grande importance de mieux comprendre les processus de formation des TICs et leur influence sur la distribution verticale de la vapeur d'eau.

La dernière génération de satellites dédiés à l'étude des nuages tels que Calipso (Winker *et al.*, 2003) et CLOUDSAT (Stephens *et al.*, 2002), a permis de fortement améliorer la couverture globale des observations des TICs (Delanoë et Hogan, 2008). Ils ont aussi permis leur étude dans les environnements polaires

(Grenier *et al.*, 2009). Par contre, leur couverture reste limitée et restreinte à une mince coupe verticale de l'atmosphère. L'utilisation de technologie de télé-détection passive permet quant à elle de faire de l'imagerie 2D et permet une étude de la structure horizontale des nuages. À l'aide de la méthode «split window» (Inoue, 1985), il est possible de mesurer l'épaisseur optique (τ) et le D_{eff} des cirrus, en effectuant une différence de température de brillance (BT) entre deux canaux situés dans la fenêtre atmosphérique aux longueurs d'onde $11\mu m$ et $12\mu m$. Le spectroradiomètre à bord de la dernière génération de satellites météorologiques opérationnels (GOES-R) utilise toujours une technique similaire afin de retrouver les propriétés optiques des cirrus. Des techniques plus avancées basées sur la méthode d'optimisation effective (OEM) (Rodgers, 2000), utilise tous les canaux disponibles afin de trouver l'état le plus probable du nuage. Cette méthode a été appliquée par (Wang *et al.*, 2016), aux mesures du Moderate Resolution Imaging Spectroradiometer (MODIS) (King *et al.*, 1992). Malgré le fait que ces instruments soient à la fine pointe de la technologie, ceux-ci sont toujours sujets à certaines limitations . En effet, les méthodes qui utilisent l'IR pour retrouver les propriétés des nuages de glace sont peu adaptées pour des cristaux plus gros ($D_{eff} \geq 80\mu m$) (Merrelli et Turner, 2013), et la faible émissivité de la surface durant la nuit polaire décroît fortement la qualité du signal et rend les mesures moins précises (Liu *et al.*, 2010).

(Baran, 2009), (Yang, 2003) et (Palchetti *et al.*, 2016a) ont démontré le potentiel des mesures hyperspectrales dans le IRL pour mesurer les propriétés des TICs. Utilisant une OEM, (Libois et Blanchet, 2017) ont démontré que l'ajout de seulement quelques bandes larges dans le IRL aux bandes du radiomètre satellitaire actuel permet de réduire l'incertitude concernant τ et D_{eff} par 50%. Cette portion du spectre inclut aussi les bandes purement rotationnelles de la vapeur d'eau qui coïncident avec un maximum de son continuum (Shine *et al.*, 2012). L'utili-

sation de IRL pour détecter des traces de vapeur d'eau dans les régions froides de l'atmosphère est donc très prometteur (Shahabadi et Huang, 2014).

Malgré la démonstration du potentiel du IRL en termes de télédétection et son importance dans le bilan radiatif global (Mlynczak *et al.*, 2005), il n'y a présentement aucun instrument observant la Terre depuis l'espace qui couvre cette portion du spectre. Ceci était essentiellement dû aux limitations technologiques. Le récent développement de meilleures technologies a renouvelé l'intérêt scientifique pour le IRL. Présentement le projet satellitaire de l'agence spatiale européenne FORUM (Palchetti *et al.*, 2016b), vise spécialement l'étude des nuages de glace. Celle-ci est basée sur la technologie du Radiation Explorer in the Far-InfraRed – Prototype for Applications and Development (REFIR-PAD) (Palchetti *et al.*, 2006). Cet interféromètre a déjà été utilisé afin d'étudier les TICs dans un environnement polaire (Palchetti *et al.*, 2015). D'autres interféromètres mesurant le F-IR ont été récemment développés. Le E-AERI (Knuteson et Revercomb, 2004), qui couvre les longueurs d'onde inférieures à $25 \mu m$, a permis l'étude des nuages en Arctique (Cox *et al.*, 2014) (Mariani *et al.*, 2013) Le Tropospheric Airborne Fourier Transform Spectrometer (TAFTS) (Canas *et al.*, 1997), a été utilisé afin de mesurer le continuum de vapeur d'eau (Fox *et al.*, 2015) ainsi que pour caractériser l'émissivité de la neige dans le IRL (Bellisario *et al.*, 2017). Le Far-InfraRed Spectroscopy of the Troposphere (FIRST) (Mlynczak *et al.*, 2006), quant à lui, vise à mieux contraindre le bilan radiatif de l'atmosphère (Latvakoski *et al.*, 2013).

Malgré le fait que des mesures hyperspectrales du IRL sont souhaitables dans une optique de bilan radiatif, elles ne sont peut-être pas essentielles pour étudier les TICs et la vapeur d'eau depuis l'espace. La majorité de l'information relative aux TICs, contenue dans cette région spectrale, peut être obtenue en utilisant seulement quelques bandes larges (Libois et Blanchet, 2017).

Le projet satellitaire « Thin Ice Clouds in Far InfraRed Experiment »(TICFIRE) (Blanchet *et al.*, 2011), supporté par l'Agence Spatiale Canadienne (ASC), porte sur l'observation des TIC et du cycle de l'eau durant la nuit polaire. Utilisant un nouveau détecteur non refroidi et 9 filtres dans le IRL et l'infrarouge thermique (IRT), l'instrument est suffisamment petit pour être embarqué à bord d'un micro-satellite, ce qui réduit considérablement les coûts du projet. Avec comme objectif d'être utilisé comme un imageur, TICFIRE avec une résolution et une trace au sol de 10 km et 600 km respectivement, ainsi qu'une vitesse d'acquisition rapide permettra de bien observer la variation spatiale des cirrus.

En support au projet, ASC a financé le développement d'un prototype, le Far InfraRed Radiometer (FIRR)(Libois *et al.*, 2016b). Avec comme objectif de tester la technologie au cœur de TICFIRE, le FIRR a d'abord été conçu comme un instrument aéroporté avec une visée nadir comme le TICFIRE. Le FIRR a été testé pour la première fois lors de la campagne du Network on Climate and Aerosols : Addressing Key Uncertainties in Remote Canadian Environments (NETCARE) en 2015 (Libois *et al.*, 2016a). Par la suite, le FIRR a été déployé, en octobre 2016 à Eureka au Nunavut et est devenu pleinement opérationnel à la fin février 2016.

L'objectif de la campagne de terrain à Eureka était de prouver l'utilité, dans les conditions typiques de l'Arctique durant la nuit polaire, d'un radiomètre avec une visée zénithale observant le F-IR. Premièrement, la technologie devait être testée sur une longue période et sa résolution radiométrique quantifiée. Deuxièmement, la sensibilité du FIRR aux propriétés des TICs, ainsi qu'au contenu en vapeur d'eau devait être évaluée.

L'ensemble de cette évaluation, effectuée dans un article rédigé en anglais, constitue le cœur de ce mémoire. Les conclusions tirées de cette étude sont reprises dans

le dernier chapitre, suivi de la bibliographie.

CHAPITRE I

WINTER FAR INFRARED MEASUREMENTS IN THE HIGH ARCTIC

by

Ludovick S.Pelletier, Quentin Libois and Jean-Pierre Blanchet

Department of Earth and Atmospheric Sciences Université du Québec à
Montréal (UQAM), Montréal (Québec), Canada

Ce chapitre rédigé en anglais et est présenté sous forme d'article scientifique, afin
d'être soumis à un journal tel que : *Atmospheric Measurement Techniques*

Abstract

During the polar night, the majority of Earth's emission to space occurs in the Far InfraRed (FIR) ($\lambda > 15\mu\text{m}$). Below 10[mm] of integrated water vapour, the atmosphere becomes partially transparent in this spectral range, extending the atmospheric window to longer wavelengths. Small variations of the water vapour (WV) content leads to strong variations of the atmospheric transmittance, thus impacting its cooling rate by reducing the WV greenhouse effect. This is especially the case in the cold Arctic since more than 50% of atmospheric cooling occurs in the FIR. Furthermore, remote sensing observations from CALIPSO and Cloud-Sat satellites over the Arctic have enlightened the ubiquity of optically thin ice clouds (TIC). Those clouds act as effective radiators through the volume of the troposphere. However, their formation process is still poorly understood. Theoretical works have shown the added value of FIR measurements for the retrieval of WV and TIC optical properties. Despite its importance, there is currently no spaceborne instrument performing spectral measurements in the FIR range. The TICFIRE (Thin Ice Cloud in the Far Infrared Experiment) satellite project aims to fill this gap. In this study, we show the results of the first ground experiments using a breadboard of the satellite main instrument, the Far InfraRed Radiometer (FIRR). During a dedicated campaign, it measured downwelling radiance at Eureka, NU N $79^{\circ}59'20''$ W $85^{\circ}56'27''$ from 25/02/2016 to 31/05/2016. The FIRR uses an array of uncooled microbolometers to measure radiances in 9 spectral channels spanning from 8 to 50 μm . The atmospheric emission in this spectral region is very sensitive to its WV content and the effective diameter of TIC ice crystals. By comparing our measurements with the E-AERI, a Fourier transform interferometer which serves as a reference, and a radiative transfer model in a closure experiment, we assess the radiative accuracy of this new technology and its sensitivity to the state of the atmosphere. Results show that the *in situ* ra-

diometric accuracy of the FIRR matches controlled laboratory performances with noise levels below $0.02 \text{ Wm}^{-2}\text{sr}^{-1}$. The instrument shows a good potential for precipitable water vapour retrieval and is able to discriminate variations in the TIC optical properties. This paves the way for the development of TIC micro-physical properties monitoring from ground-based measurements and strengthen the case for TICFIRE as a spaceborne version, able to extend observation at a global scale.

Key-Words : Cirrus- Far Infrared- Radiometer- Water vapour- Arctic-

1.1 Introduction

With an effective temperature of 255K, Earth emits 40% of its outgoing radiation in the far-infrared (FIR) region of the spectrum ($\lambda > 15\mu m$) (Harries *et al.*, 2008). In cold and dry regions of the atmosphere, such as the upper troposphere or the Poles during winter, more than 60% of the radiative cooling to space occur in this part of the spectrum (Clough *et al.*, 1992), dominated by water vapour (WV) rotational bands (Turner et Mlawer, 2010) and clouds.

Through the polar night, large portion of surface cooling to space occurs in the so-called dirty window of the atmosphere (Tobin *et al.*, 1999), in the vicinity of the $20\mu m$ wavelength. The transmittance of the atmosphere in this spectral range depends on the amount of vertical precipitable water vapour (PWV). There is a strong correlation between PWV and surface temperature (Lesins *et al.*, 2010). This is not only true at the pole, but also in the upper troposphere at lower latitudes, where temperature and PWV above the highest layers of the troposphere reach even lower values.

As for in the thermal infrared (TIR) range ($\lambda < 15\mu m$) the outgoing FIR radiation is affected by the cloud cover. While optically thick cloud emissivity depends mostly on their effective temperature, cirrus radiative properties are a function of ice crystal number concentration (N_i), effective diameter (D_{eff}) and particulate shape (Yang, 2003).

Currently, clouds account for the largest uncertainty in climate models (IPCC, 2013). Radiative and micro-physical properties of cirrus clouds are still poorly understood and global models tend to overestimate N_i (Krämer *et al.*, 2016). Airborne campaigns near the tropical tropopause have shown a great variability in the physical properties of cirrus (Jensen *et al.*, 2008). For similar absolute

humidity, temperature and updraft speed, two broad types of cirrus have been observed. One with high Ni and small D_{eff} and another one with low Ni and large D_{eff} at comparable ice water concentration. The former case is generally associated with higher supersaturation over ice, up to 60%. (Krämer *et al.*, 2009) explain this correlation between ice high supersaturation and low Ni concentration based on observation that, the ice crystals (IC) population is not able to fully quench down all the WV excess in the environment, thus the relative humidity over ice (RH_i) remain supersaturated longer in the second type of clouds. Low Ni also favours a more rapid growth of the IC, since more WV is available for each crystal, thus leading to a larger D_{eff} . Similar cirrus properties were also observed in the Arctic during an airborne campaign above the north slope of Alaska (Jouan *et al.*, 2012). Using space-based remote sensing instruments, (Grenier *et al.*, 2009) showed the ubiquity of the two types of thin ice cloud (TIC) above both poles during winter. Those polar TIC exhibit similar micro-physical properties as in the tropics, with respect to Ni and D_{eff} variation.

Due in part to the large amplitude of their spectral emissivity, the micro-physical properties of TIC strongly influences the outgoing longwave radiation. Moreover, TIC also affects radiation indirectly, when larger crystal reach precipitating size, leading to dehydration of the upper layers and increasing the atmosphere radiative cooling to space of layers below due to reduce green house effect. This process was first investigated through regional climate modelling of the Arctic environment by (Blanchet et Girard, 1995) and was shown to induce a radiative feedback that favours more cloud formation and further dehydration of the atmosphere. It is referred as the Dehydration Greenhouse Feedback(DGF). It has the potential to increase cooling rates in the troposphere and at the ground, especially during polar winter. Moreover, cirrus in the upper troposphere lower stratosphere (UTLS) can act as a gateway, enabling WV to enter the stratospheric overworld (Holton

et al., 1995). Stratospheric WV is a strong greenhouse gas, small concentration fluctuations can slow or accelerate global warming up to 25% according to (Solomon *et al.*, 2010). The tropopause cirrus micro-physical properties dictate their ability to deplete the WV in excess and can influence the amount of WV entering the stratosphere (Jensen *et al.*, 2013).

Thin ice clouds are also known as *in situ* cirrus (Krämer *et al.*, 2016). TIC can form via two leading freezing processes : Homogeneous and heterogeneous freezing. The former occurs when hydrated aerosols freeze as the air parcel reach a critical RH_i threshold as a function of temperature (Koop *et al.*, 2000). Heterogeneous freezing occurs when ice nucleating particles (INP) initiate ice formation. The better understood homogeneous freezing process leads to higher Ni concentration. On the other hand, the presence of INP to activate ice formation at lower RH_i is needed for heterogeneous nucleation process to take place. In such regime the Ni concentration is correlated with the availability of INP. (Sullivan *et al.*, 2016) show that if there is a large amount of INP, the Ni amount also increases. For very low INP amount, homogeneous freezing will produce a large concentration of small IC. When the number of INP favours a strong competition between the two regimes, the resulting Ni reaches its lowest value and IC grow to larger sizes.

The nature of those INP and their nucleation properties are still misunderstood, it is still the subject of numerous studies. While kaolinite mineral dust is considered as a good INP, the presence of a sulphuric acid coating decreases their ice nucleation abilities at temperature below -40°C (Ansmann et Müller, 2005). (Sullivan *et al.*, 2010) show that this process was irreversible even after the neutralization of the acid by ammonium. Counterintuitively solid ammonium sulfate aerosols can act directly as INP and could favour a competitive regime (Abbatt *et al.*, 2006) lowering the cloud Ni amount and leading to a larger D_{eff} .

To calculate the Earth's atmosphere radiative energy balance in climate models, the water cycle in the cold and dry region of the atmosphere needs to be properly treated (Harries *et al.*, 2008). It is then of uttermost importance to understand the formation process leading to the different micro-physical properties of TIC.

While the last generation of space base remote sensing instruments dedicated at cloud observation such as CALIPSO (Winker *et al.*, 2003) and CloudSat (Stephens *et al.*, 2002), greatly improved the global observation of the TIC (Delanoë et Hogan, 2008) and enabled their studies in polar environment (Grenier *et al.*, 2009). Their coverage is still limited and restrained to a vertical cross section of the atmosphere. Passive remote sensing satellites, on the other hand, are used for imaging and enable the study of the horizontal structure of the clouds. The split window technique (Inoue, 1985) can retrieve the optical depth (τ) and the D_{eff} using the difference in brightness temperatures between two channels in the atmospheric window (BB) $11\mu m$ and $12\mu m$. The advance baseline imager, the visible and IR spectroradiometer on board of the last generation of operational satellites GOES-R, still use a similar method to retrieve the cirrus properties. More advance technique using the optimal effective method (OEM) (Rodgers, 2000), use all available channels to find the most likely state of the cloud. Those were implemented by (Wang *et al.*, 2016) using the Moderate Resolution Imaging Spectroradiometer (MODIS) (King *et al.*, 1992). While representing the state-of-the-art in space passive remote sensing, current IR retrievals are not suited to study cloud made of larger particles ($D_{eff} \geq 80\mu m$) (Merrelli et Turner, 2013), and the low surface emissivity during the polar night severely decrease their signal-to-noise ratio making accurate measurements difficult (Liu *et al.*, 2010).

(Baran, 2009), (Yang, 2003) and (Palchetti *et al.*, 2016a) have demonstrated the potential of the hyperspectral FIR measurement to retrieve TIC properties. Using the OEM (Libois et Blanchet, 2017) show that adding a few broadband

FIR channels to existing spaceborne radiometers would decrease the uncertainty on TIC retrieved value of τ and D_{eff} by 50%. The FIR part of the spectrum also include pure rotational bands of WV that coincide with a maximum in the WV continuum (Shine *et al.*, 2012). It is therefore extremely promising to monitor WV vapour in the cold and dry regions of the atmosphere (Shahabadi et Huang, 2014).

Despite the well demonstrated potential of the FIR to improve the remote sensing of the water cycle and the importance of this spectral region for the Earth's outgoing longwave radiation (Mlynczak *et al.*, 2005). There is currently no space-based instrument measuring this part of the spectrum. This was mostly due to previous technology limitations. FIR sensors had a lower responsiveness than their TIR counterpart. Recent availability of better technologies renewed interest for satellite missions in the FIR. The FORUM (Palchetti *et al.*, 2016b) satellite mission from the European Space Agency is specifically aimed at ice clouds. It is at the heart of the technologies used in the Radiation Explorer in the Far InfraRed Prototype for Applications and Development (REFIR-PAD) project (Palchetti *et al.*, 2006). This Fourier transforms interferometer (FTIR) has already been used to measure TIC radiative properties in a polar environment (Palchetti *et al.*, 2015). Other ground-based FTIR that explores this part of the spectrum also exist and are currently used. The E-AERI (Knuteson et Revercomb, 2004) covering wavelengths up to $25 \mu m$ enables the retrieval of Arctic cloud properties (Cox *et al.*, 2014) and (Mariani *et al.*, 2013). The Tropospheric Airborne Fourier Transform Spectrometer (TAFTS) (Canas *et al.*, 1997), was used to investigate the water vapour continuum (Fox *et al.*, 2015) and characterize snow emissivity (Bellisario *et al.*, 2017). The Far-InfraRed Spectroscopy of the Troposphere (FIRST) (Mlynczak *et al.*, 2006) aimed to constrain the radiative budget of the Earth in the FIR (Latvakoski *et al.*, 2013).

While hyperspectral FIR measurements from space are desirable from an earth's energy budget perspective, they might not be required for TIC and WV remote sensing. Most of the information needed to retrieve cloud properties can be gathered using few broadband FIR filters (Libois et Blanchet, 2017). The Thin Ice Clouds in Far InfraRed Experiment (TICFIRE) satellite project (Blanchet *et al.*, 2011), sponsored by the Canadian Space Agency (CSA), focuses on the observation of the TIC and the water cycle during the polar night. Using 9 broadband channels and a new uncooled detector technology the whole instrument is small enough to fit inside a micro-satellite resulting in an overall low-cost mission. Designed as an imager with a ground pixel of 10 km, a swath of 600 km and a fast acquisition speed, TICFIRE would be able to resolve the TIC micro-physics spatial fluctuations.

To support the TICFIRE project, CSA sponsored the development of a prototype, the Far InfraRed Radiometer (FIRR) (Libois *et al.*, 2016b) to test the technologies that will be used for the satellite mission. The FIRR was designed as a nadir viewing airborne instrument and performed its first measurement in the Arctic during the 2015 aircraft campaign of the Network on Climate and Aerosols : Addressing Key Uncertainties in Remote Canadian Environments (NETCARE) (Abbatt *et al.*, 2019).

In October 2015 the FIRR was deployed at the Eureka weather station (EWS). It was fully operational at the end of February 2016 after the repair of a critical component. The Eureka ground campaign had the goal to prove the viability of a zenith pointing FIR radiometer. The FIRR's performance was compared to already proven instruments and was also tested for its ability to work in a very cold environment. A second objective was to assess the FIRR's sensitivity to different atmospheric variables such as temperature and humidity, and ice cloud properties. In this study, we present the instrument design, its calibration, and quantify its

radiometric resolution. Following this, using FIRR data acquired from 24/02/2016 to 30/03/2016, the ability to retrieve the PWV and discriminate TIC based on their micro-physical properties is evaluated.

This paper is structured as follows. The first section is an overview of the FIRR instrumental design as well as an extensive description of the signal processing and calibration use for the data acquired during the campaign. The second section offers an overview of the Eureka site, the general winter climatology and the weather during the FIRR operation, a technical description of collocated instruments as well as their data processing. In the third section, simulated downwelling radiance from a radiative transfer model (RTM) are compared with a FTIR measured spectra and with the FIRR broadband measurements the FIRR radiometric resolution and accuracy are evaluated and quantified through an inter-comparison with a FTIR and the simulated spectra. The sensitivity of the FIRR to the integrated water vapour column is investigated in the fourth section, followed by a description and evaluation of a PWV retrieval. In the fifth section, the response of the FIRR to varying cloud structures and optical properties is analyzed for 4 specific cases. Then using parameters derived from the FIRR measured BT, its ability to discriminate TIC based on their micro-physical properties. Summary and conclusion are presented in the last section.

1.2 The Far InfraRed Radiometer

This section provides an overview of the technical characteristics of the FIRR, the signal processing of the raw data and the calibration algorithm leading to level 2 radiance products. A more complete description of the instrument is given by (Libois *et al.*, 2016b).

1.2.1 Technical Characteristics

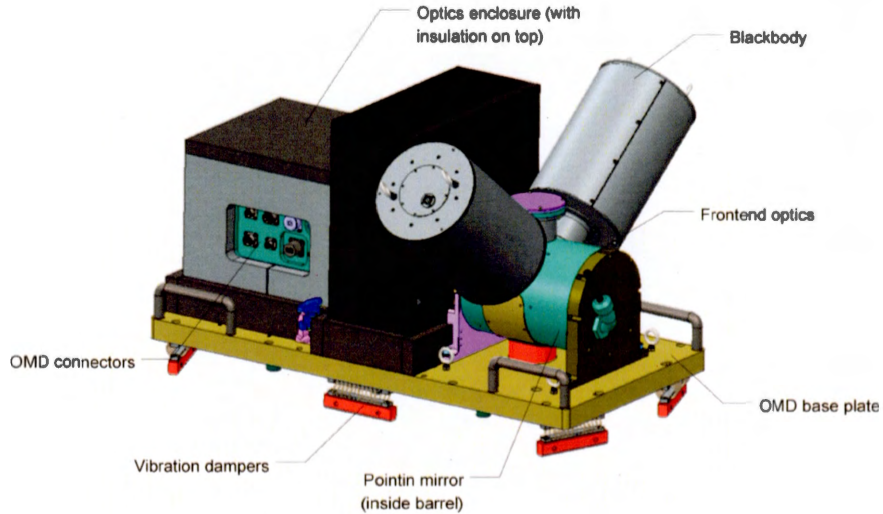


FIGURE 1.1: Schematic of the FIRR Optomechanical Device from (Libois *et al.*, 2016b).

The optomechanical device (OMD) shown in fig :1.1 represents the active part of the instrument. It is operated through the instrument control device (not discussed in this paper). The OMD can be divided into two distinct parts. The front end is composed of a gold-coated scene selecting mirror (SSM) located inside a rotating barrel. In the configuration used at Eureka, the SSM can point at 3 directions, the two black bodies (BB) and the sky view (SV). When in SV the FIRR has a 6° field of view centred on the zenith. The two BB are used for the calibration, the Ambient BB (ABB) is stabilized just above the ambient temperature. While the hot BB (HBB) is maintained at a temperature of 15 K to 30 K above the ABB. Each BB temperature can be controlled in a range of -30°C to 60°C with a 5 mK accuracy. The coating inside the BB has a well-characterized spectral reflectance in the FIR which is used to calculate its emissivity (Rochette *et al.*, 2009).

The SSM redirect the light to the back end part of the OMD. To maximize the

transmitivity, the optical path between both parts is a fully open configuration without any physical barrier. The back end portion enclose a rotating motorised filter wheel, used to select the spectral channel to be measured. It hosts 8 interference filters and 1 mesh filter, described in section 1.2.2, covering a spectral range between $(8 - 50)\mu m$. The spectral transmittances for each filter are shown in fig : 1.2. After passing through the filters wheel, the optical beam is focused by a Schwarzschild mirror telescope on the illuminated part of the detector, which is a 2-dimension array of $(80 \times 60 \text{ pixels})$, uncooled gold-black plated microbolometer developed at INO (Institue National d'optique) (Ngo Phong *et al.*, 2015). The gold-black coating ensure a better absorbance of the detector surface. The material has been proven to have a reflectance below 1% in the wavelength range (6 to $12.5 \mu m$) and below 6% in the range (12.5 to $80 \mu m$). The detector is designed to operate at room temperature and is thermally stabilized by a Pelletier effect cooler at $15^\circ C$ (Ngo Phong *et al.*, 2015). A similar detector is used in the broadband radiometer of the EarthCARE mission (Proulx *et al.*, 2009) where the same technology is used in a fully open configuration. This can only be done in the vacuum of space. The FIRR detector is vacuum sealed behind a vapour deposition diamond window that ensures a uniform transmittance in the measured spectral range. Even if the goal of this technology is to be used as an imager, the current design of the FIRR only use the illuminated portion of the detector as a single pixel. The illuminated part comprises ~ 300 pixels in a circular pattern located in the region of the detector with the gold-black coating of the best quality. In this study we use, 193 pixels, forming a circle fully encompasses at the centre of the illuminated part of the detector. This is to avoid using pixels at the edge of the illuminated area, which is subject to lower or inconsistent gain due to optical effects. Those pixels are from now on referred to as the illuminated pixel (IP). The detector is read by the IRXCAM from INO at 120 Hz. A scene measurement takes less than 1s and usually consist of the acquisition of 70 to 100 frames.

1.2.2 Filters

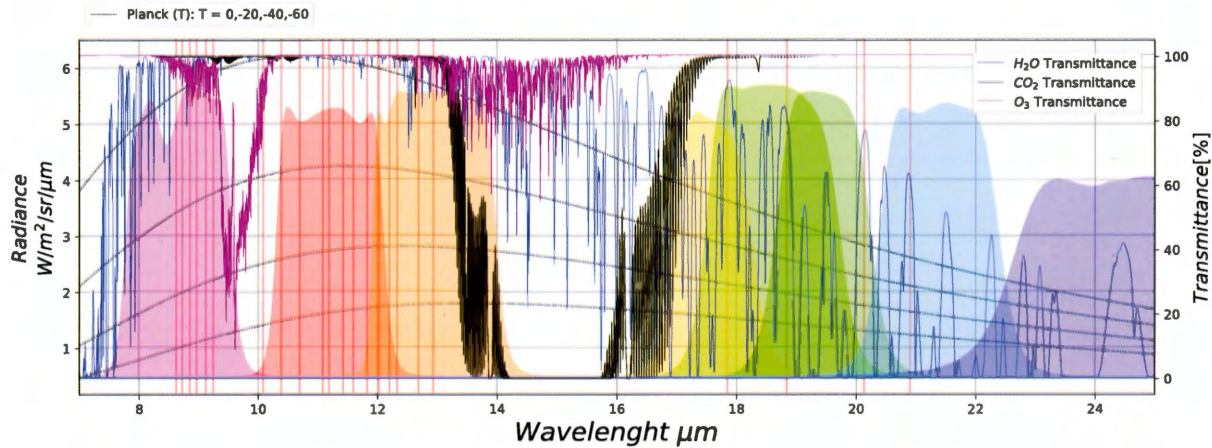


FIGURE 1.2: FIR filters and atmospheric gas absorption.

Filters spectral transmittance function (colour fill), overlaid to the spectral transmittance of a 1m optical path at 1000[hpa] for three atmospheric gases.
 O_3 (purple line), CO_2 (black line), H_2O (blue line), Micro-windows (thin red line).
 Planck's function (black lines).

As shown in fig : 1.2 8 of the 9 filters of the FIR filter span from 8 to 25 microns, covering part of the spectrum that is mainly influenced by 3 atmospheric gases, H_2O , CO_2 and O_3 . They are split in two categories, the Thermal Infrared (TIR) channels consist of 3 filters with wavelengths shorter than $15\mu m$:

- $(7.9 - 9.5)\mu m$: Encompasses the first portion of the atmospheric window. It is sensible to the ozone profile and slightly overlap with the wing of the $6.7\mu m$ H_2O bands and is therefore sensible to the temperature and WV.
- $(10 - 12)\mu m$: Located in the middle of the atmospheric window, the most transparent portion of the atmosphere, it is only sensible to the optical depth and effective temperature of either clouds or haze.

- $(12 - 14)\mu m$: Partially overlaps with the main CO_2 band, making it sensible to the temperature profile and the optical depth of the atmosphere.

The Far Infrared (FIR) filters are looking at wavelengths passed the $15\mu m$ CO_2 band, 4 of them are located in the so-called dirty window in the vicinity of the $20\mu m$ wavelength, while 2 of them cover longer wavelengths. They are defined as follows :

- $(17.25 - 19.75)\mu m$: Because of the inclusion of multiple micro-windows, This FIR filter is the less sensitive to the WV.
- $(17 - 18.5)\mu m$: Contains a lot of strong H_2O rotational bands. It also weakly overlaps with the wings of the CO_2 main band, making it sensible to the temperature profile even in a perfectly dry atmosphere.
- $(18.5 - 20.5)\mu m$: Having the peak of its transmittance located right between two micro-windows this filter is more sensible to WV than the previous one even if a large part of their ranges overlaps.
- $(20.5 - 22.5)\mu m$: Micro-windows in this band also start to have a very weak transmittance due to the WV continuum.
- $(22 - 27)\mu m$: Strongly affected by the H_2O lack of transmittance in those wavelengths and is therefore sensible only to the lowermost part of the atmosphere.
- $(30 - 50)\mu m$: Not shown in fig :1.2 and fig :1.3 This filter was designed to be used from a satellite perspective. From a ground zenith point of view, the atmosphere as an almost null transmittance in those wavelengths, therefore this band measured radiance is always corresponding to the one emitted by

a BB at a temperature matching the lowermost level of the atmosphere. For this reason this filter will be mostly left out of this study.

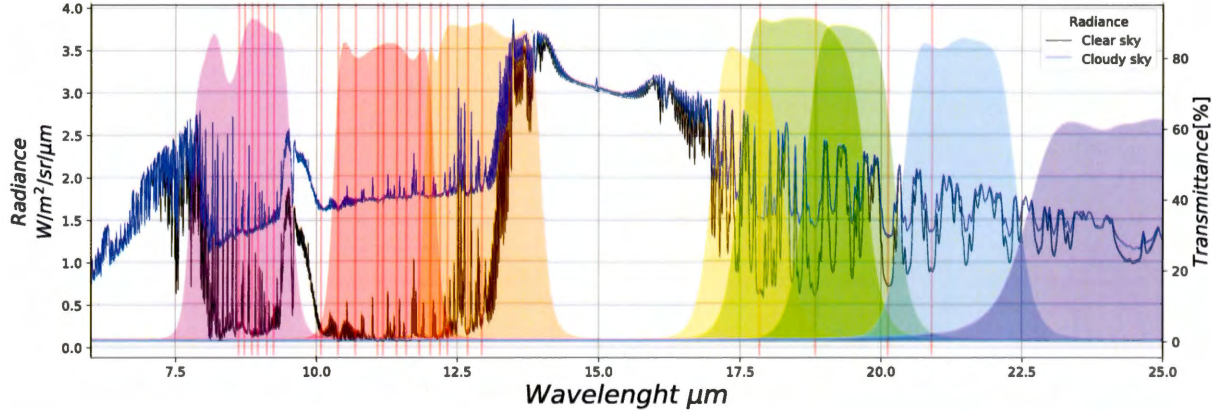


FIGURE 1.3: FIR filters and examples of downwelling radiances.

Filters spectral transmittance functions (colour fill), overlaid to the spectrally resolved downwelling radiance of a clear sky (black line) and TIC covered (blue line). Micro-windows (thin red line). Downwelling radiance measurements are from the E-AERI dataset, respectively from February 28 and March 6, 2016, in Eureka, NU.

Also shown in fig : 1.2 the Planck function for 4 temperatures. One can see that while the Planck function totally collapses at low temperature in the $6.7\mu\text{m}$ WV band, it only loses two third of its intensity in the FIR. By the Wien displacement law the maximum of radiation emitted by a BB shifts toward longer wavelengths for colder temperature. The FIR is then well suited to detect WV in a cold atmosphere, where the TIR signal-to-noise ratio drastically decreases.

Fig : 1.3 shows that the FIR filters spectral transmittance functions overlap to spectrally resolve downwelling radiance measured by the E-AERI, one for a clear sky and another for a TIC cover. The figure also includes the micro-windows

(MW) used in (Turner, 2005) to retrieve cloud properties. Most of those windows are located in the AW and are covered by the TIR filters, but the FIR part of the spectrum also includes MW between the WV rotational bands, where the atmosphere has a higher transmittance. In the FIR, the distinction between the CS and cloud cover is only distinguishable through those MW. Hence all of the FIR filters include at least 1 of such MW, making them sensible to the optical properties of clouds.

1.2.3 Instrumental Setup



FIGURE 1.4: FIRR installation at OPAL

The FIRR instrument (shown in fig : 1.4) was installed in the ØPAL laboratory using a through wall configuration with an opening in the wall allowing a fully open optical path. The part of the OMD located outside of the laboratory was protected by an enclosure built by LR-Tech. At the top of the enclosure, the automatic hatch, linked to the precipitation sensor just beside it, is used to protect

the instrument during precipitation events. A positive pressure is maintained in the hatch to avoid undetected precipitations to fall inside. The front-facing part of the enclosure is usually covered during operation but was left open for the demonstration.

1.2.4 Signal Processing

In this study, as opposed to the calibration procedure described in (Libois *et al.*, 2016b), the raw data from the FIRR are subject to extensive signal processing prior to the calibration. All of the frames and pixels from a raw reading of the detector by the camera are processed to obtain a single numerical value for each SSM positions. For each spectral bands of the FIRR, a measurement sequence is composed of 3 SSM positions, one for each FIRR point of view *SV*, *HBB* and *ABB*. For every SSM positions the detector is read by the camera for 0.83s, leading to the acquisition of 100 subframes of the detector 60x80 array that will be referred here as a full frame ${}^v\lambda FF$ were λ is the spectral band and v the SSM position. Each pixel's information is stored as a short integer that is called a count. A pixel count variation corresponds, in a linear manner, to a change in radiance absorbed by the pixel surface.

To compute the calibration as if the FIRR detector was a single pixel, each ${}^v\lambda FF$ is converted to a single corrected count ${}^v\lambda C$ value. To do so, a signal processing algorithm has been developed, taking into account the results from (Libois *et al.*, 2016b). Each pixel contained in a ${}^v\lambda FF$ can be written as ${}^v\lambda X_s^p$ where p is the pixel position in the (60 X 80) array and s the subframe to which it belongs.

$$\langle {}^v\lambda X_s^p \rangle = \frac{1}{n} \sum_p^n ({}^v\lambda X_s^p) \quad (1.1)$$

A ${}^v\lambda FF$ can be spatially averaged using eq : 1.1 where all 4800 pixels of each subframe are averaged together, resulting in a time series of single count.

$$\sigma^s({}^v\lambda X_s^p) = \sqrt{\frac{1}{n} \sum_p^n ({}^v\lambda X_s^p - \langle {}^v\lambda X_s^p \rangle)} \quad (1.2)$$

The standard deviation of this time series is computed through eq :1.2, where n is the number of selected pixels in each subframe.

$$|{}^v\lambda X_s^p| = \frac{1}{n} \sum_s^n ({}^v\lambda X_s^p) \quad (1.3)$$

$$\sigma^t({}^v\lambda X_s^p) = \sqrt{\frac{1}{m} \sum_s^n ({}^v\lambda X_s^p - |{}^v\lambda X_s^p|)} \quad (1.4)$$

An ${}^v\lambda FF$ can also be temporally averaged using eq : 1.3 and the temporal standard deviation is computed with 1.4, where m is the number of sub-frames.

During an acquisition sequence the vast majority of the subframes spatial average had almost the same count value ± 0.5 . A camera reading failure of a subframe always resulted in a very low or very high spatial average value compared to the previous and next subframe. To eliminate the bad subframes resulting from camera reading failure, all subframe not satisfying the condition : $(\langle {}^v\lambda X_s^p \rangle - {}^v\lambda \bar{X}) < (2 \cdot \sigma^t(\langle {}^v\lambda X_s^p \rangle))$ where ${}^v\lambda \bar{X} = |\langle {}^v\lambda X_s^p \rangle|$ are removed from the original ${}^v\lambda FF$. This criterion implied that, if the subframe spatial average deviated from the mean by more than twice the temporal standard deviation of all subframes spatial average this subframe was removed from the frame time series. This threshold ensured that all bad subframes were removed while keeping the highest number of good subframes.

Electronic noise affecting a single micro-bolometer in the array where resulting in a strong single pixel counts temporal fluctuations. To avoid keeping pixels affected by too much electronic noise, those not satisfying the condition : $\sigma^t(v_X^p_s) > 6$ are removed from the $v_{\lambda}FF$. The threshold of a temporal standard deviation of 6 was selected through trial and error, and gave the best results. A lower threshold would have removed good subframes from the frame time series.

Only pixels satisfying both conditions are considered good pixels. Afterwards the good pixels contained in the illuminated pixel (X_s^i) area of the detector are extracted from the array. A similar number of good non-illuminated pixels (X_s^{ni}), were also extracted from the detector dark region.

$$v_{\lambda}X^i = \lambda \left| X_s^i \right| ; \quad v_{\lambda}X^{ni} = \lambda \left| X_s^{ni} \right| \quad (1.5)$$

Through eq :1.5 a pair of $v_{\lambda}X_s^i$; $|v_{\lambda}X_s^{ni}|$ is obtain for each $v_{\lambda}FF$. Correlated count fluctuations over the whole array of the micro-bolometer have been observed by (Libois *et al.*, 2016b), the hypothesis being that this is due to fluctuations of the thermal state of the detector material. Very rapid fluctuations ($t < 1s$) are removed by the temporal averaging over the $v_{\lambda}FF$. While slow thermal fluctuations ($t >$ full sequence duration) are processed through the calibration. Since this noise was demonstrated to be correlated over the whole detector array, to remove fluctuations that fall in between the two categories, the spatial average X^{ni} is subtracted to the spatial average X^i as shown in :

$$C_{\lambda}^v = \left\langle v_{\lambda}X^i \right\rangle - \left\langle v_{\lambda}X^{ni} \right\rangle \quad (1.6)$$

The corrected count value $v_{\lambda}C$ associated with each FIR filters and SSM positions is then obtained and will be used to retrieve the measured radiances. After the

signal processing, a full-measurement sequence includes 27_{λ}^vCC ($3SSM*9Filters$) each $_{\lambda}^vCC$ is stored as 64-bit floating-point format representing 0,216Ko as opposed to the original raw files of 26 Mo.

Throughout the campaign filters wheel misplacements were randomly occurring due to a design flaw in the instrument. The resulting misalignment between the filter and the telescope resulted in a signal inhomogeneity over the detector illuminated area. The spatial standard deviation of such frame always exceeded 20 counts. To remove such event from the measurement, the following conditions : $\sigma_s(\frac{HBB}{\lambda}X^i - \frac{ABB}{\lambda}X^i) < 20$ $\sigma_s(\frac{HBB}{\lambda}X^i - \frac{SC}{\lambda}X^i) < 20$ needed to be fulfilled or the whole sequence for this filter was discarded, since all SSM positions are required to perform the calibration.

1.2.5 Calibration

Since the detector of the FIRR collects radiance from not only the scene view, but also from inside the field of view of the detector, including the optical path between the pointing mirror and the detector surface. The calibration process needs to be performed frequently, since a slight temperature change of the optical path produce a change in measured radiances. Thus for every MS the true radiance of the SV is computed from a two-point calibration using the ABB and HBB, assuming a linear relationship (e.g (Revercomb *et al.*, 1988)). Here, we describe the method to retrieve radiances from the measurements of ABB and HBB references, and from SC corrected counts obtained after the signal processing.

$$L_{\lambda}^{BB} = \int_{\lambda} \tau_{\lambda}(\lambda') \frac{2hc^2}{\lambda'^5} \frac{\varepsilon(\lambda')}{e^{\frac{hc}{\lambda' k_b T_{BB}}} - 1} d\lambda' \quad (1.7)$$

First the radiance emitted by each BB, L_{λ}^{BB} for a filter centred at a wavelength λ is

given by eq : 1.7, where $h = 6.63 \times 10^{-34} Js$ is the Planck constant, $c = 3 \times 10^8 ms^{-1}$ is the speed of light, $k_b = 1.38 \times 10^{-23} JK^{-1}$ is the Boltzmann constant, λ' is the wavelength and τ_λ is the normalized transmittance of the filter λ .

Using the BB temperature T_{BB} and emissivity ε , their theoretical spectrally resolved radiances are computed using the Planck function. Then the computed spectrally resolved radiances are convoluted with the normalized spectral transmission function of the corresponding filter λ , as shown in fig :1.3.

Taking into account that the response of the detector varies linearly with the scene radiance as demonstrated in (Libois *et al.*, 2016b), we can express C_λ^{BB} as follows :

$$C_\lambda^{BB} = B_\lambda^{BB} + G_\lambda L_\lambda \quad (1.8)$$

The gain of the detector G_λ can be computed from :

$$G_\lambda = \left| \frac{C_\lambda^{HBB} - C_\lambda^{ABB}}{L_\lambda^{HBB} - L_\lambda^{ABB}} \right| \quad (1.9)$$

and the background B_λ is obtained from :

$$B_\lambda = C_\lambda^{ABB} - G_\lambda L_\lambda^{ABB} \quad (1.10)$$

To take into account the variation of the background during the MS and assuming a linear time dependence, then the R_λ term representing the variation of B_λ is found from :

$$R_\lambda = C_\lambda^{HBB} - B_\lambda - G_\lambda L_\lambda^{HBB} / \Delta t_{HBB} \quad (1.11)$$

Where Δt_{HBB} is the time lag between the acquisition of C_λ^{ABB} and the C_λ^{ABB} measurement. The radiance L_λ^{SV} from the SV for the filter λ is then retrieved using :

$$L_\lambda^{SV} = \frac{C_\lambda^{SV} - B_\lambda - R_\lambda \Delta t_{sv}}{G_\lambda} \quad (1.12)$$

It is also possible to use the BB measurements from the next sequence MS_n for computing G_λ . If another MS is available after the first one we can use the next ABB measurement to take into account the background variation during the first MS, eq : 1.9 then becomes :

$$G_\lambda = \left| \frac{\Delta t_{NBB}(C_\lambda^{HBB} - C_\lambda^{ABB}) - \Delta t_{HBB}(C_\lambda^{HBB} - C_\lambda^{ABB})}{\Delta t_{NBB}(L_\lambda^{HBB} - L_\lambda^{ABB}) - \Delta t_{HBB}(L_\lambda^{NBB} - L_\lambda^{ABB})} \right| \quad (1.13)$$

Where NBB is the next ABB measurement and Δt_{NBB} is the time lag between the acquisition of C_λ^{ABB} and C_λ^{NBB} . The SV measurement being taken between the two BB measurements the G_λ retrieve by 1.13 taking into account the change in the detector gain during the MS.

This calibration procedure varies from (Libois *et al.*, 2016b), where the correlated noise between the IP and NIP was subtracted during the calibration. In this study the correlated noise had already been removed during the signal processing in the section 1.2.4.

To simplify comparisons between each filter, it is convenient to express their measurements in terms of brightness temperature (BT), which is the temperature of a perfect BB emitting the same radiance (L_λ^{BB}) as the one computes in eq : 1.7 for a filter λ .

1.3 The Eureka Campaign

The Eureka weather station (EWS) is located in Nunavut Canada at N $79^{\circ}59'20''$, O $85^{\circ}56'27''$ and is operated by the Meteorological Service of Canada (MSC). Environment and Climate Change Canada (ECCC), The Canadian Space Agency (CSA) and the Canadian Network for the Detection of Atmospheric Changes (CANDAC), a collaboration between 9 Canadian universities departments, operate a suite of instruments on three local sites : the Polar Environment Atmospheric Research Laboratory (PEARL), the Surface and Atmospheric Flux Irradiance and Radiation Extension (SAFIRE) and the Zero-altitude Pearl Auxiliary Laboratory (\emptyset PAL). Eureka is located deep inside the polar vortex with polar winter conditions. It is monitored by frequent sun-synchronous satellites including CLOUDSAT and CALIPSO. The site is strategically located for Arctic study and dense satellite overpass (Batchelor *et al.*, 2009).

1.3.1 Climatology

At N 80° , Eureka experience a full 4 months of polar night each year. The sun sets around the October 20th and rises again around the February 20th. With an annual average temperature at sea level of -20°C , Eureka is one of the coldest locations in the northern hemisphere. During the winter month (DJFM), the average monthly temperatures are below -35°C , reaching a minimum of -38°C in February (Lesins *et al.*, 2010). This is driven by strong radiative cooling to space, since the average PWV during the night, remains below 2[mm] throughout winter(Weaver *et al.*, 2017). A very dry atmosphere allows a substantial fraction of emitted radiation from the ground to escape to space. As a result, during the dark months a strong surface temperature inversion is maintained, leading to a layer of strong stability above the ground. The air layer near the ground is cooled from

the negative radiation balance of the surface, resulting in a strong temperature inversion of the boundary layer (Curry et Curry, 1983). During spring, Eureka and the Arctic in general are subject to «arctic Haze» episodes, which is composed of highly acidic sulfate aerosols. They are formed when a long-range transported SO_2 , is oxidized especially when exposed to visible light after polar sunrise (Sirois et Barrie, 1999). The haze layers are often present in the warmest part of the atmosphere where the highest water vapour concentration is located. However, aerosols can be transported higher up by low-pressure systems induced vertical motion.

(Cox *et al.*, 2014) have studied cloud optical properties observed at Eureka between 2006 and 2009, using the Polar-Atmospheric Emitted Radiance Interferometer (P-AERI) (Knuteson et Revercomb, 2004), and applying the MIXCRA algorithm from (Turner, 2005). During winter at Eureka, from December to April, the fraction of liquid cloud is normally below 4%. Mixed phase cloud accounts for 20% to 45% of events, with a maximum in February and the minimum in March. The average ice fraction in mixed-phase clouds is typically within 50% - 60%, but it shows higher variation, especially in March. The cloud optical depth (COD) or (τ), never exceed 6 and more than half of the clouds are within[0 - 1] range, for both ice only and mixed phase clouds. The winter conditions affect significantly the surface radiation budget (Mariani *et al.*, 2016). In the AW ($10\mu m$) average clear sky (CS) BT varies only slightly from summer to winter, between 200K and 175K. Otherwise, the average BT in the $(17-34)\mu m$ range, the so-called dirty window (DW), varies from 275K to 180K, clearly showing the weakening of the DW during the month with lowest PWV. Thinner clouds during winter affect Cloud Radiative Forcing (CRF). From October to April, the sky BT in both windows is modulated by the presence of thin cloud layer, increasing only by about 5% in the AW, and 10% in the DW. During summer, the thin cloud CRF in the AW

is more substantial, increasing by 25[K]. The DW experience little CRF during the summer, even for optically thick clouds. The higher amount of low-level WV limits the clouds radiation reaching the surface in this spectral region. Eureka, with extended cold and dry winter conditions is a favoured location for testing the FIRR.

1.3.2 ØPAL

The Zero-altitude Pearl Auxiliary Laboratory ØPAL is located only 100 m away from the EWS at an elevation of 15 m above sea level, and houses a comprehensive set of collocated instruments for probing the atmosphere. The technical characteristics and data processing of each passive and active remote sensing instrument used in this study are described below.

E-AERI

The Extended-range Atmospheric Emitted Radiance Interferometer (E-AERI) is an FTIR instrument measuring the absolute downwelling spectral radiance the range between 5 and 25 microns ($400 - 3000 \text{ cm}^{-1}$) at a resolution of 1.0 cm^{-1} (Mariani *et al.*, 2012). The E-AERI stands for the extended version of the AERI (Knuteson et Revercomb, 2004), adding the $(20 - 25)\mu\text{m}$ range to the basic AERI version. A full scan cycle of the spectrum requires 7 minutes. The AERI was developed by ABB under a commercial license with the University of Wyoming. The E-AERI has 2 detectors kept at 70K using a Stirling-cycle cryo-cooler. It uses the same two-point calibration as the FIRR.

The FIRR and the E-AERI are installed side-by-side at ØPAL. The front end optic of the E-AERI is very similar to that of the FIRR. A pointing mirror can rotate from the zenith view to each of the 2 BB used for the two-point calibration. The

back end optic located inside the laboratory is sealed from the outside environment by an IR transmitting window. This installation differs from the FIRR by the fact that the E-AERI back end enclosure is fully sealed and it is controlled to maintain a constant temperature. Thus as a requirement, the E-AERI instrument is thermally more stable than the FIRR. In 2009 CANDAC installed the E-AERI at ØPAL, where it is acquiring nearly continuous data since February 2011. Prior to the installation of the E-AERI, the polar version of a standard AERI was used at ØPAL. For a period of 7 months, both instruments were used side-by-side. During this period, the radiance from $(5\text{-}20)\mu\text{m}$ taken by both AERI instruments shown consistent results(Mariani *et al.*, 2012). The E-AERI is a well characterized and proven reference instruments for FIRR validation. It is conveniently located within 10 metres from the FIRR. The spectrum measured by the E-AERI fully overlaps with 7 of the 9 bands of the FIRR. Therefore, we use it to assess the radiometric resolution and the accuracy of the FIRR during our 4 months ground campaign.

The temporal resolution of the E-AERI is slower than the FIRR, a full scan of E-AERI needs 7 minutes to perform a full cycle, while the FIRR take usually less than 3 minutes During winter the sky condition at Eureka, in absence of convection, is generally evolving slowly, the resolution of the E-AERI is fast enough to provide a reliable comparison with the FIRR in clear and cloudy scenes.

E-AERI data were provided by the research group of Prof. Kim Strong from the University of Toronto.

Radiosonde Profiles

A radiosonde flight is released twice a day (1115UTC and 2315UTC) by MSC as part of the regular operation of the EWS. The sonde type used by ECCC is the

Vaisala RS-92 (Vaisala, 2013). In cold temperature and low humidity conditions, the radiosondes atmospheric data need to be corrected prior to their use. Raw data profiles have been extracted from the binary file generated by the Vaisala acquisition system, using the software from the GCOS (Global Climate Observing System) Reference Upper-Air Network (GRUAN) (Dirksen *et al.*, 2014) group.

First, because the response of the thin-film capacitor to temperature fluctuations is not instantaneous, the resulting RH measurements must be corrected. This method is called the "time-lag correction" and is described in (Miloshevich *et al.*, 2004). During winter in Eureka, the strong vertical temperature gradient near the surface, makes this correction mandatory. As shown by (Rowe *et al.*, 2008), this model of radiosonde processing produces a dry bias at low temperature. Starting at a pressure level of 700 hPa, to correct this bias, a second algorithm describe by (Miloshevich *et al.*, 2009) is applied to the sounding data. We note that only the night-time RH correction has been used for all of the radiosonde profiles during the campaign. This is due to the daily solar bias correction in (Miloshevich *et al.*, 2009) that has been developed for the mid-latitudes conditions, and not validated in the Arctic cases where low solar angle as well as strong surface albedo adds uncertainty to the solar heating of the RS-92 humidity sensor. Taking account of the night-time dry bias is essential to retrieve reliable vertical profiles. Moreover, at this time of the year very few radiosonde launches were performed during daylight. In the mid-latitudes, the RH correction mostly applies in the high troposphere and stratosphere, but in the high Arctic the low temperature and dry conditions lead to correction over the whole troposphere. As shown in fig.1.5, the corrected vertical profile better matches the lidar observation. The RH_i corrected dataset at the top of the cloud reaches values near 160%, while for the non-corrected data, the RH never reaches that level for ice supersaturation. Such high values are expected to be present at the top of thin ice clouds (Krämer *et al.*, 2016). On the opposite, the

dry layer of the corrected profile at 7200 metres, better matches the altitude where the lidar backscatter signal has lower values due to the ice crystals sublimation in the sub-saturated air. In clouds, RH_i is a critical value to characterize the cloud micro-physical dynamics (Jouan *et al.*, 2014).

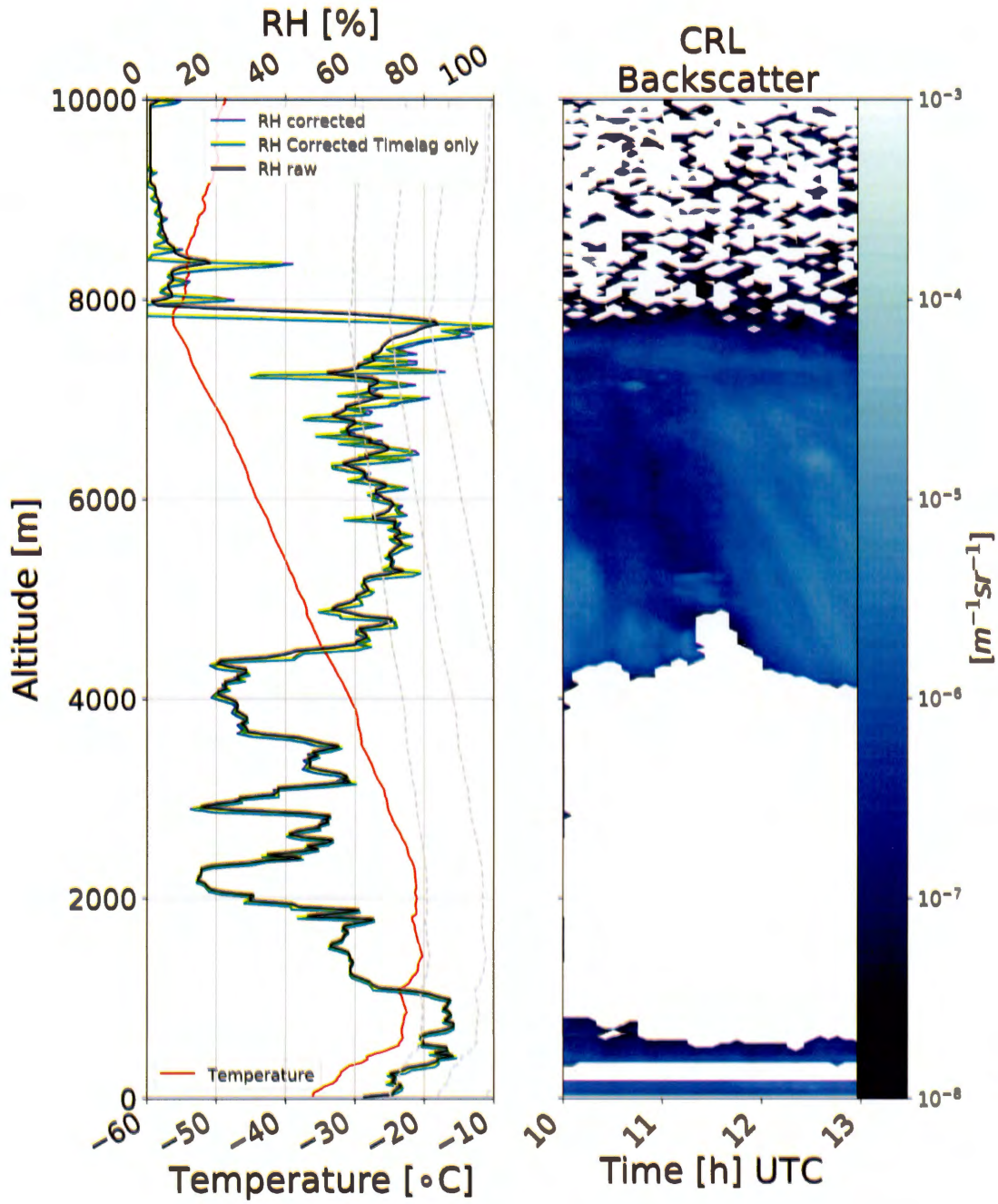


FIGURE 1.5: Comparison with the CRL and the radiosonde corrected profile.

Left : Atmospheric temperature profile on March 27, 2016, 1200UTC raw sounding, including corrected and non-corrected RH profile. Corresponding values of $RH_i = 100\%, 120\%, 140\%, 160\%$ (light grey dash line) and temperature profiles (red line) are shown. Right : Corresponding time series of the CRL Backscatter profile for the period around of the launch of the radiosonde.

MMCR

The millimetre-wave cloud radar (MMCR) is a zenith pointing Ka-band 35-GHz (8.6mm wavelength) radar (Moran *et al.*, 1998). It measures the 1st, 2nd and 3rd Doppler moment of the cloud hydrometer up to 15 km. The MMCR was first deployed at Eureka in 2005 by the Atmospheric Radiative Measurement (ARM) as part of the suite of instruments from the ground base multi-sensor cloud phase classifier (Shupe, 2007). They were used as part of a pan-Arctic study (Shupe, 2011). Unfortunately from the original full suite of instruments, only the MMCR remains active. The Microwave Radiometer (MWR) (Turner *et al.*, 2007) still acquire data, but have been shown out of calibration since 2010(Weaver *et al.*, 2017). The Arctic High Spectral Resolution Lidar (AHSRL) (Eloranta et Ponsardin, 2001) was removed from the site in 2012. The MMCR can be used in 4 modes : Boundary layer, stratus, cirrus and general case. The ARSCL algorithm (Clothiaux *et al.*, 2000) is normally used by ARM to optimally combined each mode. However data from the MMCR¹ at Eureka is not processed by the ARM anymore, only the calibrated 1st, 2nd and 3rd Doppler moment for each mode is available on the ARM database. Therefore, in this study, only the general mode is used. Since ice crystal from the clouds are usually smaller than 1mm, the radar backscatter (β_r) follows the Rayleigh regime. As suggested by (Donovan et Van Lammeren, 2001) we use the MMCR measured reflectivity Z and the complex index of refraction of ice $n_i = 1.785$ to retrieve the β_{radar} from :

$$\beta_{radar} = \frac{\pi^4}{\lambda_{radar}^4} \frac{|K|^2}{4} Z \quad (1.14)$$

¹The data are archived on the ARM website : <https://www.arm.gov/data>

where :

$$K = \frac{n_i^2 - 1}{n_i^2 + 1} \quad (1.15)$$

and λ is the MMCR wavelength.

The MMCR reflectivity Z is given as decibel relative to Z :

$$dBZ = 10 \cdot \log_{10} Z \left[\frac{mm^6}{m^3} \right] \quad (1.16)$$

To compute the β_{radar} it needs to be converted to SI units using :

$$Z = 10^{\frac{dBZ}{10} - 18} \quad (1.17)$$

Because of the long wavelengths of the MMCR with respect to the crystal size D_{eff} , the instrument is not sensible to ice crystal smaller than $40\mu m$ in diameter and can fail to detect clouds with low concentration of smaller IC.

CRL Lidar

The CANDAC Raman Lidar (CRL) is a Rayleigh-Mie-Raman lidar operating at two wavelengths, a visible beam at 532.08nm and a UV beam at 354.72nm (Nott *et al.*, 2012). For the 2016 CANDAC sunrise campaign, the CRL was operational most of the time over the 4 months of the study with few periods of down time. Unfortunately, only the 532 nm channel was operating. It was not possible to retrieve the lidar aerosol backscatter (β_l) through the Raman profile of nitrogen (Ansmann et Müller, 2005). Instead β_l is retrieved using the Klett inversion technique (Klett, 1985). It is less precise and its use as an input in

the D_{eff} retrieval algorithm from (Donovan et Van Lammeren, 2001) was shown inconsistent and unusable. Still the retrieved β_l and β_r can be used to classify the two types of TIC above ØPAL following criteria from (Bourdages *et al.*, 2009) see section 1.6.1. In this study when the β_l is not available, then the range-corrected photo-counts is used instead. While not identical to the β_l , nonetheless it follows the same response function to the presence of a cloud. The linear depolarization ratio from the CRL was obtained by the algorithm described in (McCullough *et al.*, 2017). All the CRL measured quantities were processed and provided by CANDAC.

1.3.3 Weather

Fig : 1.6 shows the time series of the atmospheric profiles at Eureka during the campaign from the surface to 14000 m. In the first panel, one can see that the surface temperature inversion is maintained during most of the campaign. The level of maximum temperature is usually located just below 2000 m and episodes of warm air advection below 6000 m are occasionally seen. Those periods are generally associated with an increased moisture concentration. As shown by (Doyle *et al.*, 2011), Eureka is subject to periods of higher PWV due to WV intrusion from lower latitudes, advected from the South by synoptic low-pressure systems. Weaker vertical gradient of potential temperature in the troposphere and a colder tropopause is also associated with those warm air intrusions and vertical motion associated with warm fronts. As a result, a local minimum in surface pressure and geopotential height follows increasing temperature. The temperature minimum associated with the tropopause is usually located between 10000 m and 8000 m. Episodes of a less define tropopause can be seen from March 1 to 5 of and March 9 to 17. This coincides with the week surface temperature inversions and results in a strong vertical gradient of the potential temperature over the whole

troposphere. Increase in the PWV is often followed by an increase in surface temperature. After March 19, the vertical temperature profile is subject to fewer variations. Low PWV leads to a strong and sustained surface inversion. Potential temperature profile shows a high stability over the whole troposphere.

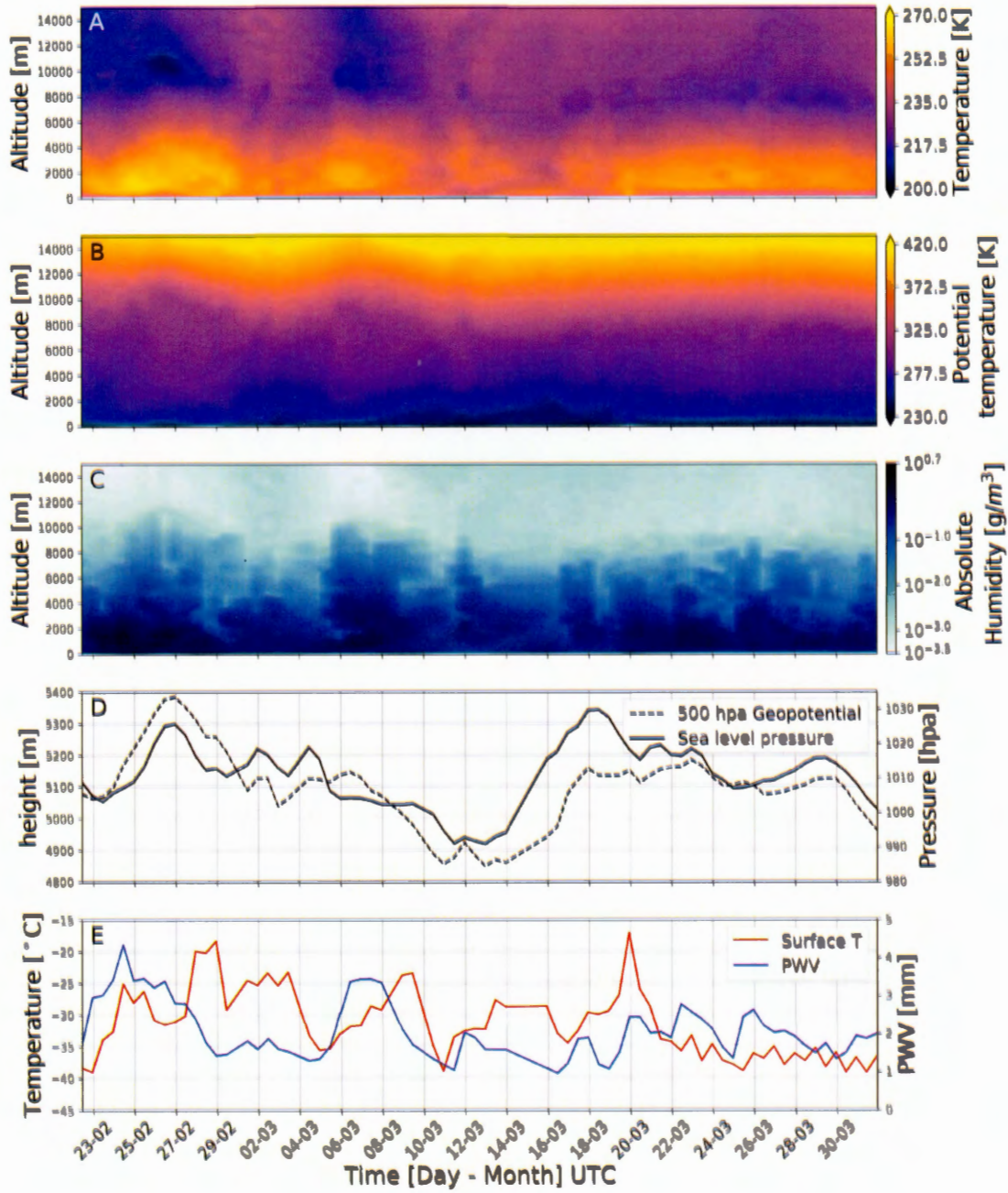


FIGURE 1.6: Time series of the weather vertical profiles and surface conditions obtain from radiosonde datasets at Eureka, Nu between February 22 and March 03, 2016.

a) temperature. b) potential temperature profile. c) absolute humidity. d) sea-level pressure, 500 hPa geopotential height. e) surface temperature and WV total column.

1.4 Radiometric Validation

In this section, radiometric resolution and accuracy of the FIRR are validated against E-AERI measurements. The radiances are further compared to theoretical calculations using a detailed radiative transfer model (RTM). The RTM parameters are described below. Then, radiative closure experiment is performed for a more thorough validation. In turn, we verify that the RTM properly reproduces the spectrally resolved radiance measured by the E-AERI in CS conditions. Checking RTM against measurements provide confidence on its application for extrapolating our results.

1.4.1 Radiative Transfert Simulation

For each radiosonde releases, atmospheric downwelling radiance was computed up to an altitude of 28 km. The simulations have been performed with the version 5.4.5 of MODTRAN (Berk *et al.*, 2005), using the HITRAN 2013 spectral line parameters database (Rothman *et al.*, 2013) and the water vapour continuum CDK 2.5.2 (Clough *et al.*, 2005). The spectral resolution was set to 0.1(cm⁻¹). Multiple scattering of haze and cloud particles was accounted for through the discrete ordinates method (DISORT) (Stamnes *et al.*, 1988) using an eight streams approximation.

The Temperature and RH are interpolated from the corrected 20 m resolution radiosonde dataset. The vertical profiles of CO₂ were obtained from the Total Carbon Column Observing Network (TCCON) a priori profiles (Wunch *et al.*, 2011). The profiles of methane and nitrous oxide are from the sub-Arctic winter case of (Paton, 1948). The ozone profile is interpolated from the ozone sonde release sparsely throughout the CANDAC sunrise campaign. When ozone sondes were available over 5 consecutive days in the vicinity of the launch, the sub-Arctic

standard profile from (Paton, 1948) was used instead.

The atmospheric vertical resolution used in calculations decreases with height. From a 1m resolution for the first 20 m above the ground, increasing to 20m layers up to 1 km height, to 60 m between 1Km and 3 km, to 100 m up to 10 km and finally 500 m to the top up to 28 km. Since the inversion layer near the surface often strong in the Arctic, the high resolution in the low levels is essential, as shown by (Mlynczak *et al.*, 2016), to properly resolve the highly absorptive water vapour rotation bands across the FIR spectrum as well as the ($15\mu\text{m}$) CO_2 band. A warm path inside the instrument has also been used to take into account the warmer air located in the FIR or E-AERI enclosure e.g.(Mlynczak *et al.*, 2016). This correction results in a better representation of the bands when the atmosphere as an extremely low transmissivity.

Due to the topographic reality around the EWS and the high stability of the boundary layer during Arctic winter, the exhaust of the electrical generator, located only 75 m away from ØPAL, tend to accumulate near the surface. The use of a standard CO_2 profile in the RTM results in a high residual for the FIR channels covering parts of the highly absorptive CO_2 bands. To perform a good radiative closure, the amount of CO_2 was doubled in the first 25 m and then linearly interpolated from 25 m to match the standard profile at 200 m. We acknowledge that during windy events, when the surface temperature inversion is dynamically broken, the correction could overestimate the amount of CO_2 in the lower levels.

The aerosol optical parameter has been set at a concentration corresponding to a rural visual extinction range of 24 km in the boundary layer. All simulations are performed without clouds, independently of the true atmospheric conditions at the time.

Those simulation will serve two purposes. First to perform an intercomparison

between simulated radiance and FIRR and E-AERI measurements during CS condition. Second, to obtain a CRF estimate by subtracting the clear sky simulated radiance to the corresponding clouds observation (See section 1.6).

1.4.2 Radiative Closure Experiment

A radiative closure experiment was done, by comparing the RTM simulated radiance with the measurements from the FIRR and the E-AERI. Comparing simulations to measurements is a way to validate both, the RTM ability to resolve clear sky downwelling radiance and the instruments radiometric resolution.

Since the simulated spectra are at higher resolution than the E-AERI, to enable their intercomparison, it is convolved with an Hanning window of a 0.5cm^{-1} half width (e.g. (Mast *et al.*, 2017)). The E-AERI and the simulated spectrum are then interpolated to a common wavenumbers grid of 0.1cm^{-1} . Both spectra are then smoothed to improve the clarity of the plot. To compare over the same bands ranges, the FIRR measurements to the spectrally resolved E-AERI observations and RTM simulations, a synthetic dataset of FIRR radiances is created for each filter, by convolving the E-AERI/RTM measured spectrum with the normalized spectral transmittances of the FIRR filters from :

$$I_\lambda = \sum_{w_{min}}^{w_{max}} I_w^s * \frac{T_w^\lambda}{T_{max}^\lambda} \quad (1.18)$$

where I_λ is the FIRR radiances for the channel λ , I_w^s is the spectrally resolve radiance from the E-AERI or MODTRAN at the wavelength w and T_w^λ is the FIRR filter transmittance in function of w .

E-AERI and MOTRAN integrated spectra over each filter range can then be used as a proxy of FIRR data. All FIRR and E-AERI observations were average over

1h periods, beginning at the time of the release of the sounding. The simulation for the 28/02/2016 2300UTC sounding was selected as a reference case since the sky was very clear. The Backscatter profile of the lidar never exceed $10^{-7} [msr^{-1}]$ after 23h. The atmospheric profile show 2 temperature inversions, one near the ground and another one below 2000 m. Since much of the radiance measured by the FIR channels, come from the lower levels of the atmosphere, this profile was selected to test the ability of the RTM to resolve complex thermal structures near the surface.

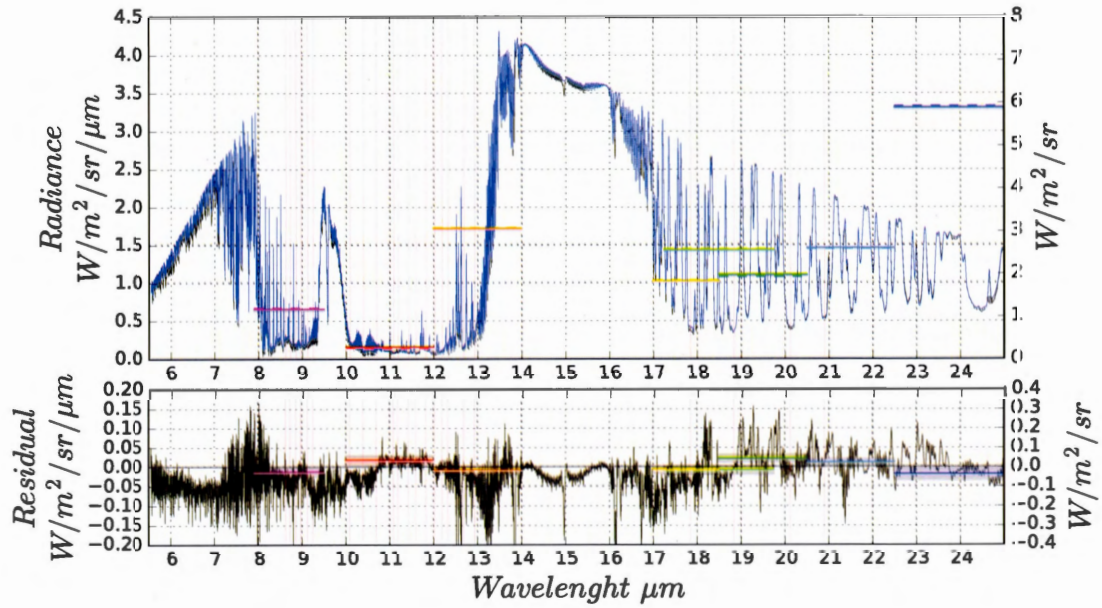


FIGURE 1.7: Clear sky simulated and observed downwelling radiance.

Top : Associated with the left Y axis, E-AERI (MODTRAN) in blue(black) measured(simulated) spectrally resolved downwelling radiance during a clear sky release of a radiosonde on February 28, 2016.

Associated with the right Y axis, In colour the FIRR(MODTRAN) in full line(dash line) measured(simulated) radiances for each band.

Bottom : Corresponding residual between the E-AERI - MODTRAN (black line) and FIRR - MODTRAN (colours), micro-windows (thin red lines) are also indicated.

TABLE 1.1: Radiative closure results.

Numerical RU values associated with the fig : 1.7. The FIRR measurements and their associated residuals with respect to MODTRAN.

Filters	7.9-9.5	10-12	12-14	17.25-19.75	17-18.5	18.5-20.5	20.5-22.5	22.5-27.5	30-50
RU	1.14	0.25	3.02	2.52	1.79	1.95	2.58	5.86	7.33
Residual	-0.03	0.03	-0.02	-0.02	-0.02	0.04	0.02	-0.04	0.05

As seen on fig : 1.7 and fig : 1.1 radiative closure is achieved to a good degree comparable to the FIRR laboratory radiometric resolution of $0.02 [W/m^2/sr]$ here after call Radiance Unit [RU]. Micro-windows in the FIR are properly resolved by the RTM but show a negative residual in the TIR. As stated before the aerosols visibility in the boundary layer was set to 24 km. An atmosphere without any aerosol (not shown) leads to a positive residual in the TIR micro-window. This suggests that an aerosol visibility lower than 24 km could yield a better radiative closure, but such experiment was out of the scope of this study. The filter with the higher residual is the one encompassing strong WV bands in the FIR. This could be due to uncertainties in the atmospheric profile very close to the instrument, or could also be associated to line parameters uncertainty in the HITRAN database. H_2O Line parameters show higher uncertainties in the FIR than in the TIR (Mast *et al.*, 2017). The WV continuum and line parameter are subject to constant improvement since the Radiative Heating in Underexplored Bands Campaign (Turner et Mlawer, 2010). But multiple spectrally resolved measurements in a very dry atmosphere are still required to further constrain those parameters (Mast *et al.*, 2017).

1.4.3 Radiometric Resolution

The overall radiometric accuracy of the FIRR and bias have been assessed throughout the campaign. Fig :1.8 shows the residual between the FIRR and the E-AERI/MODTRAN. They are shown for each of the FIRR filters. For the FIRR - MODTRAN each dots represent an average of the FIRR measurements during the 45-minute periods following the release of a sounding, then subtracted by the corresponding RTM simulated radiances to show differences. All simulations are included even those associated to a sounding released in presence of clouds. However, it is not representative of the true radiative bias. For the FIRR - E-AERI data, each dot represents an average taken over 1h for clear sky and cloud observation. To avoid as much as possible influence from the difference in temporal resolution between each instrument, only the timewise homogeneous scenes were selected. The standard deviation of the FIRR for the period needed to be under 1 RU to avoid selecting heavily fluctuating radiance values. This assures us that the scene was stable enough for the intercomparison with the E-AERI. Moreover a minimum of 10 FIRR and 7 E-AERI measurements per hour have been required for validation. This is to ensure that both instruments covered much of the 1h period.

The shaded areas, highlights periods same sequences of particular interest at the time of the FIRR measurement. The darkest one corresponds to AHS (ABB,HBB,Sky) sequences that first look at the ABB during the calibration. The lighter shade is associated to the HAS sequences looking first at the HBB . As one can see, in the first case the bias between the E-AERI and the FIRR range from -0.05 to -0.15 [RU] as for the second case, the bias is lower, ranging from 0.04 to - 0.07 [RU].

Such behaviour could be explained by two processes. First the rapid transition between the HBB and the cold SV positions could lead to the filter emissivity

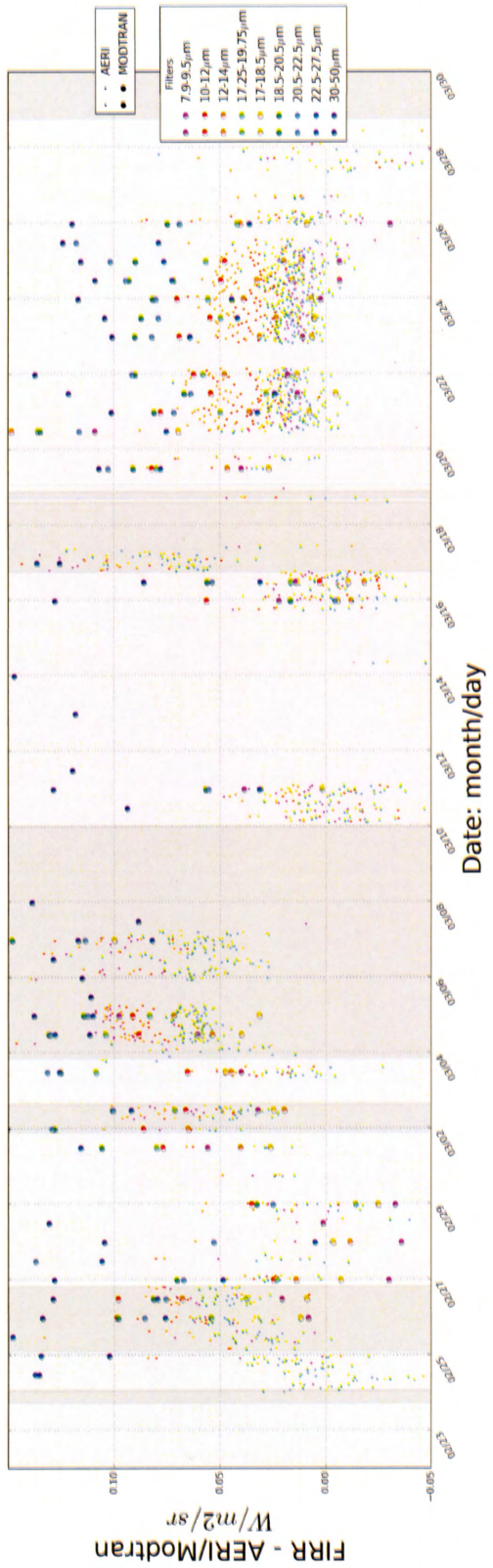


FIGURE 1.8: Residual between the FIRR and the E-AERI and between the FIRR and MODTRAN.

Light shade : Measurement made during an HAS sequence.

Dark shade : Measurement made during an AHS sequence.

itself is contributing to the measured radiance by the bolometer and not being properly taken into account in the calibration.. This effect has not been observed in the laboratory (Libois *et al.*, 2016b) since the BT of the ABB and the HBB were much closer to the SV position. This effect seems to affect the (7.9 - 9.5 μ m) filters more than the others, with a bias of 0.02 [RU] for the HAS and 0.1[RU] for the AHS.

The second process is attributed to the instrument configuration. Since the SSM barrel only rotate one way, during the AHS, the opening of the barrel does not pass by the zenith opening. Air is trapped in the OMD for a longer period. This results in a larger temperature build up inside the OMD. Higher amplitude of temperature variations in the optical path could affect the calibration process. The hypothesis was tested by monitoring the interior of the instrument using suspended naked thermocouples, looking at variations of the internal sensible heat flux of the OMD. The results (not shown) showed a stronger variation of the sensible heat flux when using the AHS sequence. The high bias is then explained by a stronger amplitude of the background signal during AHS sequences. This highlights the fact that the quality of FIR measurements is strongly affected by the thermal stability of the enclosure and the optical unit. An open configuration results in a strong temperature gradient through the OMD, like the case of Eureka. Part of the OMD was inside the lab at a temperature around 15 °C, and the other part was outside at temperature below –30 °C. This situation should be avoided in the future.

There are other sources of error observed throughout the campaign, even within the same type of data acquisition sequences. Multiple tests have been done to pinpoint the cause. Thermocouples placed inside the instrument enclosure showed that a variation of the sensible heat flux was present throughout the measurement periods, and that the magnitude of this heat flux was linked to pressure variation outside and inside the ØPAL building. Air was being sucked out through the

instrument optical path, causing internal temperature variation . The airflow was also an issue during the 2015 airborne campaign (Libois *et al.*, 2016a). But the airflow, being generated by the airplane speed, was stronger and steadier than the one experienced at OPAL. This problem could be solved by the implementation of a force steady airflow at a fixed temperature, this would not only reduce the noise induced by the sensible heat flux variation, but also help stabilize the filter temperature throughout the calibration process. Overall if we take into account the HAZ sequence only, the bias as well as the accuracy of the FIRR is slightly higher than the one experienced in the laboratory tests (Libois *et al.*, 2016b).

TABLE 1.2: Comparison between the FIRR and E-AERI/MODTRAN.

Clear sky FIRR measurements for all filters, residuals between the FIRR and the E-AERI/MODTRAN and their associated standard deviation for the period between 03/21 to 03/24 of March

Filter	FIRR	FIRR std	FIRR-AERI	FIRR-AERI std	FIRR-MODTRAN	FIRR-MODTRAN std
7.9-9.5	1.081	0.021	0.016	0.014	-0.017	0.009
10-12	0.284	0.024	0.028	0.047	-0.059	0.008
12-14	2.641	0.019	0.050	0.017	-0.020	0.011
17.25-19.75	2.661	0.020	0.007	0.012	-0.044	0.012
17-18.5	1.778	0.016	0.027	0.016	-0.004	0.005
18.5-20.5	2.047	0.019	0.024	0.009	-0.075	0.008
20.5-22.5	2.669	0.016	0.018	0.037	-0.072	0.009
22.5-27.5	5.742	0.032	Nan	Nan	0.038	0.022
30-50	6.641	0.020	Nan	Nan	0.034	0.011

Table 1.2 shows respectively the FIRR measurements in [RU], the residual with both the E-AERI and MODTRAN and their associated standard deviation (std), for the period of 03/21 to 03/24. To avoid any contribution from the cloud cover, we used only HAS sequences during a clear sky event. Bias with respect to E-AERI is at the maximum for the (12 - 14 μ m) filter and it is associated to a low

standard deviation, meaning that the bias is steady in time. This could be caused by either instrument. The ($10 - 12\mu m$) filter shows the largest bias in respect to the measured radiance and its standard deviation is also the highest. This might be attributed to the E-AERI being less accurate when measuring very low radiance (personal communication with Dr. Zen Marianni). Most importantly both instruments don't share the same optical path, the contribution from the air inside their enclosure could vary. E-AERI enclosure being sealed the temperature is more stable. The systematic warmer bias could be explained by the open configuration of the FIRR letting warm air flowing through the instrument. Concerning the bias with MODTRAN, to avoid averaging during cloud observation, only measurement when the BT of the $10 - 12\mu m$ was below 170K were used. A negative residual remains between the FIRR and MODTRAN with a low standard deviation value meaning that the simulation generally overestimate the downwelling radiance, with the exception of the two filters covering the longest wavelengths. This corroborates the idea that the aerosol optical dept used in the RTM is too high and that the WV might not be very well represented in the FIR. The low bias and standard deviation for the two filters affected by the CO_2 support the use of the modified profile in the simulation. The standard deviation of the FIRR measurements is always below 0.03[RU] with the exception of the ($22.5 - 27.5\mu m$) filters. Those results are similar to the one obtains by (Libois *et al.*, 2016b). Looking at a very cold atmosphere, radiances measured by the FIRR are often lower than the one used for in laboratory tests. Achieving the same radiometric resolution in those conditions prove that the detector has the ability to accurately measure the atmosphere downwelling radiance in a cold environment. Moreover the bias between MODTRAN and the FIRR being relatively low and robust, justifies the use of those simulations in the following sections.

1.5 Water Vapour

In this section the FIRR sensibility to the total PWV is investigated. A simple retrieval using only three FIR FIRR channels is described and evaluated.

1.5.1 PWV Observation

As shown in Fig : 1.9 During the March 25, from 0000 to 1200UTC the FIR channels BT increase steadily while the BT of the TIR filters remains more or less the same. During this time a humid layer of air is advected between 2000 m and 4000 m almost doubling the concentration of PWV. Both atmospheric sounding before and after the FIRR measurements are shown. The PWV increases from 1.35 [mm] to 2.43[mm] within 12h. The atmosphere then becomes less transparent in the FIR range. At the beginning of the day, in dryer atmospheric conditions, stronger radiative cooling from ground to space is happening despite the presence of thin clouds. The cloud event shows the strong link between WV profile and the FIR cooling.

The 3 filters in the range between $17\mu m$ and $22.5\mu m$ are the most affected by the increased PWV, while temperature is increased by $15^{\circ}C$. The $(17.25 - 19.75)\mu m$ and $(17 - 18.5)\mu m$ bands are not subject to the same BT increasing rate, leading to an inversion in their order around 0600UTC, implying that the first one experience a higher response to the change in PWV. As shown in (Libois *et al.*, 2016b) the transmittance of the atmosphere with respect to the PWV is not the same for each of the FIRR spectral bands. This can be seen in fig : 1.9 as their BT does not increase at the same rate. At low PWV the atmosphere is more transparent to the $(17.25 - 19.75)\mu m$ and $(18.5 - 20)\mu m$ channels than it is for the $(17 - 18.5)\mu m$. This is expressed as an increased in BT measure by the later ones. Those 3 filters partially overlap, making them less sensible to the smooth haze background. The

main differences are related to their responses to WV and CO_2 concentration. The $(17 - 18.5)\mu m$ is the only one sensible to the CO_2 , and its responses to the WV depend on the value of their spectral transmittance convoluted with H_2O .

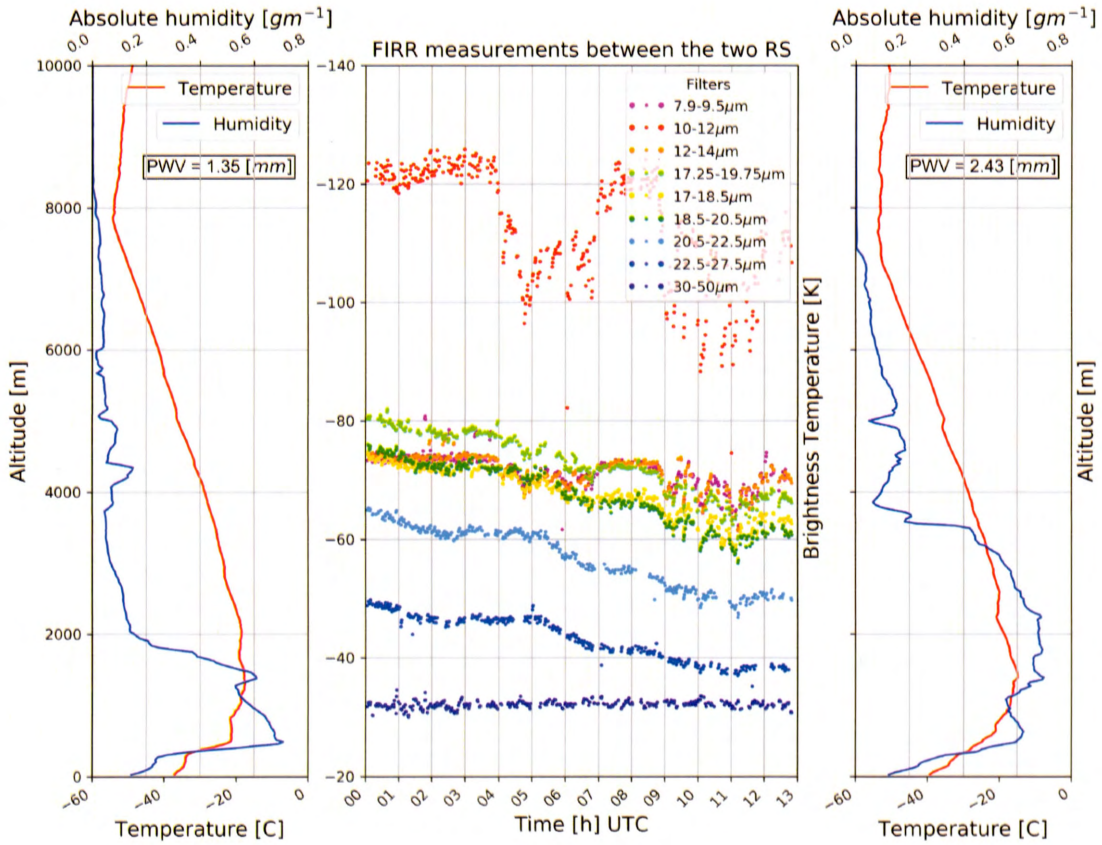


FIGURE 1.9: Comparison between CRL and radiosonde corrected atmospheric profile.

Left and Right : Radiosonde profiles of temperature and absolute humidity on March 25, 2016, at 0000 and 1200UTC respectively.

Middle : Time series of the FIRR measured brightness temperatures between the two soundings.

To investigate the relationship between those FIR BT and the total PWV, two

pairs of BT differences are defined and analyzed :

$$\Delta BT_1 = (17 - 18.5)\mu m - (17.25 - 19.75)\mu m \quad (1.19)$$

$$\Delta BT_2 = (17 - 18.5)\mu m - (18.5 - 20)\mu m \quad (1.20)$$

Shown in fig :1.10 is the comparison between the clear sky PWV and corresponding ΔBT . The FIR BT where averaged for 45 minutes after the release of a radiosonde to obtain both ΔBT values. The PWV was integrated from the corrected radiosonde RH profile.

One can see in fig : 1.10 that both ΔBT behave in the same way. Lower PWV leads to higher ΔBT , since the $(17 - 18.5)\mu m$ measure higher BT at very low amount of WV. This could be due to the band being dominated from the radiance emitted by the atmospheric CO_2 when the PWV concentration is low enough. Both ΔBT reach an asymptote at 7[mm] of PWV. At higher PWV ΔBT_1 tend to zero, both of the bands being dominated by the WV, while approaching saturation. ΔBT_2 Becomes negative around 2[mm] of PWV, suggesting that the $(18.5 - 20)\mu m$ band is the most responsive to the WV. It measures low BT in dry conditions, but increases very sharply with an increase of PWV. This is due to the filters transmittance functions overlapping with multiple WV rotational bands.

Also shown in fig : 1.10, are the values from E-AERI and MODTRAN, used as a proxy of the FIRR and for theoretical closure test of the experiment. Looking at the MODTRAN scatter plot, since the aerosol profile in RTM is uniform, the spread of inferred points around the curve can only be related to the change in the vertical distribution of the WV. The larger spread for the FIRR and the E-AERI are associated to a possible presence of haze and instrumental noise. MODTRAN

shows only a small bias compared to the FIR/E-AERI both ΔBT being higher for the same PWV. This is in accordance with the result shown in tab : 1.2, where the lowest warm bias of MODTRAN is found in the $(17 - 18.5)\mu m$ band. As previously discuss, this could be due to either a bad aerosol parameter or due to the fact that the RTM is not properly resolving the WV spectrum in the FIR.

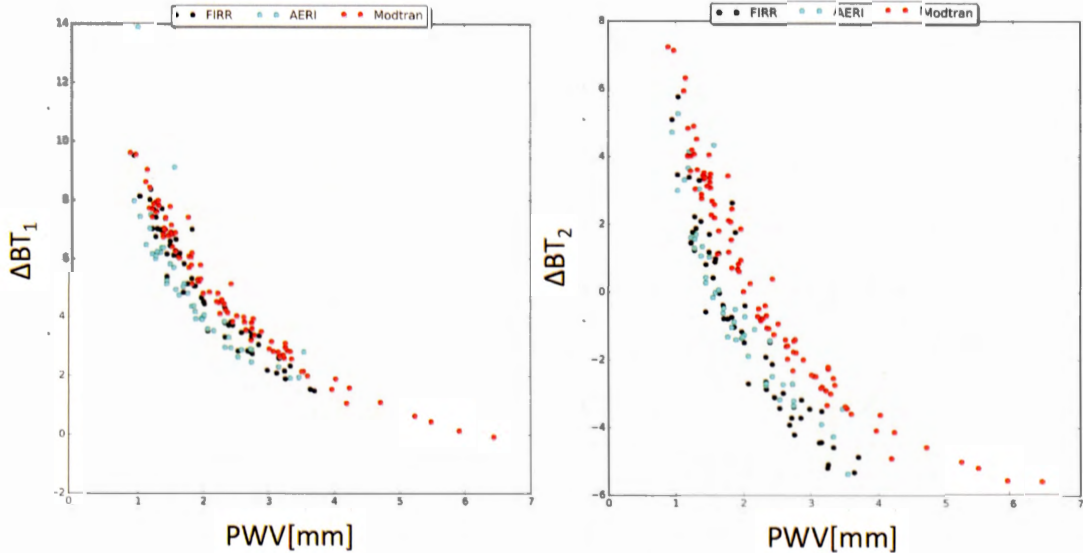


FIGURE 1.10: Variation of both ΔBT in respect to the water vapour total column PWV[mm] for clear sky events

1.5.2 PWV Retrieval

Algorithm Description

Using BT measured from the 3 filters discuss above a retrieval of the total PWV is implemented. To extract as much information as possible from those relationships, both ΔBT were used to retrieve PWV after applying a 2D polynomial fit in the

$\Delta BT - PWV$ 3D space as follows.

$$PWV = C_1 + C_2 \Delta BT_1 + C_3 \Delta BT_2 + C_4 \Delta BT_1 \Delta BT_2 + C_5 \Delta BT_1^2 + C_6 \Delta BT_2^2 \quad (1.21)$$

The coefficients have been retrieved for the winter (JFM) 2014 dataset from the E-AERI. The E-AERI was used as a proxy from the FIR, as describe in sections 1.4.2 to obtain the ΔBT then time corresponding corrected radiosondes were used to integrated WV over the column to obtain the PWV. Valid E-AERI measurements 45 minutes following the radiosonde launch were averaged together. Only profile with less than 4mm were kept to retrieve the coefficients. Clouds and arctic haze where filtered out of the dataset using a threshold of 170K for the $(10-11)\mu m$ BT. Only lower BT have been classified as clear sky, thus the same threshold needs to be applied prior to retrieve PWV. The resulting coefficients in Eq : 1.21 are shown in tab : 1.3.

TABLE 1.3: coefficient use in Eq : (1.21)

C_1	C_2	C_3	C_4	C_5	C_6
3.68881896	-0.79413762	0.20239227	-0.08143551	0.07631236	0.03808218

Results and Discussion

The retrieval was independently tested during the 2016 winter also using the E-AERI as a proxy to avoid any instrumental bias. Results are shown in fig :1.11 and detailed in tab :1.4 using the same statistical parameters use by (Weaver *et al.*, 2017).

The absolute and relative value of the standard deviation (std), standard error to

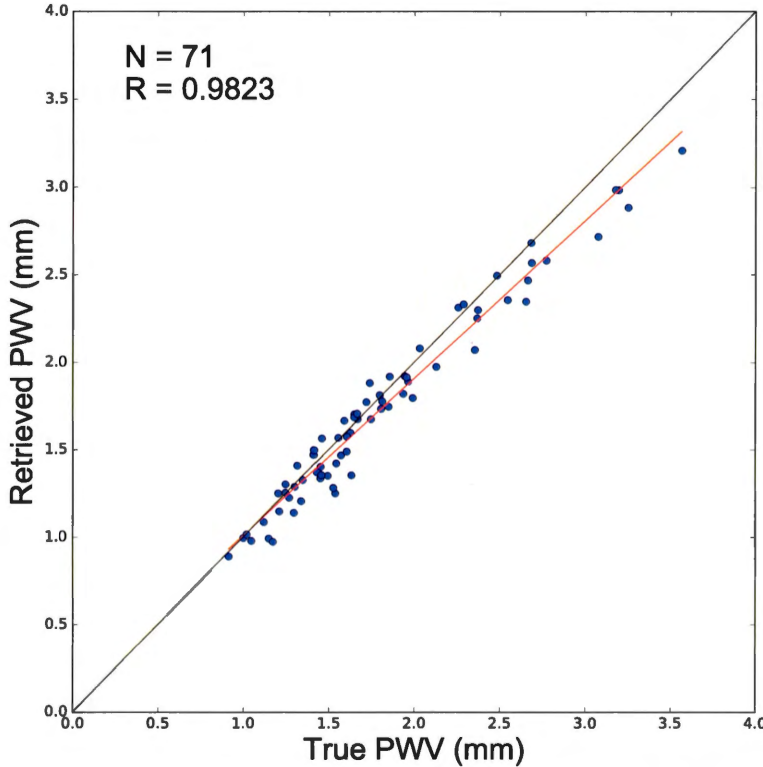


FIGURE 1.11: PWV from integrated radiosonde RH profile vs. the PWV retrieve using the FIRR

the mean (SEM) and root mean square difference (RMSD) are consistent with the one from the instruments evaluated in (Weaver *et al.*, 2017). The drift from the true PWV for the higher value is attributed to an uncertainty in the ΔBT_2 . It is suspected to be due to the presence of arctic haze either during the measurements period or from uncertainties in the retrieval of the coefficients. High winter PWV $>3\text{mm}$ contents are usually found at the end of March, when arctic haze or thin clouds are also more frequent. Therefore a larger data set should be used to retrieve the coefficients to reduce contamination by isolated events.

Since the FIRR retrieval of PWV is only being tested during winter, when PWV rarely exceeds 4[mm], direct comparison with other studies is difficult. Compared

TABLE 1.4: Results of inter-comparison of PWV measurements between the FIRR and the radiosonde.

Number of coincidence (N), correlation coefficients (R), slope of the best fit line (m), mean difference (Delta), standard deviation(std), standard error to the mean (SEM), root mean square difference(RMSD) in [mm] and [%]

N	R	m	Delta(mm)	std(mm)	SEM(mm)	RMSD(mm)	Delta%	Std%	SEM%	RMSD%
71	0.9823	0.9	0.08	0.12	0.02	0.14	4.14	6.42	0.76	7.64

with the results of (Weaver *et al.*, 2017), with a std of 0.12[mm] the FIRR performance exceeds the results from the MWR in the low concentration range. The FIRR results are similar to the Sun-photometer, with the chief advantage of not requiring sunlight to perform the measurement. The only instrument at ØPAL able to perform low concentration PWV retrieval during winter nights conditions is the E-AERI.

The retrieval method use with the E-AERI is the one describe by (Rowe *et al.*, 2008). It uses the radiosonde temperature and RH profile as a first guest, and through an iterative process rescale the WV until the simulated radiances match the observations. The FIRR retrieval, while being less accurate than the E-AERI, doesn't rely on any a priori information, suggesting a great potential of the FIR to retrieve the PWV. FIR retrieval of PWV is especially adapted to the polar night. Simple passive instruments such as GPS receivers can retrieve the PWV with an 0.7mm accuracy (Hagemann *et al.*, 2003). With the PWV values encounter in the polar regions, this represents a relatively high uncertainty. While only working at very low PWV, FIR radiometers could be used to fill the gap when other instruments lack sensitivity.

Other more precise passive remote sensing instruments such as the HAMSTRAD-

Tropo (Ricaud *et al.*, 2010) are measuring BT in the microwave spectrum. Using optimal effective method (OEM) (Rodgers, 2000), they use multiple narrow channels near the O_2 51-59 GHz line to first retrieve temperature profiles and spectral information in the 169-196 GHz range to retrieve WV profiles. The addition of FIR domain to the microwave range provides complimentary and independent information to improve this type of retrieval. The results presented in this study aim to be exploratory, as a sensitivity test rather than a fully operational algorithm. It deserves to be improved, first by using a more extensive data set over several winters to refine the coefficients and to improve the cloud screening. Future work would also involve testing more elaborate retrieval technique, such as applying the OEM methodology with all of the FIR filters and testing the addition of FIR bands to widely used microwave PWV approach.

1.6 Ice Cloud and Arctic Haze

In this section the FIRR sensitivity to cloud cover is investigated. Four cases of ice clouds and arctic haze are analyzed individually with respect to the full suite of instrument available at ØPAL. CRF signatures are inter-compared against cloud microphysical properties obtained from the CRL and the MMCR instruments. Based on those results a TIC sensitivity test using parameters developed from the FIRR observations is implemented. Based on a preliminary qualitative interpretation of the CRL and MMCR measurements, various events are classified in 5 categories, and the ability of the FIRR to retrieve them is evaluated.

Fig :1.12 shows a full day of FIRR/E-AERI and CRL observations at ØPAL. It is selected purposely for a case with a high cloud cover variability. Overall the FIRR BT show strong variation throughout the day having a notable response to cloud height and optical thickness. At 0900UTC the low depolarization ratio at

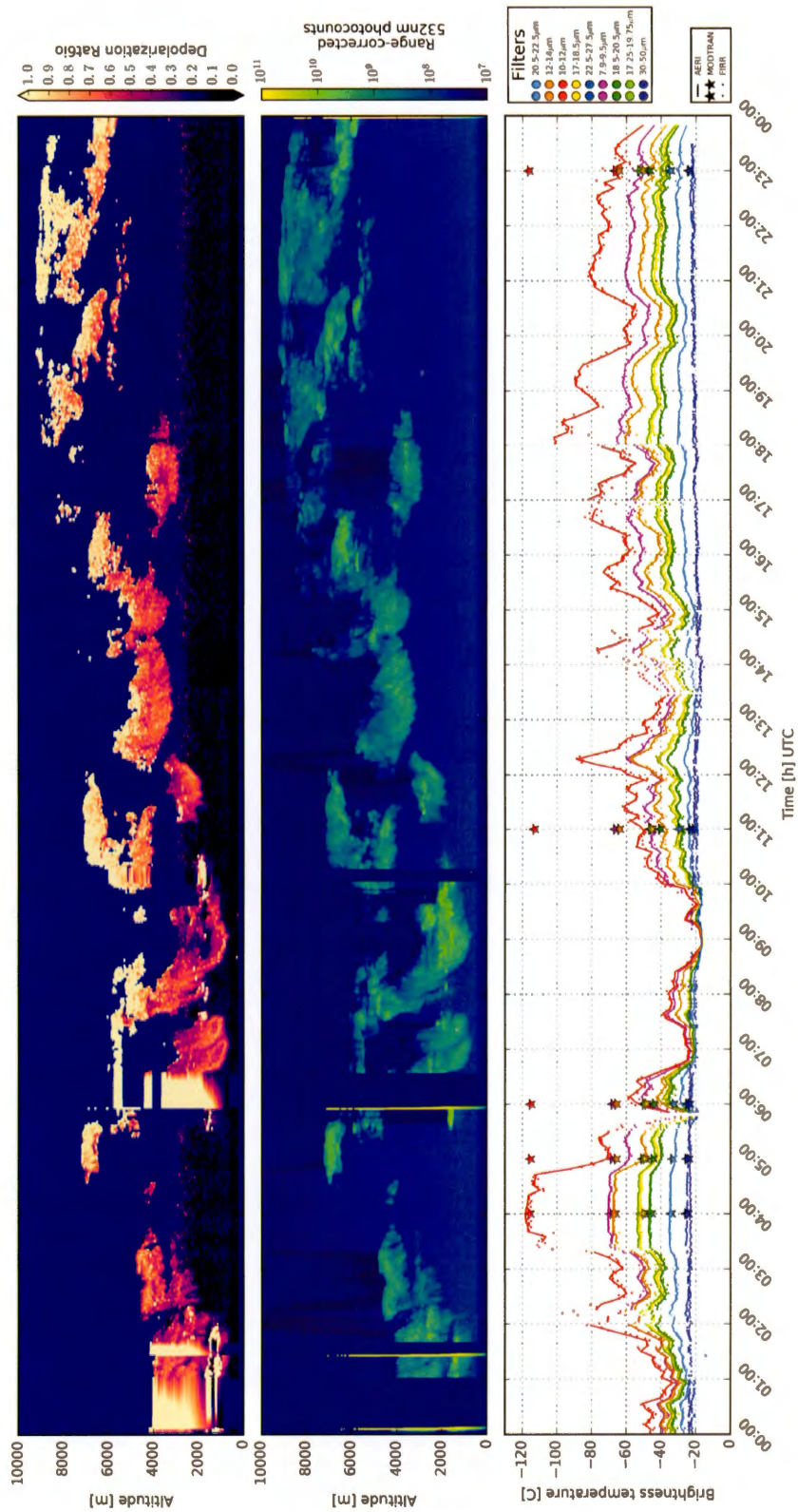


FIGURE 1.12: 24h Time series of cloud observations above ØPAL on February 24, 2016.

Top : CRL linear depolarization ratio.

Middle : CRL 532[nm] range-corrected photo-counts.

Bottom : FIRR/E-AERI/MODTRAN brightness temperature for each of the FIRR filters.

2000m mean that liquid droplets are present in the cloud. At the same time, all FIRR channels became saturated due to their high sensitivity to liquid droplets emissivity. The BT difference between each filter varies largely, since cloud emissivity is strongly dependant on wavelength and optical properties of the clouds (Yang, 2003). While the $30 - 50\mu m$ is only sensible to the lowest levels of the atmosphere, the $22 - 27\mu m$ is able to partially reach a cloud layer if it is low enough altitude. Higher BT observed at the end of the day is influenced by the strengthening temperature inversion, while the cloud temperature being higher than the surface temperature. During the brief period of clear sky, centred at 0400UTC, the RTM simulations from an interpolated sounding matches well the FIRR/E-AERI measurements, as verification.

1.6.1 TIC Observations

To assess the response of the FIRR to the cloud optical properties, four different cases were qualitatively analyses with respect to the parameters measured by the MMCR, the CRL and the FIRR/E-AERI suite of instruments. For each case, the cloud radiative forcing is obtained by subtracting the RTM simulation to the radiances of a cloud scene measurement. Those simulations have been performed with the same parameters describe in sections 1.4.1. Clouds were classified in four types, the first three types use the same definition as the one described in (Grenier *et al.*, 2009) :

- TIC - 1 : Non-precipitating TIC. Compose of large amount of small crystal.
- TIC-2A : Precipitating TIC overlaid by a TIC-1. Large amount of ice crystal with a high D_{eff} . Those TIC are associated with stronger updrafts, the high crystal number concentration (N_i) still leads to the formation of large crystal since air parcel vertical movement keep a high RH_i at the top of the cloud.

- TIC-2B : Precipitating TIC, small amount of large crystal, usually optically very thin ($COD < 3$). The RH_i inside the cloud remain high due to the low Ni not being able to quench all excess WV.
- Arctic haze : layers of hydrated acidic aerosols.

TIC-1

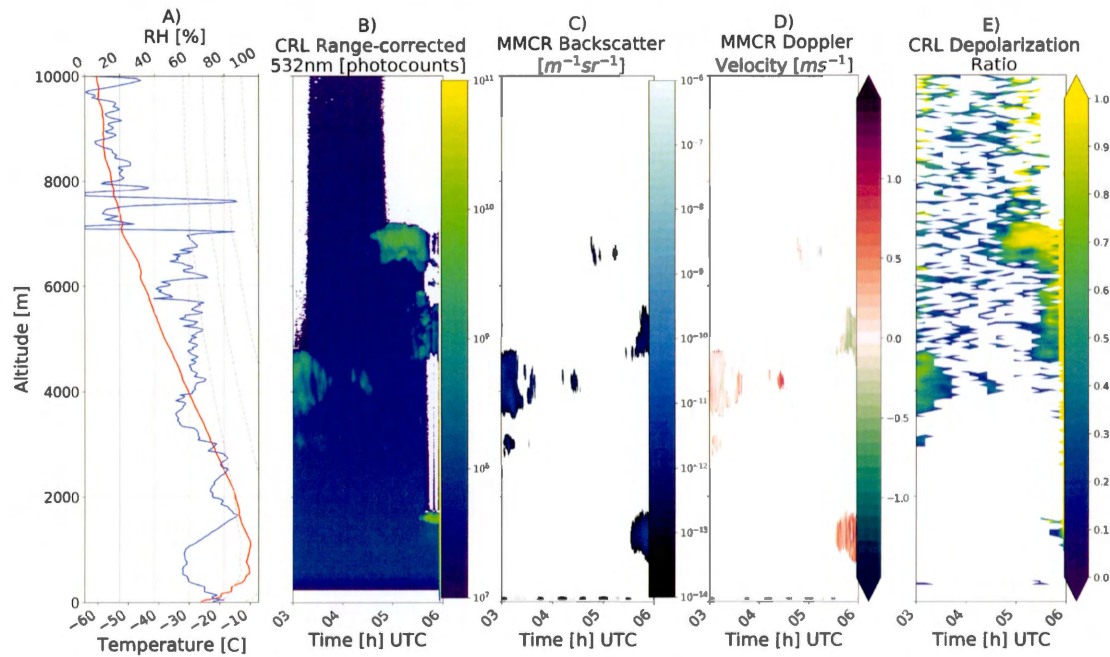


FIGURE 1.13: Observed case of TIC-1 above ØPAL on February 24, 2016.

- A : Interpolated temperature and relative humidity profile from the radiosonde.
- B : Time series of the CRL range-corrected photo-counts during the event.
- C : Corresponding MMCR backscatter, cloud mask set to $10^{-14}m^{-1}sr^{-1}$.
- D : MMCR Doppler velocity.
- E : CRL linear depolarization ratio.

The first case is one of the few TIC-1 cloud detected by the CRL lidar, but not by the MMCR, that was not hidden behind a lower layer of clouds. Fig : 1.13

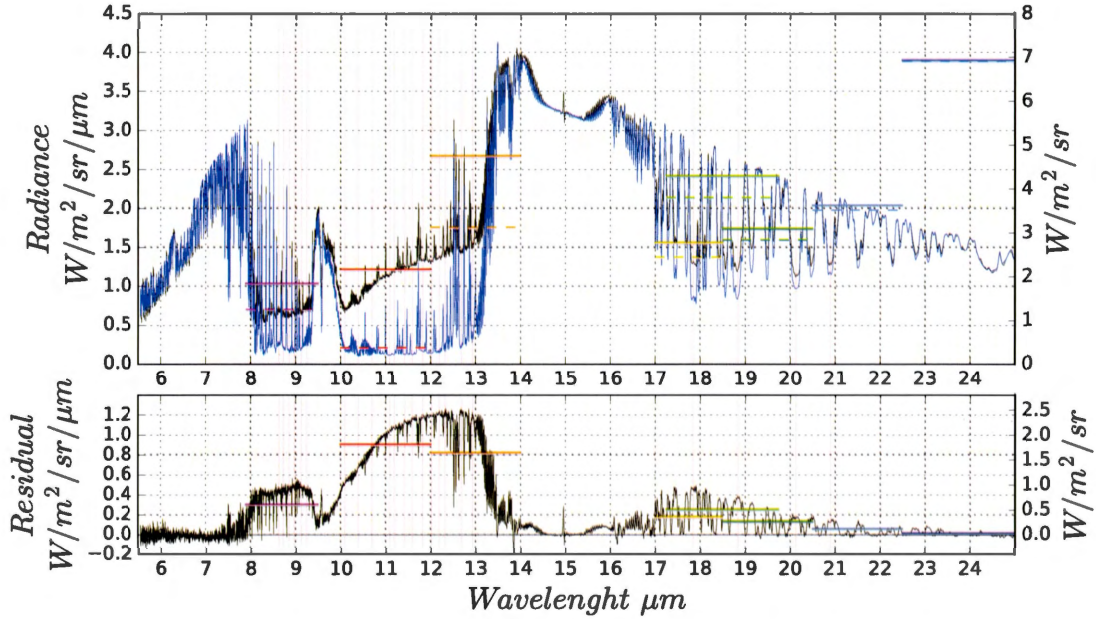


FIGURE 1.14: Cloud radiative forcing from a case of TIC-1.

Top : Associated with the left Y axis, E-AERI (black) and MODTRAN (blue) spectrally resolved downwelling radiance measurement during a case of TIC-1 shown in fig :1.13.

Associated with the right Y axis, the FIRR measured radiances (colours) for each band and MODTRAN (colours dash) simulated integrated radiances.

Bottom : Corresponding residual between the E-AERI - MODTRAN (black line) and FIRR - MODTRAN (colours) micro-windows (thin red lines) are also indicated.

TABLE 1.5: FIRR measured downwelling radiances [RU] for the case of fig : 1.14 and the corresponding residuals with MODTRAN for each filters

Filters	7.9-9.5	10-12	12-14	17.25-19.75	17-18.5	18.5-20.5	20.5-22.5	22.5-27.5	30-50
RU	1.82	2.14	4.72	4.27	2.75	3.08	3.61	6.91	7.02
Residual	0.59	1.79	1.62	0.49	0.34	0.26	0.11	0.02	0.11
Percentage	32.4	83.6	34.3	11.5	12.4	8.44	3.05	0.29	1.57

shows a cloud at 0500UTC, the cloud top is at a height of 7000 m and has a 400 m vertical extension, the mean temperature is around -50°C . The CRF in the AW($10 - 11\mu\text{m}$) (see fig : 1.14) is strong (1.79 RU). The high photo-counts from the CRL, and the attenuated signal above it, suggest a COD in the higher range for such a geometrically high and thin ice cloud. But since the MMCR is not able to detect it, the cloud is likely composed of large amount of small crystal (Bourdages *et al.*, 2009). As shown on 1.14, the CRF is stronger in the TIR channels of the FIRR and weaker in the FIR channels. Following the theoretical work of (Baran, 2009) and (Palchetti *et al.*, 2016a), it suggests that the cloud emissivity is higher in the TIR for a TIC with a low D_{eff} . We should consider that the radiosonde profile was interpolated. Since at those temperatures small fluctuation of absolute humidity lead to strong change in RH, the profile might not be representative of the true state of the atmosphere.

TIC-2

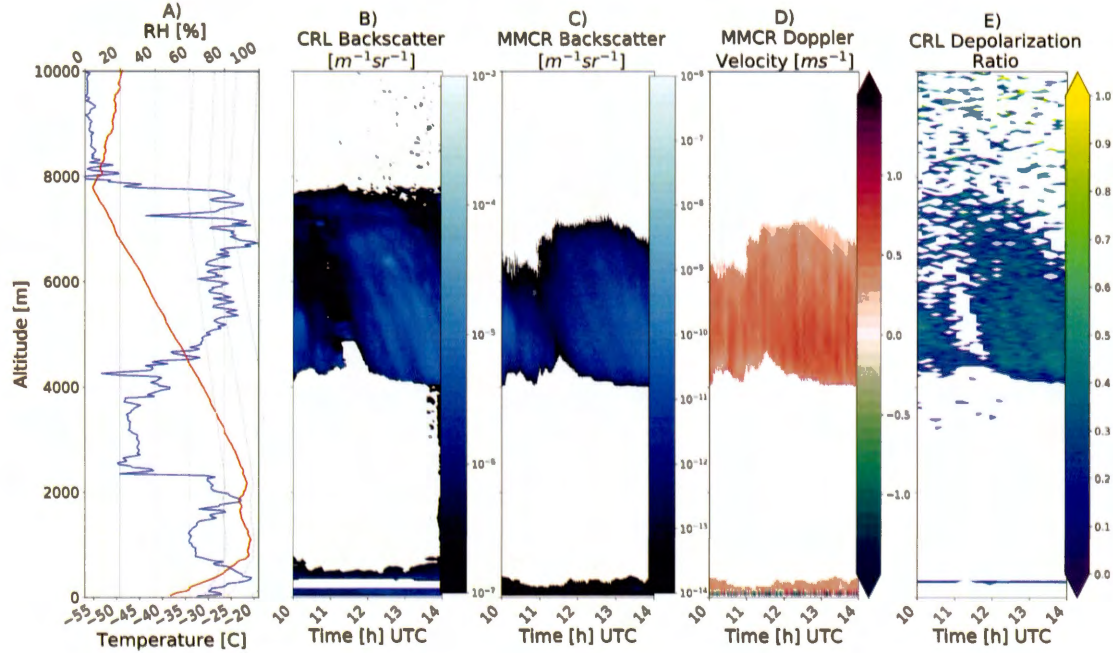


FIGURE 1.15: Observed case of TIC-2b above ØPAL on March 27, 2016.

- A : Interpolated temperature and relative humidity profile from the radiosonde.
- B : Time series of the CRL backscatter during the event.
- C : Corresponding MMCR backscatter, cloud mask set to $10^{-14} m^{-1} sr^{-1}$.
- D : MMCR Doppler velocity.
- E : CRL linear depolarization ratio.

TABLE 1.6: FIR measured downwelling radiances [RU] for the case of TIC-2B shown in fig : 1.16 and the corresponding residual with MODTRAN for each filter.

Filters	7.9-9.5	10-12	12-14	17.25-19.75	17-18.5	18.5-20.5	20.5-22.5	22.5-27.5	30-50
RU	1.09	0.62	2.77	2.63	1.77	1.96	2.54	5.55	6.59
Residual	0.10	0.42	0.31	0.19	0.11	0.13	0.09	0.04	0.16
Percentage	9.17	67.7	11.2	7.22	6.21	6.63	3.54	0.72	2.43

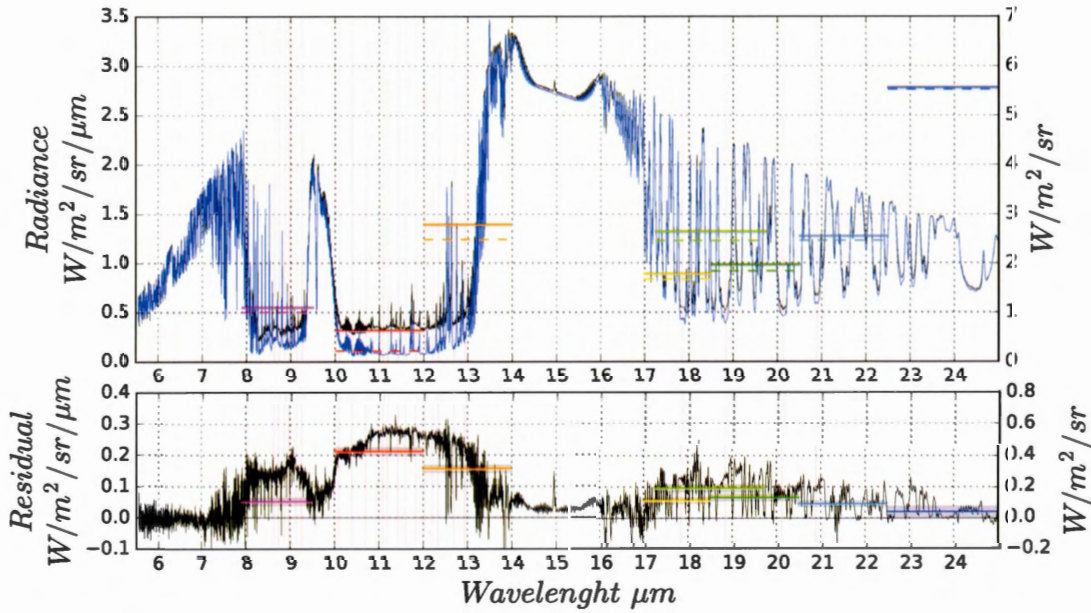


FIGURE 1.16: Cloud radiative forcing from a case of TIC-2B.

Similar to fig : 1.14 but for a case of TIC-2B shown in fig :1.15.

Fig : 1.15 show a case of a very optically thin TIC-2 clouds. The cloud top is located at 7700 m with a temperature of -55°C , it extends over 4500 m with an average temperature around -45°C . The β_l is low and the CRF in the AW($10 - 11\mu\text{m}$), shown in fig 1.16, is lower than in the previous case. This suggests a lower optical depth than the previous case for a geometrically much thicker cloud. Since the MMCR detect the cloud over its whole height, the IC are considered to be larger. The Doppler speed, with an average of $0.4 \text{ [ms}^{-1}]$ also suggest large crystals ($D_{eff} > 100\mu\text{m}$) (Matrosov *et al.*, 2002). In fig : 1.15 The CRF in the TIR and the FIR are nearly proportional and follow the expected emissivity curve of a grey body. A nearly constant emissivity value in the FIR and TIR wavelength range is representative of a cloud composed of larger crystal (Baran, 2007) (Palchetti *et al.*, 2016a).

Fig : 1.17 show the observed atmospheric profile and Fig : 1.18 the CRF ob served

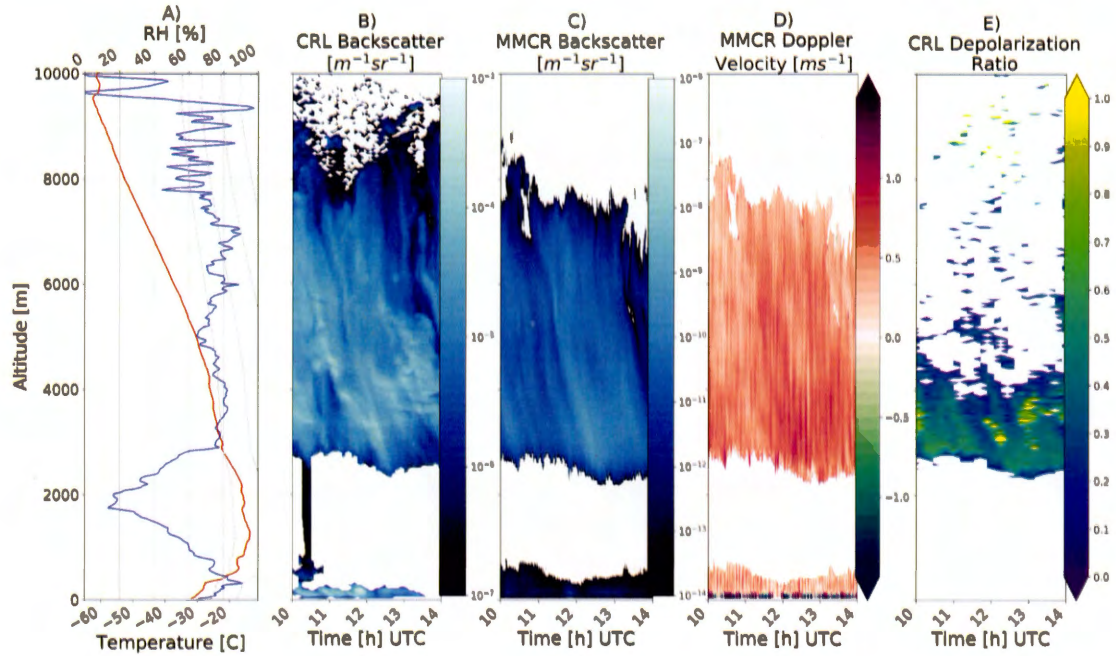


FIGURE 1.17: Observed case of TIC-2A above ØPAL on March 6, 2016.

Similar to fig :1.15

TABLE 1.7: FIR measured downwelling radiances [RU] for the case of TIC-2A shown in fig : 1.18 and the corresponding residuals with MODTRAN for each filter.

Filters	7.9-9.5	10-12	12-14	17.25-19.75	17-18.5	18.5-20.5	20.5-22.5	22.5-27.5	30-50
RU	3.03	3.54	5.34	4.55	2.91	3.19	3.59	6.72	6.79
Residual	1.94	3.28	2.52	1.45	0.87	0.86	0.60	0.46	0.12
Percentage	64.0	92.6	47.2	31.9	29.9	27.0	16.7	6.85	1.77

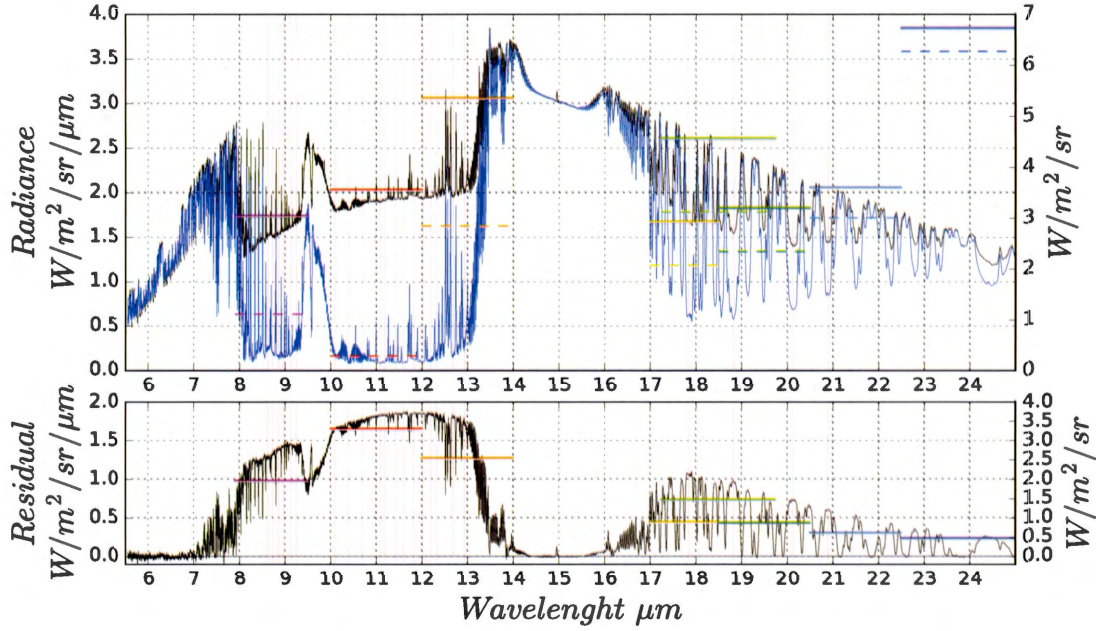


FIGURE 1.18: Cloud radiative forcing from a case of TIC-2A.

Similar to fig : 1.14 but for a case of TIC-2A shown in fig :1.17.

during the 6th of March. The CRL signal is lost around 9000 m due to attenuation by the larger cloud layer and the MMCR is not able to detect the top of the cloud. Following the RH profile, the cloud top is estimated to be located near 9200 m where the saturation over-ice reaches 160%. The cloud cover most of the troposphere with a vertical extension of 6500 m. The cloud tops temperature of -62°C is colder than the two previous cases. At such cold temperatures and RH_i the active region of the cloud must be dominated by homogeneous freezing (Krämer *et al.*, 2009), producing a large amount of small ice crystal. This is supported by the fact that the MMCR only start to detect the cloud at a height of 8000 m, where the Ice crystals have grown enough to be seen by the radar. Ice crystals size slowly grow during their descent quenching down the supersaturation over ice to near zero in the bottom half of the cloud, as opposed to the previous case where the amount of ice crystals was not sufficient to fully absorb the excess

WV. This suggests that the crystal number is higher than in the previous case. This conclusion is backed up by the high β_l value over the whole cloud since the lidar is more sensitive to the ice number concentration than to the particle size (Donovan et Van Lammeren, 2001). As shown in fig : 1.18 the CRF is high in all of the FIRR channels reaching 3.3 [RU] in the AW($10 - 11\mu m$). The cloud high β_l value and geometrical thickness explain its high radiative forcing. Moreover, even if the cloud top is much colder, the bottom of the cloud which accounts for much of the signal measure by the FIRR is -20K warmer than the previous cloud average temperature. Crystals at the bottom of the cloud have grown by deposition throughout sedimentation process and are estimated to reach a size around $200\mu m$ (Matrosov *et al.*, 2002). In those conditions the cloud forcing spectrum also follow a grey body curve as expected for large crystals.

Arctic Haze

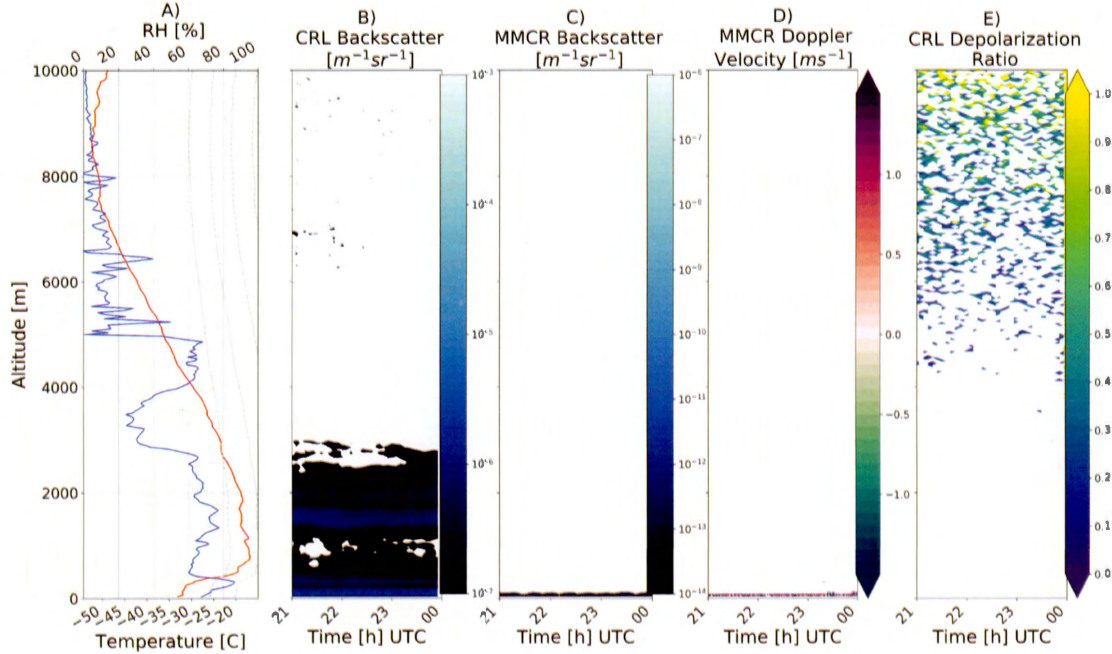


FIGURE 1.19: Observed case of arctic haze above ØPAL on March 22, 2016.
Similar to fig :1.15.

Fig : 1.19 show measurement made on March 22, when a case of strong arctic haze was observed. The β_l coefficient indicates the presence of a layer of haze just under 2000 m. The depolarization is low, and following the criteria from (Bourdages *et al.*, 2009) such layer is a characteristic of wet haze. Often encountered during spring this is a classic case of arctic haze produce by the deliquescence of sulfate aerosols (Sirois et Barrie, 1999). Fig : 1.20 show that the radiative forcing of the layer is very weak and the changes between the simulated spectrum from MODTRAN that from the E-AERI is barely perceptible. Still the residual is higher than the one shown in fig : 1.7, during the radiative closure experiment and likely detectable in the FIR. The $(20 - 22)\mu\text{m}$ seems to be the most sensitive to the presence of haze.

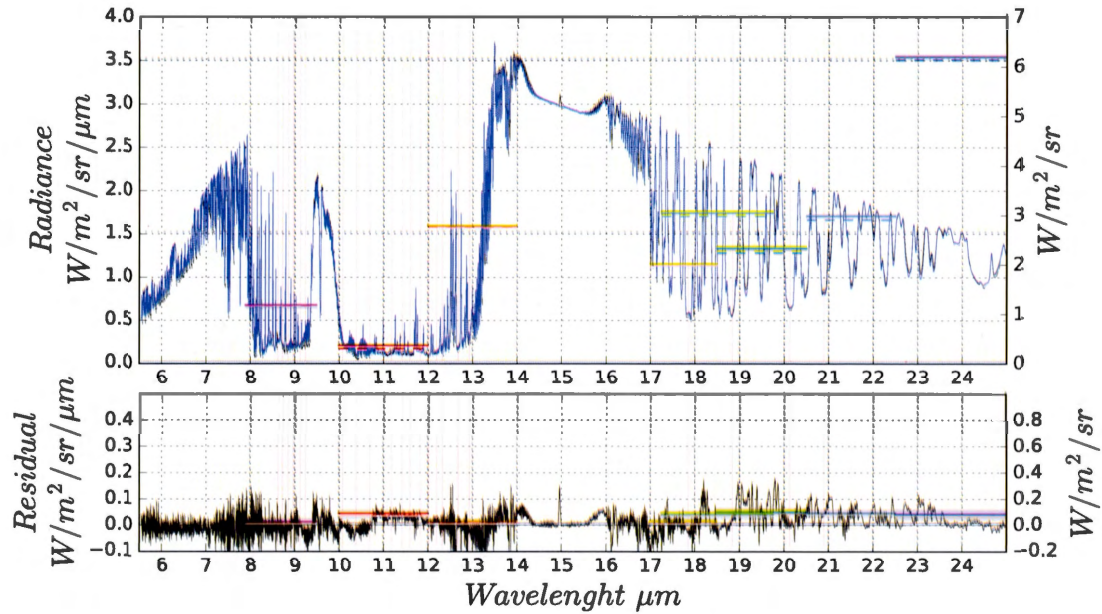


FIGURE 1.20: Cloud radiative forcing from a case of arctic haze.

Similar to fig : 1.14 but for a case of haze shown in fig :1.19

TABLE 1.8: FIRR measures downwelling radiances [RU] for the case of arctic haze shown in fig : 1.19 and the corresponding residual with MODTRAN for each filters

Filters	7.9-9.5	10-12	12-14	17.25-19.75	17-18.5	18.5-20.5	20.5-22.5	22.5-27.5	30-50
RU	1.14	0.32	2.73	3.02	1.96	2.31	2.96	6.17	6.71
Residual	0.01	0.07	0.01	0.07	0.01	0.09	0.08	0.07	0.10
Percentage	0.88	21.8	0.37	2.32	0.51	3.90	0.03	1.13	1.49

1.6.2 TIC Classification Algorithm

The CRF is defined as follows :

$$CRF = I_{cloud} - I_{clear} \quad (1.22)$$

where I_{cloud} is the downwelling radiance from a cloudy sky measurements and I_{clear} is the atmospheric downwelling radiance from a clear sky. Since in cold temperature the atmospheric layer between the radiometer and the cloud base is dry enough to have a good transmittivity, the CRF can be used as a rough estimate of its emissivity. We use the CRF as a classification system between TIC-1 and TIC-2.

Methodology

To test the sensitivity of the FIRR to the cloud D_{eff} a method based on the cloud BT residual have been applied. First clear sky BT are compute through MODTRAN (BT_{cs}) for all the FIRR filters.

$$BT_{cf}^{\lambda} = BT_{obs}^{\lambda} - BT_{cs}^{\lambda} \quad (1.23)$$

Then as shown in Eq : 1.23 the BT_{cs} are subtracted to the FIRR measurement (BT_{obs}) to obtain the BT CRF λBT_f for each spectral band λ .

Based on the jacobians from (Palchetti *et al.*, 2016a), since AW have no sensitivity to IC size variation and is mainly sensible to the optical thickness of the clouds each FIRR channels are normalized by the most transparent (10 – 12) μm bands

to obtain a β^λ parameter through :

$$\beta^\lambda = \frac{BT_{cf}^\lambda}{BT_{cf}^{(10-12)\mu m}} \quad (1.24)$$

For the $(12 - 14)\mu m$ filter, increasing the cloud D_{eff} lead to a lower cloud emissivity. As for the $(7.9 - 9.5)\mu m$ and the FIR filters the cloud emissivity increases with the D_{eff} . This is in agreement with the spectral shape of the residual in fig : 1.18 and fig : 1.14 where the slope between the radiance at $12\mu m$ and the radiance at $8\mu m$ and $20\mu m$ is steeper for the TIC-1 case. As shown by (Yang, 2003), the sensitivity to crystal size is maximal near $23\mu m$. From a ground perspective, the $(22 - 27)\mu m$ filter of the FIRR is too sensitive to the presence of WV in the lower level of the atmosphere and add noise to the cloud signal. Instead the $(17.25 - 22.5)\mu m$ channel has been selected.

Based on this knowledge two $\Delta\beta$ parameters are calculated from :

$$\Delta\beta_{TIR} = \beta_{cf}^{(12-14)\mu m} - \beta_{cf}^{(7.9-9.5)\mu m} \quad (1.25)$$

$$\Delta\beta_{FIR} = \beta_{cf}^{(12-14)\mu m} - \frac{(\beta_{cf}^{(17.25-19.75)\mu m} + \beta_{cf}^{(18.5-20.5)\mu m} + \beta_{cf}^{(20.5-22.5)\mu m})}{3} \quad (1.26)$$

To test our algorithm, the clouds during the campaign were classified based on the observation parameters of collocated instruments from ØPAL. We selected only the timewise homogeneous cloud scenes and those cases composed only of a single cloud layer with no ice crystal layer seen near the ground. All scenes have been classified between 5 types following specific criteria :

- Clear Sky : β_l under $10^{-8} [m^{-1}sr^{-1}]$ over the whole vertical profile.

- TIC-1 : Lack of falling streak, B_l above $10^{-6} [m^{-1}sr^{-1}]$ or high value of range corrected photo-counts from the CRL and low/no reflectivity from the MMCR. Average Doppler speed of less than 0.1 [m/s].
- TIC-2 : Presence of falling streaks in the cloud, detection from the CRL and the MMCR, average Doppler speed over 0.5 [m/s]
- Haze : Low detection by the CRL, B_l in the vicinity of $10^{-6} [m^{-1}sr^{-1}]$, with a corresponding low depolarization ratio.
- TIC-2 + Haze : Same criteria as the TIC-2 with an underlying layer of haze below it.

5 TIC - 1 case where identified using those criteria, all of those cases are above 6000 m and only one case was undetected by the MMCR while no clouds were detected below it. 9 cases of TIC-2 spanning from 8000 m to 500 m with varying geometric thickness spread throughout the campaign. 6 cases of haze, all happening during the last 10 days of March and contain within the first 3000 m of the atmosphere. The corresponding BT measure by the FIRR where averaged during each observations time span, with a duration varying between 10 and 60 minutes, corresponding respectively to 3 and 20 sequences of the FIRR observations.

Results and Discussion

Fig : 1.21 show a phase space with the two $\Delta\beta$ as its dimensions. As one can see all types of cases are regrouped into distinctive clusters, Considering the spread of each cluster it would be impossible to distinguish them using only one of the $\Delta\beta$, both the TIR and the FIR are needed. Since all cases of TIC-1 happened during similar atmospheric profile and near the same altitude, the spread in the TIC-1 cluster may be explained largely by the variation of the clouds ice crystal size.

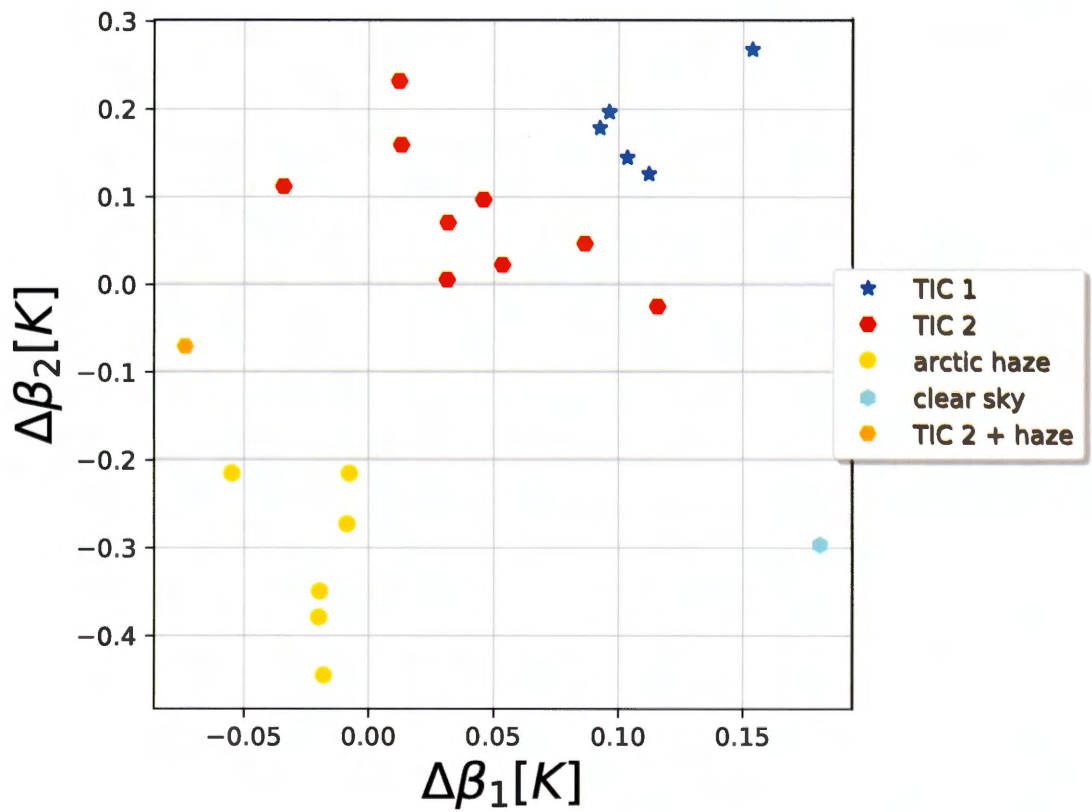


FIGURE 1.21: FIR TIC classification.

$\Delta\beta_{TIR}$ vs. $\Delta\beta_{FIR}$ for each selected cases

The fact that the only TIC-1 not detected by the MMCR, shown in 1.13, is the one with the highest $\Delta\beta$ in both the FIR and the TIR, supports this assumption, being probably the one with the smallest ice crystals average diameter. The TIC-2 cluster spread could also be explained by the ice crystal size variation, but some of the variation of the $\Delta\beta_{FIR}$ could be due to a change of the atmospheric transmittance below the cloud. There is a clear distinction between the clear sky case and the arctic haze cases, but a larger data set needs to be used to confirm this behaviour. Those results are very encouraging and clearly show the value of the FIR channels to better classified ice clouds by their effective diameter. This is in agreement with the result of (Blanchard *et al.*, 2017) and it supports the theoretical work of (Libois et Blanchet, 2017).

Improvement on this preliminary results could be made by taking the true emissivity of the cloud to calculate the $\Delta\beta$ parameters instead of the normalize radiative forcing of eq : 1.24. Due to its high sensitivity to WV, the $\Delta\beta_{FIR}$ is sensitive to the state of the atmosphere below the cloud. The atmosphere transmittance would need to be taken into account to retrieve the true emissivity of the cloud, since part of the cloud emitted radiance have been absorbed by the underlying layer of the atmosphere. This method would be similar to the split window describe in (Heidinger et Pavolonis, 2009) where the cloud emissivity is retrieved through an OEM.

1.7 Conclusion

The FIRR a broadband radiometer measuring downwelling radiance in 9 channels spanning from 8 to $50 \mu m$, was first designed as a prototype to test the technologies to be used on TICFIRE satellite mission. Additionally the FIRR instrument was aimed to be used as a ground-based instrument to probe the atmosphere

in the high Arctic, filling a gap in the observations of the water vapour at low concentrations, ubiquitous during the polar night and spring. For this study the FIRR was installed at Eureka, NU during the 2016 winter and spring. The first goal of this study was to assess the FIRR radiometric resolution while measuring a very cold atmosphere over an extended period to validate the technologies and the instrumental design. The second objective was to test the instrument sensitivity to the state of the atmosphere, especially the WV profiles and the optical properties of the TIC.

By comparing the FIRR radiance measurements with the E-AERI a collocated FTIR and simulated downwelling radiances, the radiometric resolution has been characterized during the whole campaign. Results show that the radiometric resolution of the FIRR depends on the stability of the thermal state of the instrument itself. When environmental conditions favour a stable state, the radiometric resolution matches the one measured in controlled laboratory conditions with value close to 0.02 [RU]. This is very satisfying considering that the measured BT was reaching very low values. Those results nevertheless, highlight the need to improve the actual instrumental design to ensure a constant thermal stability. The next FIRR generation is already being built and is planned to be installed at the supersite of Iqaluit in the Canadian Arctic during the fall of 2018. In the light of our results, the new OMD enclosure was designed to be thermally stabilised and to avoid any airflow through the instrument.

Using the RH profile from radiosonde release on the site. The response of the FIRR channels were analyzed with respect to the PWV content of the atmosphere. The FIRR showed a remarkable sensitivity to low amount of WV. Using 3 of the FIR bands of the FIRR a simple retrieval was developed and tested. Result shows that the FIRR is able to retrieve the PWV with accuracy and a resolution similar or exceeding other instruments located at Eureka. While only working at low PWV

value ($< 4\text{mm}$) the retrieval remains relatively simple and doesn't rely on any a priori information. This demonstrates the use of the FIR to monitor low amount of WV in cold regions. FIR radiometer could fill a gap left by other instruments that lose their accuracy at low PWV content or limited by the presence of sunlight. Future work would involve using FIR broadband measurements in a more advance retrieval technique.

Based on the results from theoretical work about ice clouds emissivity (Baran, 2009)(Palchetti *et al.*, 2016a). A TIC sensibility test based on their CRF signature was implemented. Using collocated active remote sensing instruments clouds observed during the campaign were classified based on their optical properties. The FIRR sensibility to those properties has been evaluated. Results show that when using the TIR in conjunction with the FIR bands, the FIRR is able to discriminate between cloud with small and large D_{eff} . This is, to our knowledge, the first time that broadband FIR radiometry is used to retrieve TIC properties from a ground perspective. Those results are the continuity of the work done in (Blanchard *et al.*, 2017) and support the theoretical work of (Libois et Blanchet, 2017). Future work would involve the implementation of a true retrieval of the TIC properties using all of the FIRR bands.

Overall the results from the 2016 Eureka campaign show that a broadband FIR radiometer is very effective to remotely monitor the water cycle in the polar region. It also highlights the importance of the FIR in the energy balance of the cold regions of the Earth.

CONCLUSION

Le FIRR, un radiomètre mesurant la radianc émise vers la Terre par l'atmosphère dans 9 bandes couvrant les longueurs incluses entre 8 et 50 μm , a d'abord été conçu comme un prototype afin de tester les technologies au coeur du projet satellitaire TICFIRE. Par la suite, le FIRR a été utilisé comme instrument au sol afin de combler les lacunes d'observations concernant le cycle de l'eau durant la nuit polaire. Le radiomètre a donc été installé à Eureka, NU pendant l'hiver 2016.

L'objectif premier de cette étude était de quantifier la précision et la résolution radiométrique de l'instrument sur une longue période en mesurant une atmosphère très froide, afin de valider la technologie utilisée ainsi que le design de l'instrument. Le deuxième objectif était de tester la sensibilité de l'instrument à l'état de l'atmosphère, aux propriétés optiques des nuages de glace optiquement mince ainsi qu'aux quantités intégrées de vapeur d'eau que l'on retrouve durant la nuit polaire.

En comparant les radiances mesurées par le FIRR avec celle d'un interféromètre, ainsi qu'avec ceux simulés par un modèle de transfert radiatif. La résolution radiométrique a été caractérisée durant l'ensemble de la période d'activité du FIRR à Eureka. Les résultats démontrent que la résolution du FIRR dépend fortement de la stabilité thermique de l'enceinte de l'instrument. Lorsque les conditions environnementales favorisent un état thermique stable, la résolution du FIRR est similaire à celle obtenue en laboratoire, soit $0.02 [W/m^2/sr^{-1}]$. Ceci est très satisfaisant considérant que les valeurs de température de brillance de l'atmosphère étaient moindres que celles mesurées en laboratoire. Ces résultats démontrent

aussi qu'un meilleur design instrumental est nécessaire afin de garantir la stabilité thermique de l'instrument.

Une nouvelle génération du FIRR a déjà été produite et sera installée à Iqaluit, Nu en septembre 2018. À la lumière des résultats de cette étude, le nouvel instrument a été conçu afin d'être beaucoup plus stable. L'OMD est stabilisé thermiquement et la circulation de l'air y est bloquée.

En utilisant le contenu intégré de vapeur obtenu à l'aide de radiosondages, la réponse du FIRR à différentes valeurs de vapeur d'eau précipitable (VP) a été analysée. Le FIRR démontre une grande sensibilité à la vapeur d'eau. En utilisant 3 bandes dans le IRL, une méthode d'inversion afin de mesurer la valeur de VP a été développée. Les résultats démontrent que le FIRR est capable de mesurer VP avec une résolution similaire à celle d'autres instruments utilisés dans les régions polaires. Malgré le fait que cette méthode est restreinte à de faibles quantités de vapeur d'eau ($< 4\text{mm}$), celle-ci ne requière aucun *a priori* et est très efficace dans des conditions où d'autres instruments perdent leurs sensibilités. Ceci prouve l'utilité du IRL afin de mesurer de faibles quantités de vapeur d'eau dans les régions froides de l'atmosphère. Un radiomètre mesurant le IRL pourrait couvrir la lacune laissée par d'autres instruments durant la nuit polaire.

Se basant sur les travaux théoriques de (Baran, 2009) et (Palchetti *et al.*, 2016a), un test de sensibilité a été développé à l'aide du forçage radiatif des nuages. En utilisant le radar et le lidar présents à Eureka, les nuages observés durant la campagne ont été classifiés en fonction de leurs propriétés optiques. La sensibilité du FIRR à ces propriétés a été analysée et sa capacité à classifier chaque type a été évaluée. Les résultats démontrent que lorsque le IRL est utilisé conjointement avec le IRT, le FIRR est capable de faire la distinction entre les TICs ayant un petit et un grand D_{eff} . Ceci représente à notre connaissance la première fois qu'un

radiomètre IRL à bandes larges est utilisé afin de classifier les TICs à partir du sol. Ces résultats confirment les hypothèses émises par (Blanchard *et al.*, 2017) et supporte les travaux théoriques de (Libois et Blanchet, 2017).

De manière générale, la campagne du FIRR à Eureka démontre qu'un radiomètre IRL est efficace afin d'observer le cycle de l'eau dans les régions polaires et confirme l'importance de l'infrarouge lointain dans le bilan énergétique des régions froides de la Terre.



BIBLIOGRAPHIE

- Abbatt, J. P., Benz, S., Czkzo, D. J., Kanji, Z., Lohmann, U. et Möhler, O. (2006). Solid ammonium sulfate aerosols as ice nuclei : A pathway for cirrus cloud formation. *Science*, 313(5794), 1770–1773.
<http://dx.doi.org/10.1126/science.1129726>. Récupéré de
<http://science.sciencemag.org/content/313/5794/1770>
- Abbatt, J. P., Richard Leaitch, W., Aliabadi, A. A., Bertram, A. K., Blanchet, J. P., Boivin-Rioux, A., Bozem, H., Burkart, J., Chang, R. Y., Charette, J., Chaubey, J. P., Christensen, R. J., Cirisan, A., Collins, D. B., Croft, B., Dionne, J., Evans, G. J., Fletcher, C. G., Gali, M., Ghahremaninezhad, R., Girard, E., Gong, W., Gosselin, M., Gourdal, M., Hanna, S. J., Hayashida, H., Herber, A. B., Hesaraki, S., Hoor, P., Huang, L., Hussherr, R., Irish, V. E., Keita, S. A., Kodros, J. K., Köllner, F., Kolonjari, F., Kunkel, D., Ladino, L. A., Law, K., Levasseur, M., Libois, Q., Liggio, J., Lizotte, M., MacDonald, K. M., Mahmood, R., Martin, R. V., Mason, R. H., Miller, L. A., Moravek, A., Mortenson, E., Mungall, E. L., Murphy, J. G., Namazi, M., Norman, A. L., O'Neill, N. T., Pierce, J. R., Russell, L. M., Schneider, J., Schulz, H., Sharma, S., Si, M., Staebler, R. M., Steiner, N. S., Thomas, J. L., Von Salzen, K., Wentzell, J. J., Willis, M. D., Wentworth, G. R., Xu, J. W. et Yakobi-Hancock, J. D. (2019). Overview paper : New insights into aerosol and climate in the Arctic. *Atmospheric Chemistry and Physics*, 19(4), 2527–2560. <http://dx.doi.org/10.5194/acp-19-2527-2019>
- Ansmann, A. et Müller, D. (2005). Lidar and Atmospheric Aerosol Particles. In *Lidar* 105–141. New York : Springer-Verlag
- Baran, A. J. (2007). The impact of cirrus microphysical and macrophysical properties on upwelling far-infrared spectra. *Quarterly Journal of the Royal Meteorological Society*, 133(627), 1425–1437.
<http://dx.doi.org/10.1002/qj.132>. Récupéré de
<http://doi.wiley.com/10.1002/qj.132>
- Baran, A. J. (2009). A review of the light scattering properties of cirrus. *Journal of Quantitative Spectroscopy and Radiative Transfer*, 110(14-16), 1239–1260. <http://dx.doi.org/10.1016/j.jqsrt.2009.02.026>. Récupéré de <http://dx.doi.org/10.1016/j.jqsrt.2009.02.026>

- Batchelor, R. L., Strong, K., Lindenmaier, R., Mittermeier, R. L., Fast, H., Drummond, J. R., Fogal, P. F., Batchelor, R. L., Strong, K., Lindenmaier, R., Mittermeier, R. L., Fast, H., Drummond, J. R. et Fogal, P. F. (2009). A New Bruker IFS 125HR FTIR Spectrometer for the Polar Environment Atmospheric Research Laboratory at Eureka, Nunavut, Canada : Measurements and Comparison with the Existing Bomem DA8 Spectrometer. *Journal of Atmospheric and Oceanic Technology*, 26(7), 1328–1340. <http://dx.doi.org/10.1175/2009JTECHA1215.1>. Récupéré de <http://journals.ametsoc.org/doi/abs/10.1175/2009JTECHA1215.1>
- Bellisario, C., Brindley, H. E., Murray, J. E., Last, A., Pickering, J., Harlow, R. C., Fox, S., Fox, C., Newman, S. M., Smith, M., Anderson, D., Huang, X. et Chen, X. (2017). Retrievals of the Far Infrared Surface Emissivity Over the Greenland Plateau Using the Tropospheric Airborne Fourier Transform Spectrometer (TAFTS). *Journal of Geophysical Research : Atmospheres*, 122(22), 12,152–12,166. <http://dx.doi.org/10.1002/2017JD027328>. Récupéré de <http://doi.wiley.com/10.1002/2017JD027328>
- Berk, A., Anderson, G. P., Acharya, P. K., Bernstein, L. S., Muratov, L., Lee, J., Fox, M., Adler-Golden, S. M., Chetwynd, J. H., Hoke, M. L., Lockwood, R. B., Gardner, J. A., Cooley, T. W., Borel, C. C. et Lewis, P. E. (2005). MODTRAN 5 : a reformulated atmospheric band model with auxiliary species and practical multiple scattering options : update. volume 5806, p. 662. International Society for Optics and Photonics. <http://dx.doi.org/10.1117/12.606026>. Récupéré de <http://proceedings.spiedigitallibrary.org/proceeding.aspx?doi=10.1117/12.606026>
- Blanchard, Y., Royer, A., O'Neill, N. T., Turner, D. D. et Eloranta, E. W. (2017). Thin ice clouds in the Arctic : Cloud optical depth and particle size retrieved from ground-based thermal infrared radiometry. *Atmospheric Measurement Techniques*, 10(6), 2129–2147. <http://dx.doi.org/10.5194/amt-10-2129-2017>
- Blanchet, J. P. et Girard, É. (1995). Water vapor-temperature feedback in the formation of continental Arctic air : its implication for climate. *Science of the Total Environment*, 160-161(C), 793–802. [http://dx.doi.org/10.1016/0048-9697\(95\)04412-T](http://dx.doi.org/10.1016/0048-9697(95)04412-T)
- Blanchet, J.-P., Royer, A., Châteauneuf, F., Bouzid, Y., Blanchard, Y., Hamel, J.-F., de Lafontaine, J., Gauthier, P., O'Neill, N. T., Pancratii, O. et Garand, L. (2011). TICFIRE : a far infrared payload to monitor the

evolution of thin ice clouds. *SPIE 4485, Optical Spectroscopic Techniques, Remote Sensing, and Instrumentation for Atmospheric and Space Research IV*, 8176, 81761K–81761K-11. <http://dx.doi.org/10.1117/12.898577>. Récupéré de <http://dx.doi.org/10.1117/12.898577>

Bourdages, L., Duck, T. J., Lesins, G., Drummond, J. R. et Eloranta, E. W. (2009). Physical properties of High Arctic tropospheric particles during winter. *Atmospheric Chemistry and Physics*, 9(18), 6881–6897. <http://dx.doi.org/10.5194/acp-9-6881-2009>. Récupéré de <http://www.atmos-chem-phys.net/9/6881/2009/>

Canas, T. A., Murray, J. E. et Harries, J. E. (1997). Tropospheric airborne Fourier transform spectrometer (TAFTS). volume 3220, p. 91. International Society for Optics and Photonics. <http://dx.doi.org/10.1117/12.301139>. Récupéré de <http://proceedings.spiedigitallibrary.org/proceeding.aspx?doi=10.1117/12.301139>

Clothiaux, E. E., Ackerman, T. P., Mace, G. G., Moran, K. P., Marchand, R. T., Miller, M. A. et Martner, B. E. (2000). Objective Determination of Cloud Heights and Radar Reflectivities Using a Combination of Active Remote Sensors at the ARM CART Sites. *Journal of Applied Meteorology*, 39(5), 645–665. [http://dx.doi.org/10.1175/1520-0450\(2000\)039<0645:ODOCHA>2.0.CO;2](http://dx.doi.org/10.1175/1520-0450(2000)039<0645:ODOCHA>2.0.CO;2). Récupéré de <http://journals.ametsoc.org/doi/abs/10.1175/1520-0450%282000%29039%3C0645%3AODOCHA%3E2.0.CO%3B2>

Clough, S. A., Iacono, M. J. et Moncet, J.-L. (1992). Line-by-line calculations of atmospheric fluxes and cooling rates : Application to water vapor. *Journal of Geophysical Research*, 97(D14), 15761. <http://dx.doi.org/10.1029/92JD01419>. Récupéré de <http://doi.wiley.com/10.1029/92JD01419>

Clough, S. A., Shephard, M. W., Mlawer, E. J., Delamere, J. S., Iacono, M. J., Cady-Pereira, K. E., Boukabara, S. et Brown, P. D. (2005). Atmospheric radiative transfer modeling : A summary of the AER codes. *Journal of Quantitative Spectroscopy and Radiative Transfer*, 91(2), 233–244. <http://dx.doi.org/10.1016/j.jqsrt.2004.05.058>

Cox, C. J., Turner, D. D., Rowe, P. M., Shupe, M. D. et Walden, V. P. (2014). Cloud microphysical properties retrieved from downwelling infrared radiance measurements made at Eureka, Nunavut, Canada (2006-09). *Journal of Applied Meteorology and Climatology*, 53(3), 772–791. <http://dx.doi.org/10.1175/JAMC-D-13-0113.1>

- Curry, J. et Curry, J. (1983). On the Formation of Continental Polar Air. *Journal of the Atmospheric Sciences*, 40(9), 2278–2292. [http://dx.doi.org/10.1175/1520-0469\(1983\)040<2278:OTFOP>2.0.CO;2](http://dx.doi.org/10.1175/1520-0469(1983)040<2278:OTFOP>2.0.CO;2). Récupéré de [http://journals.ametsoc.org/doi/abs/10.1175/1520-0469\(1983\)040%281983%29040%3C2278%3AOTFOP%3E2.0.CO%3B2](http://journals.ametsoc.org/doi/abs/10.1175/1520-0469(1983)040%281983%29040%3C2278%3AOTFOP%3E2.0.CO%3B2)
- Delanoë, J. M. E. et Hogan, R. J. (2008). A variational scheme for retrieving ice cloud properties from combined radar, lidar, and infrared radiometer. *Journal of Geophysical Research Atmospheres*, 113(7), D07204. <http://dx.doi.org/10.1029/2007JD009000>. Récupéré de <http://doi.wiley.com/10.1029/2007JD009000>
- Dirksen, R. J., Sommer, M., Immel, F. J., Hurst, D. F., Kivi, R. et Vömel, H. (2014). Reference quality upper-air measurements : GRUAN data processing for the Vaisala RS92 radiosonde. *Atmos. Meas. Tech*, 7, 4463–4490. <http://dx.doi.org/10.5194/amt-7-4463-2014>. Récupéré de www.atmos-meas-tech.net/7/4463/2014/
- Donovan, D. P. et Van Lammeren, A. C. (2001). Cloud effective particle size and water content profile retrievals using combined lidar and radar observations 1. Theory and examples. *Journal of Geophysical Research Atmospheres*, 106(D21), 27425–27448. <http://dx.doi.org/10.1029/2001JD900243>. Récupéré de <http://doi.wiley.com/10.1029/2001JD900243>
- Doyle, J. G., Lesins, G., Thackray, C. P., Perro, C., Nott, G. J., Duck, T. J., Damoah, R. et Drummond, J. R. (2011). Water vapor intrusions into the High Arctic during winter. *Geophysical Research Letters*, 38(12), n/a–n/a. <http://dx.doi.org/10.1029/2011GL047493>. Récupéré de <http://doi.wiley.com/10.1029/2011GL047493>
- Eloranta, E. et Ponsardin, P. (2001). A high spectral resolution Lidar designed for unattended operation in the Arctic. Dans *Optical Remote Sensing*, p. OMC4., Washington, D.C. OSA. <http://dx.doi.org/10.1364/ORS.2001.OMC4>. Récupéré de <https://www.osapublishing.org/abstract.cfm?uri=ORS-2001-OMC4>
- Fox, C., Green, P. D., Pickering, J. C. et Humpage, N. (2015). Analysis of far-infrared spectral radiance observations of the water vapor continuum in the Arctic. *Journal of Quantitative Spectroscopy and Radiative Transfer*, 155, 57–65. <http://dx.doi.org/10.1016/J.JQSRT.2015.01.001>. Récupéré de <https://www.sciencedirect.com/science/article/pii/S0022407315000023>

- Grenier, P., Blanchet, J.-p. et Mu ?oz-Alpizar, R. (2009). Study of polar thin ice clouds and aerosols seen by CloudSat and CALIPSO during midwinter 2007. *Journal of Geophysical Research Atmospheres*, 114(9).
<http://dx.doi.org/10.1029/2008JD010927>
- Hagemann, S., Bengtsson, L. et Genthert, G. (2003). On the determination of atmospheric water vapor from GPS measurements. *Journal of Geophysical Research : Atmospheres*, 108(D21).
<http://dx.doi.org/10.1029/2002JD003235>. Récupéré de
<http://doi.wiley.com/10.1029/2002JD003235>
- Harries, J., Carli, B., Rizzi, R., Serio, C., Mlynczak, M., Palchetti, L., Maestri, T., Brindley, H. et Masiello, G. (2008). THE FAR-INFRARED EARTH. *Reviews of Geophysics*, 46(2007), 1–34.
<http://dx.doi.org/10.1029/2007RG000233.1.INTRODUCTION>
- Heidinger, A. K. et Pavolonis, M. J. (2009). Gazing at cirrus clouds for 25 years through a split window. Part I : Methodology. *Journal of Applied Meteorology and Climatology*, 48(6), 1100–1116.
<http://dx.doi.org/10.1175/2008JAMC1882.1>. Récupéré de
<http://journals.ametsoc.org/doi/abs/10.1175/2008JAMC1882.1>
- Holton, J. R., Haynes, P. H., McIntyre, M. E., Douglass, A. R., Rood, R. B. et Pfister, L. (1995). Stratosphere-troposphere exchange.
<http://dx.doi.org/10.1029/95RG02097>. Récupéré de
<http://doi.wiley.com/10.1029/95RG02097>
- Inoue, T. (1985). On the Temperature Measurements and Effective Cirrus Emissivity Clouds by Window Determination Region of Semi-Transparent in the. *Journal of the Meteorological Society of Japan*, 63(1973), 88–99.
Récupéré de https://www.jstage.jst.go.jp/article/jmsj1965/63/1/63_{_}1_{_}88/{}pdf/-char/ja
- IPCC. (2013). *Climate Change 2013 : The Physical Science Basis. Contribution of Working Group I to the Fifth Assessment Report of the Intergovernmental Panel on Climate Change*. Cambridge : Cambridge University Press. <http://dx.doi.org/10.1017/CBO9781107415324>. Récupéré de www.climatechange2013.org
- Jensen, E. J., Diskin, G. S., Lawson, R. P., Lance, S., Bui, T. P., Hlavka, D., McGill, M., Pfister, L., Toon, O. B. et Gao, R. (2013). Ice nucleation and dehydration in the Tropical Tropopause Layer. *Proceedings of the National Academy of Sciences*, 110(6), 2041–2046.
<http://dx.doi.org/10.1073/pnas.1217104110>. Récupéré de

<http://www.pnas.org/cgi/doi/10.1073/pnas.1217104110>
<http://www.pnas.org/content/pnas/110/6/2041.full.pdf>

Jensen, E. J., Pfister, L., Bui, T. V., Lawson, P., Baker, B., Mo, Q., Baumgardner, D., Weinstock, E. M., Smith, J. B., Moyer, E. J., Hanisco, T. F., Sayres, D. S., Clair, J. M. S., Alexander, M. J., Toon, O. B. et Smith, J. A. (2008). Formation of large ($100 \mu\text{m}$) ice crystals near the tropical tropopause. *Atmospheric Chemistry and Physics*, 8(6), 1621–1633.
<http://dx.doi.org/10.5194/acp-8-1621-2008>. Récupéré de www.atmos-chem-phys.net/8/1621/2008/

Jouan, C., Girard, É., Pelon, J., Gultepe, I., Delanoë, J. et Blanchet, J. P. (2012). Characterization of Arctic ice cloud properties observed during ISDAC. *Journal of Geophysical Research Atmospheres*, 117(23), 1–23.
<http://dx.doi.org/10.1029/2012JD017889>

Jouan, C., Pelon, J., Girard, É., Ancellet, G., Blanchet, J.-p. et Delanoë, J. (2014). On the relationship between Arctic ice clouds and polluted air masses over the North Slope of Alaska in April 2008. *Atmospheric Chemistry and Physics*, 14(3), 1205–1224. <http://dx.doi.org/10.5194/acp-14-1205-2014>

King, M. D., Kaufman, Y. J., Menzel, W. P. et Tanre, D. (1992). Remote-sensing of cloud, aerosol, and water-vapor properties from the moderate resolution imaging spectrometer (modis). *Ieee Transactions On Geoscience Remote Sensing*, 30(i), 2–27.

Klett, J. D. (1985). Lidar inversion with variable backscatter/extinction ratios. *Applied Optics*, 24(11), 1638.
<http://dx.doi.org/10.1364/AO.24.001638>. Récupéré de <https://www.osapublishing.org/abstract.cfm?URI=ao-24-11-1638>

Knuteson, R. et Revercomb, H. (2004). Atmospheric emitted radiance interferometer. Part I : Instrument design. ... of *Atmospheric and ...*, 21(12), 1763–1777. <http://dx.doi.org/10.1175/JTECH-1662.1>. Récupéré de <http://journals.ametsoc.org/doi/abs/10.1175/JTECH-1662.1>

Koop, T., Luo, B., Tsias, A. et Peter, T. (2000). Water activity as the determinant for homogeneous ice nucleation in aqueous solutions. *Nature*, 406(6796), 611–614. <http://dx.doi.org/10.1038/35020537>. Récupéré de <http://www.nature.com/doifinder/10.1038/35020537>

Krämer, M., Rolf, C., Luebke, A., Afchine, A., Spelten, N., Costa, A., Meyer, J., Zöger, M., Smith, J., Herman, R. L., Buchholz, B., Ebert, V., Baumgardner, D., Borrmann, S., Klingebiel, M. et Avallone, L. (2016). A microphysics guide to cirrus clouds-Part 1 : Cirrus types. *Atmospheric*

- Chemistry and Physics*, 16(5), 3463–3483.
<http://dx.doi.org/10.5194/acp-16-3463-2016>. Récupéré de
www.atmos-chem-phys.net/16/3463/2016/
- Krämer, M., Schiller, C., Afchine, A., Bauer, R., Gensch, I., Mangold, A., Schlicht, S., Spelten, N., Sitnikov, N., Borrmann, S., De Reus, M. et Spichtinger, P. (2009). Ice supersaturations and cirrus cloud crystal numbers. *Atmospheric Chemistry and Physics*, 9(11), 3505–3522.
<http://dx.doi.org/10.5194/acp-9-3505-2009>. Récupéré de
www.atmos-chem-phys.net/9/3505/2009/
- Latvakoski, H., Mlynczak, M. G., Johnson, D. G., Cageao, R. P., Kratz, D. P. et Johnson, K. (2013). Far-infrared spectroscopy of the troposphere : instrument description and calibration performance. *Appl. Opt.*, 52(January 2013), 264–273. <http://dx.doi.org/10.1364/AO.52.000264>. Récupéré de
<http://ao.osa.org/abstract.cfm?URI=ao-52-2-264>
- Lesins, G., Duck, T. J. et Drummond, J. R. (2010). Climate trends at Eureka in the Canadian high arctic. *Atmosphere-Ocean*, 48(2), 59–80.
<http://dx.doi.org/10.3137/A01103.2010>. Récupéré de
<http://www.tandfonline.com/doi/abs/10.3137/A01103.2010>
- Libois, Q. et Blanchet, J. P. (2017). Added value of far-infrared radiometry for remote sensing of ice clouds. *Journal of Geophysical Research*, 122(12), 6541–6564. <http://dx.doi.org/10.1002/2016JD026423>. Récupéré de
<http://doi.wiley.com/10.1002/2016JD026423>
- Libois, Q., Ivanescu, L., Blanchet, J. P., Schulz, H., Bozem, H., Leaitch, W. R., Burkart, J., Abbatt, J. P., Herber, A. B., Aliabadi, A. A. et Girard, É. (2016a). Airborne observations of far-infrared upwelling radiance in the Arctic. *Atmospheric Chemistry and Physics*, 16(24), 15689–15707.
<http://dx.doi.org/10.5194/acp-16-15689-2016>. Récupéré de
www.atmos-chem-phys.net/16/15689/2016/
- Libois, Q., Proulx, C., Ivanescu, L., Coursol, L., Pelletier, L. S., Bouzid, Y., Barbero, F., Girard, É. et Blanchet, J.-p. (2016b). A microbolometer-based far infrared radiometer to study thin ice clouds in the Arctic. *Atmospheric Measurement Techniques*, 9(4), 1817–1832.
<http://dx.doi.org/10.5194/amt-9-1817-2016>
- Liu, Y., Ackerman, S. A., Maddux, B. C., Key, J. R., Frey, R. A., Liu, Y., Ackerman, S. A., Maddux, B. C., Key, J. R. et Frey, R. A. (2010). Errors in Cloud Detection over the Arctic Using a Satellite Imager and Implications for Observing Feedback Mechanisms. *Journal of Climate*, 23(7), 1894–1907.

<http://dx.doi.org/10.1175/2009JCLI3386.1>. Récupéré de
<http://journals.ametsoc.org/doi/abs/10.1175/2009JCLI3386.1>

Mariani, Z., Strong, K. et Drummond, J. R. (2016). Distributions of Downwelling Radiance at 10 and 20 μm in the High Arctic. *Atmosphere - Ocean*, 54(5), 529–540.

<http://dx.doi.org/10.1080/07055900.2016.1216825>. Récupéré de
<https://www.tandfonline.com/doi/full/10.1080/07055900.2016.1216825>

Mariani, Z., Strong, K., Palm, M., Lindenmaier, R., Adams, C., Zhao, X., Savastiouk, V., McElroy, C. T., Goutail, F. et Drummond, J. R. (2013). Year-round retrievals of trace gases in the arctic using the extended-range atmospheric emitted radiance interferometer. *Atmospheric Measurement Techniques*, 6(6), 1549–1565.

<http://dx.doi.org/10.5194/amt-6-1549-2013>. Récupéré de
www.atmos-meas-tech.net/6/1549/2013/

Mariani, Z., Strong, K., Wolff, M., Rowe, P. M., Walden, V. P., Fogal, P., Duck, T. J., Lesins, G., Turner, D. S., Cox, C. J., Eloranta, E. W., Drummond, J. R., Roy, C., Turner, D. D., Hudak, D. R. et Lindenmaier, I. A. (2012). Infrared measurements in the Arctic using two Atmospheric Emitted Radiance Interferometers. *Atmospheric Measurement Techniques*, 5(2), 329–344. <http://dx.doi.org/10.5194/amt-5-329-2012>

Mast, J. C., Mlynczak, M. G., Cageao, R. P., Kratz, D. P., Latvakoski, H., Johnson, D. G., Turner, D. D. et Mlawer, E. J. (2017). Measurements of downwelling far-infrared radiance during the RHUBC-II campaign at Cerro Toco, Chile and comparisons with line-by-line radiative transfer calculations. *Journal of Quantitative Spectroscopy and Radiative Transfer*, 198, 25–39.
<http://dx.doi.org/10.1016/J.JQSRT.2017.04.028>. Récupéré de <https://www.sciencedirect.com/science/article/pii/S0022407316308949>

Matrosov, S. Y., Korolev, A. V. et Heymsfield, A. J. (2002). Profiling cloud ice mass and particle characteristic size from doppler radar measurements. *Journal of Atmospheric and Oceanic Technology*, 19(7), 1003–1018. [http://dx.doi.org/10.1175/1520-0426\(2002\)019<1003:PCIMAP>2.0.CO;2](http://dx.doi.org/10.1175/1520-0426(2002)019<1003:PCIMAP>2.0.CO;2).
Récupéré de [http://journals.ametsoc.org/doi/pdf/10.1175/1520-0426\(2002\)019<1003:PCIMAP>2.0.CO;2](http://journals.ametsoc.org/doi/pdf/10.1175/1520-0426(2002)019<1003:PCIMAP>2.0.CO;2)

Mccullough, E. M., Sica, R. J., Drummond, J. R., Nott, G., Perro, C., Thackray, C. P., Hopper, J., Doyle, J., Duck, T. J. et Walker, K. A. (2017). Depolarization calibration and measurements using the CANDAC Rayleigh–Mie–Raman lidar at Eureka, Canada. *Atmos. Meas. Tech*, 10,

4253–4277. <http://dx.doi.org/10.5194/amt-10-4253-2017>. Récupéré de <https://doi.org/10.5194/amt-10-4253-2017>

Merrelli, A. et Turner, D. D. (2013). Information content for cloud ice microphysics in the FIR radiance spectrum. Dans *AIP Conference Proceedings*, volume 1531, 348–351. <http://dx.doi.org/10.1063/1.4804778>

Miloshevich, L. M., Paukkunen, A., Mel, H. V., Oltmans, S. J., Vömel, H. et Oltmans, S. J. (2004). Development and validation of a time-lag correction for Vaisala radiosonde humidity measurements. *Journal of Atmospheric and Oceanic Technology*, 21(9), 1305–1327. [http://dx.doi.org/10.1175/1520-0426\(2004\)021<1305:DAVOAT>2.0.CO;2](http://dx.doi.org/10.1175/1520-0426(2004)021<1305:DAVOAT>2.0.CO;2). Récupéré de [http://journals.ametsoc.org/doi/pdf/10.1175/1520-0426\(2004\)021<1305:DAVOAT>2.0.CO;2](http://journals.ametsoc.org/doi/pdf/10.1175/1520-0426(2004)021<1305:DAVOAT>2.0.CO;2)

Miloshevich, L. M., Vömel, H., Whiteman, D. N. et Leblanc, T. (2009). Accuracy assessment and correction of Vaisala RS92 radiosonde water vapor measurements. *Journal of Geophysical Research Atmospheres*, 114(11), 1–23. <http://dx.doi.org/10.1029/2008JD011565>

Mlynczak, M. G., Cageao, R. P., Mast, J. C., Kratz, D. P., Latvakoski, H. et Johnson, D. G. (2016). Observations of downwelling far-infrared emission at Table Mountain California made by the FIRST instrument. *Journal of Quantitative Spectroscopy and Radiative Transfer*, 170, 90–105. <http://dx.doi.org/10.1016/j.jqsrt.2015.10.017>. Récupéré de <http://dx.doi.org/10.1016/j.jqsrt.2015.10.017>

Mlynczak, M. G., Johnson, D. G., Latvakoski, H., Jucks, K., Watson, M., Kratz, D. P., Bingham, G., Traub, W. A., Wellard, S. J., Hyde, C. R. et Liu, X. (2006). First light from the Far-Infrared Spectroscopy of the Troposphere (FIRST) instrument. *Geophysical Research Letters*, 33(7), L07704. <http://dx.doi.org/10.1029/2005GL025114>. Récupéré de <http://doi.wiley.com/10.1029/2005GL025114>

Mlynczak, M. G., Wielicki, B., Kratz, D., Charlock, T., Johnson, D. et Gazarik, M. (2005). The Far-Infrared Spectrum Exploring a New Frontier in the Remote Sensing of Earth's Climate - white paper. *National Research Council*, (January). <http://dx.doi.org/10.1364/HISE.2007.HMA1>

Moran, K. P., Mariner, B. E., Post, M. J., Kropfli, R. A., Welsh, D. C. et Widener, K. B. (1998). An Unattended Cloud-Profilng Radar for Use in Climate Research. *Bulletin of the American Meteorological Society*, 79(3), 443–455. [http://dx.doi.org/10.1175/1520-0477\(1998\)079<0443:AUCPRF>2.0.CO;2](http://dx.doi.org/10.1175/1520-0477(1998)079<0443:AUCPRF>2.0.CO;2). Récupéré de

[http://journals.ametsoc.org/doi/abs/10.1175/1520-0477\(2011\)281998\(290793C0443\)3AAUCPRF\(3E2.0.CO\(3B2](http://journals.ametsoc.org/doi/abs/10.1175/1520-0477(2011)281998(290793C0443)3AAUCPRF(3E2.0.CO(3B2)

Ngo Phong, L., Proulx, C., Oulachgar, H. et Châteauneuf, F. (2015). Far infrared microbolometers for radiometric measurements of ice cloud. *Proc. of SPIE*, 9375, 93750G. <http://dx.doi.org/10.1117/12.2076219>. Récupéré de <http://proceedings.spiedigitallibrary.org/proceeding.aspx?doi=10.1117/12.2076219>

Nott, G. J., Duck, T. J., Doyle, J. G., Coffin, M. E., Perro, C., Thackray, C. P., Drummond, J. R., Fogal, P. F., McCullough, E. et Sica, R. J. (2012). A remotely operated lidar for aerosol, temperature, and water vapor profiling in the high arctic. *Journal of Atmospheric and Oceanic Technology*, 29(2), 221–234. <http://dx.doi.org/10.1175/JTECH-D-11-00046.1>. Récupéré de <https://journals.ametsoc.org/doi/pdf/10.1175/JTECH-D-11-00046.1>

Palchetti, L., Belotti, C., Bianchini, G., Castagnoli, F., Carli, B., Cortesi, U., Pellegrini, M., Camy-Peyret, C., Jeseck, P. et Té, Y. (2006). Technical note : First spectral measurement of the Earth's upwelling emission using an uncooled wideband Fourier transform spectrometer. *Atmospheric Chemistry and Physics*, 6(12), 5025–5030.

<http://dx.doi.org/10.5194/acp-6-5025-2006>. Récupéré de www.atmos-chem-phys.net/6/5025/2006/

Palchetti, L., Bianchini, G., Di Natale, G. et Del Guasta, M. (2015). Far-infrared radiative properties of water vapor and clouds in Antarctica. *Bulletin of the American Meteorological Society*, 96(9), 1505–1518.
<http://dx.doi.org/10.1175/BAMS-D-13-00286.1>

Palchetti, L., Di Natale, G., Bianchini, G., Natale, G. D., Nazionale, C., Nazionale, I. et Fiorentino, S. (2016a). Remote sensing of cirrus cloud microphysical properties using spectral measurements over the full range of their thermal emission. *Journal of Geophysical Research : Atmospheres*, 121(18), 1–16. <http://dx.doi.org/10.1002/2016JD025162.1>.

Palchetti, L., Olivieri, M., Pompei, C., Labate, D., Brindley, H., Di Natale, G. et Bianchini, G. (2016b). The Far Infrared FTS for the FORUM Mission. Dans *Light, Energy and the Environment*, p. FTu3C.1., Washington, D.C. OSA. <http://dx.doi.org/10.1364/FTS.2016.FTu3C.1>. Récupéré de <https://www.osapublishing.org/abstract.cfm?URI=FTS-2016-FTu3C.1>

Paton, J. (1948). THE OPTICAL PROPERTIES OF THE ATMOSPHERE. *Weather*, 3(8), 243–249.
<http://dx.doi.org/10.1002/j.1477-8696.1948.tb00925.x>. Récupéré de

<http://www.dtic.mil/docs/citations/AD0753075>

Proulx, C., Williamson, F., Allard, M., Baldenberger, G., Gay, D., Garcia-Blanco, S., Cote, P., Martin, L., Larouche, C., Ilias, S., Pope, T., Caldwell, M., Ward, K. et Delderfield, J. (2009). The EarthCARE broadband radiometer detectors. *Proceedings of SPIE*, 7453, 74530S–74530S-11.

<http://dx.doi.org/10.1117/12.829935>. Récupéré de
<http://link.aip.org/link/PSISDG/v7453/i1/p74530S/s1{&}Agg=doi>

Revercomb, H. E., Buijs, H., Howell, H. B., Laporte, D. D., Smith, W. L. et Sromovsky, L. a. (1988). Radiometric calibration of IR Fourier transform spectrometers : solution to a problem with the High-Resolution Interferometer Sounder. *Applied optics*, 27(15), 3210–3218.

<http://dx.doi.org/10.1364/AO.27.003210>

Ricaud, P., Gabard, B., Derrien, S., Chaboureau, J. P., Rose, T., Mombauer, A. et Czekala, H. (2010). HAMSTRAD-tropo, A 183-GHz radiometer dedicated to sound tropospheric water vapor over concordia station, Antarctica. *IEEE Transactions on Geoscience and Remote Sensing*, 48(3 PART2), 1365–1380. <http://dx.doi.org/10.1109/TGRS.2009.2029345>

Rochette, L., Smith, W. L., Howard, M. et Bratcher, T. (2009). Atmospheric Sounder Spectrometer for Infrared Spectral Technology : Latest development & improvement in the Atmospheric sounding technology. *Proc. SPIE 7457, Imaging Spectrometry XIV*, 7457, 745702–745702–9.

<http://dx.doi.org/10.1117/12.829344>. Récupéré de
<http://proceedings.spiedigitallibrary.org/proceeding.aspx?articleid=787813>

Rodgers, C. D. (2000). Inverse Methods for Atmospheric Sounding - Theory and Practice. 2(January), 256.

<http://dx.doi.org/10.1142/9789812813718>. Récupéré de <http://ebooks.worldscinet.com/ISBN/9789812813718/9789812813718.html>

Rothman, L. S., Gordon, I. E., Babikov, Y., Barbe, A., Chris Benner, D., Bernath, P. F., Birk, M., Bizzocchi, L., Boudon, V., Brown, L. R., Campargue, A., Chance, K., Cohen, E. A., Coudert, L. H., Devi, V. M., Drouin, B. J., Fayt, A., Flaud, J. M., Gamache, R. R., Harrison, J. J., Hartmann, J. M., Hill, C., Hodges, J. T., Jacquemart, D., Jolly, A., Lamouroux, J., Le Roy, R. J., Li, G., Long, D. A., Lyulin, O. M., Mackie, C. J., Massie, S. T., Mikhailenko, S., Müller, H. S., Naumenko, O. V., Nikitin, A. V., Orphal, J., Perevalov, V., Perrin, A., Polovtseva, E. R., Richard, C., Smith, M. A., Starikova, E., Sung, K., Tashkun, S., Tennyson, J., Toon, G. C., Tyuterev, V. G. et Wagner, G. (2013). The HITRAN2012 molecular

- spectroscopic database. *Journal of Quantitative Spectroscopy and Radiative Transfer*, 130, 4–50. <http://dx.doi.org/10.1016/j.jqsrt.2013.07.002>
- Rowe, P. M., Miloshevich, L. M., Turner, D. D. et Walden, V. P. (2008). Dry bias in Vaisala RS90 radiosonde humidity profiles over Antarctica. *Journal of Atmospheric and Oceanic Technology*, 25(9), 1529–1541.
<http://dx.doi.org/10.1175/2008JTECHA1009.1>
- Shahabadi, M. B. et Huang, Y. (2014). Measuring Stratospheric H₂O with an Airborne Spectrometer. *Journal of Atmospheric and Oceanic Technology*, 31(7), 1502–1515. <http://dx.doi.org/10.1175/JTECH-D-13-00191.1>.
Récupéré de
<http://journals.ametsoc.org/doi/abs/10.1175/JTECH-D-13-00191.1>
- Shine, K. P., Ptashnik, I. V. et Rädel, G. (2012). The Water Vapour Continuum : Brief History and Recent Developments. *Surveys in Geophysics*, 33(3-4), 535–555. <http://dx.doi.org/10.1007/s10712-011-9170-y>
- Shupe, M. D. (2007). A ground-based multisensor cloud phase classifier. *Geophysical Research Letters*, 34(22), 1–5.
<http://dx.doi.org/10.1029/2007GL031008>
- Shupe, M. D. (2011). Clouds at arctic atmospheric observatories. Part II : Thermodynamic phase characteristics. *Journal of Applied Meteorology and Climatology*, 50(3), 645–661. <http://dx.doi.org/10.1175/2010JAMC2468.1>.
Récupéré de
<http://journals.ametsoc.org/doi/abs/10.1175/2010JAMC2468.1>
- Sirois, A. et Barrie, L. a. (1999). Arctic lower tropospheric aerosol trends and composition at Alert, Canada : 1980–1995. *Journal of Geophysical Research*, 104, 11599. <http://dx.doi.org/10.1029/1999JD900077>
- Solomon, S., Rosenlof, K. H., Portmann, R. W., Daniel, J. S., Davis, S. M., Sanford, T. J. et Plattner, G.-K. (2010). Contributions of stratospheric water vapor to decadal changes in the rate of global warming. *Science (New York, N.Y.)*, 327(5970), 1219–23. <http://dx.doi.org/10.1126/science.1182488>.
Récupéré de <http://www.ncbi.nlm.nih.gov/pubmed/20110466>
- Stamnes, K., Tsay, S.-C., Wiscombe, W. et Jayaweera, K. (1988). Numerically stable algorithm for discrete-ordinate-method radiative transfer in multiple scattering and emitting layered media. *Applied Optics*, 27(12), 2502. <http://dx.doi.org/10.1364/AO.27.002502>. Récupéré de
<https://www.osapublishing.org/abstract.cfm?URI=ao-27-12-2502>
- Stephens, G. L., Vane, D. G., Boain, R. J., Mace, G. G., Sassen, K., Wang,

- Z., Illingworth, A. J., O'connor, E. J., Rossow, W. B., Durden, S. L., Miller, S. D., Austin, R. T., Benedetti, A., Mitrescu, C., Team, t. C. S., Stephens, G. L., Vane, D. G., Boain, R. J., Mace, G. G., Sassen, K., Wang, Z., Illingworth, A. J., O'connor, E. J., Rossow, W. B., Durden, S. L., Miller, S. D., Austin, R. T., Benedetti, A., Mitrescu, C. et Team, t. C. S. (2002). THE CLOUDSAT MISSION AND THE A-TRAIN. *Bulletin of the American Meteorological Society*, 83(12), 1771–1790.
<http://dx.doi.org/10.1175/BAMS-83-12-1771>. Récupéré de
<http://journals.ametsoc.org/doi/10.1175/BAMS-83-12-1771>
- Sullivan, R. C., Petters, M. D., DeMott, P. J., Kreidenweis, S. M., Wex, H., Niedermeier, D., Hartmann, S., Clauss, T., Stratmann, F., Reitz, P., Schneider, J. et Sierau, B. (2010). Irreversible loss of ice nucleation active sites in mineral dust particles caused by sulphuric acid condensation. *Atmospheric Chemistry and Physics*, 10(23), 11471–11487.
<http://dx.doi.org/10.5194/acp-10-11471-2010>. Récupéré de
www.atmos-chem-phys.net/10/11471/2010/
- Sullivan, S. C., Morales Betancourt, R., Barahona, D. et Nenes, A. (2016). Understanding cirrus ice crystal number variability for different heterogeneous ice nucleation spectra. *Atmospheric Chemistry and Physics*, 16(4), 2611–2629. <http://dx.doi.org/10.5194/acp-16-2611-2016>. Récupéré de www.atmos-chem-phys.net/16/2611/2016/
- Tobin, D. C., Best, F. a., Brown, P. D., Clough, S. A., Dedecker, R. G., Ellingson, R. G., Garcia, R. K., Howell, H. B., Knuteson, R. O., Mlawer, E. J., Revercomb, H. E., Short, J. F., van Delst, P. F. W. et Walden, V. P. (1999). Downwelling spectral radiance observations at the SHEBA ice station : Water vapor continuum measurements from 17 to 26 μ m. *Journal of Geophysical Research*, 104(D2), 2081.
<http://dx.doi.org/10.1029/1998JD200057>. Récupéré de
<http://onlinelibrary.wiley.com/doi/10.1029/1998JD200057/full>
- Turner, D. D. (2005). Arctic Mixed-Phase Cloud Properties from AERI Lidar Observations : Algorithm and Results from SHEBA. *Journal of Applied Meteorology*, 44(4), 427–444. <http://dx.doi.org/10.1175/JAM2208.1>
- Turner, D. D., Clough, S. A., Liljegren, J. C., Cady-Pereira, K., Clough, S. A., Clothiaux, E. E., Cady-Pereira, K. E. et Gaustad, K. L. (2007). Satellite observations of ammonia View project Retrieving Liquid Water Path and Precipitable Water Vapor From the Atmospheric Radiation Measurement (ARM) Microwave Radiometers. *IEEE TRANSACTIONS ON GEOSCIENCE AND REMOTE SENSING*, 45(11).

<http://dx.doi.org/10.1109/TGRS.2007.903703>. Récupéré de
www.radiometrics.com

Turner, D. D. et Mlawer, E. J. (2010). The radiative heating in underexplored bands campaigns. *Bulletin of the American Meteorological Society*, 91(7), 911–923. <http://dx.doi.org/10.1175/2010BAMS2904.1>

Vaisala (2013). *Vaisala Radiosonde RS92 Performance in the WMO Intercomparison of High Quality Radiosonde Systems*. Rapport technique

Wang, C., Platnick, S., Zhang, Z., Meyer, K. et Yang, P. (2016). Retrieval of ice cloud properties using an optimal estimation algorithm and MODIS infrared observations : 1. Forward model, error analysis, and information content. *Journal of Geophysical Research : Atmospheres*, 121(10), 5809–5826. <http://dx.doi.org/10.1002/2015JD024526>. Récupéré de
<http://doi.wiley.com/10.1002/2015JD024526>

Weaver, D., Strong, K., Schneider, M., Rowe, P. M., Sioris, C., Walker, K. A., Mariani, Z., Uttal, T., Thomas McElroy, C., Vömel, H., Spassiani, A. et Drummond, J. R. (2017). Intercomparison of atmospheric water vapour measurements at a Canadian High Arctic site. *Atmospheric Measurement Techniques*, 10(8), 2851–2880.
<http://dx.doi.org/10.5194/amt-10-2851-2017>

Winker, D. M., Pelon, J. R. et McCormick, M. P. (2003). The CALIPSO mission : spaceborne lidar for observation of aerosols and clouds. 4893, 1. <http://dx.doi.org/10.1117/12.466539>. Récupéré de
<http://proceedings.spiedigitallibrary.org/proceeding.aspx?doi=10.1117/12.466539>

Wunch, D., Toon, G. C., Blavier, J.-F. L., Washenfelder, R. A., Notholt, J., Connor, B. J., Griffith, D. W. T., Sherlock, V. et Wennberg, P. O. (2011). The Total Carbon Column Observing Network. *Philosophical Transactions of the Royal Society A : Mathematical, Physical and Engineering Sciences*, 369(1943), 2087–2112. <http://dx.doi.org/10.1098/rsta.2010.0240>. Récupéré de <http://www.ncbi.nlm.nih.gov/pubmed/21502178>
<http://rsta.royalsocietypublishing.org/cgi/doi/10.1098/rsta.2010.0240>

Yang, P. (2003). Spectral signature of ice clouds in the far-infrared region : Single-scattering calculations and radiative sensitivity study. *Journal of Geophysical Research*, 108(D18), 4569.
<http://dx.doi.org/10.1029/2002JD003291>. Récupéré de
<http://doi.wiley.com/10.1029/2002JD003291>